Development of Carbon Nanomaterials/Transition Metal Oxides Based Hybrid Composites as High Performance Anode Materials for Lithium-Ion Batteries

A Dissertation Submitted to the Department of Chemistry,

Quaid-i-Azam University, Islamabad, in Partial Fulfillment of the

Requirements for the Degree of

Doctor of Philosophy

in
Physical Chemistry

by

Laraib kiran

Department of Chemistry
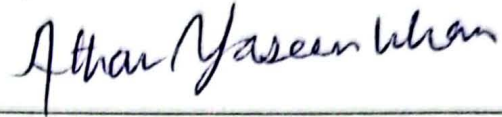
Quaid-i-Azam University

Islamabad, Pakistan

2024

DECLARATION

This is to certify that this dissertation entitled *"Development of Carbon Nanomaterials/Transition Metal Oxides based Hybrid Composites as High-Performance Anode Materials for Lithium-Ion Batteries"* submitted by *Ms. Laraib Kiran,* is accepted in its present form by the Department of Chemistry, Quaid-i-Azam University, Islamabad, Pakistan, as satisfying the partial requirement for the award of degree of *Doctor of Philosophy in Physical Chemistry.*
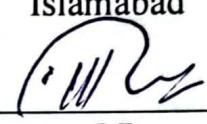
External Examiner (I):

Prof. Dr. Athar Yaseen Khan
Department of Chemistry
Forman Christian College
Ferozepur Road
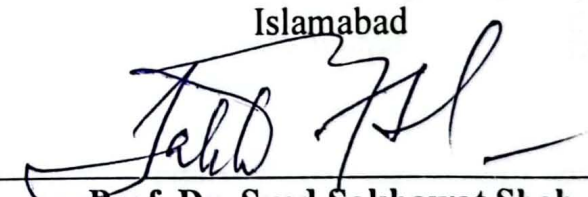Lahore

External Examiner (II):

Dr. Khalid Khan
Director Coordination
PAEC Head Quarter
Islamabad

Co-Supervisor :

Dr. Muhammad Imran Shahzad
Nanosciences & Technology
Department (NS&TD)
National Centre for Physics (NCP),
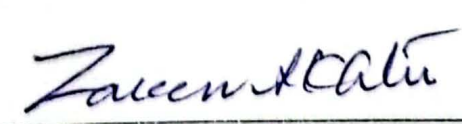Islamabad

Supervisor:

Prof. Dr. Syed Sakhawat Shah
Department of Chemistry
Quaid-i-Azam University
Islamabad

Head of Section:

Prof. Dr. Hazrat Hussain
Department of Chemistry
Quaid-i-Azam University
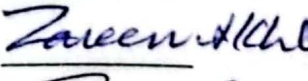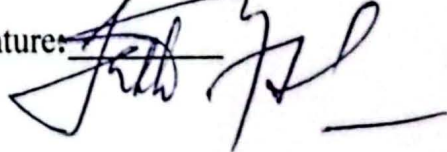Islamabad.

Chairperson:

Prof. Dr. Mrs. Zareen Akhter
Department of Chemistry
Quaid-i-Azam University
Islamabad.

Certificate of Approval

This is to certify that the research work presented in this thesis, entitled **"Development of Carbon Nanomaterials/Transition Metal Oxides based Hybrid Composites as High-Performance Anode Materials for Lithium-Ion Batteries"** was conducted by **Ms. Laraib Kiran** under the supervision of **Prof. Dr. Syed Sakhawat Shah**

No part of this thesis has been submitted any where else for any other degree. This thesis, is submitted to the **Department of Chemistry Quaid-i-Azam University Islamabad** in partial fulfillment of the requirements for the Doctor of Philosophy in Field of **Physical Chemistry, Department of Chemistry, Quaid-i-Azam University, Islamabad.**

Student Name   Ms. Laraib Kiran   Signature: _____

Examination Committee:

1. **External Examiner:**   **Prof. Dr. Athar Yaseen Khan**   Signature: _____
   Department of Chemistry
   Forman Christian College
   Ferozepur Road
   Lahore.

2. **External Examiner:**   **Dr. Khalid Khan**   Signature: _____
   Director Coordination
   PAEC Head Quarter
   Islamabad

3. **Internal Examiner:**   **Prof. Dr. Hazrat Hussain**   Signature: _____
   Department of Chemistry
   Quaid-i-Azam University
   Islamabad.

Co-Supervisor: **Dr. Muhammad Imran Shahzad**   Signature: _____

Head of Department: **Prof. Dr. Zareen Akhter**   Signature: _____

Supervisor   **Prof. Dr. Syed Sakhawat Shah**   Signture: _____

AUTHOR'S DECLARATION

I, **Ms. Laraib Kiran** hereby state that my Ph.D. thesis titled **"Development of Carbon Nanomaterials/Transition Metal Oxides based Hybrid Composites as High-Performance Anode Materials for Lithium-Ion Batteries"** is my own work and has not been submitted previously by me for taking any degree from this University (Quaid-i-Azam University Islamabad) or anywhere else in the country/world.

At anytime if my statement is found to be incorrect even after my Graduation the University has the right to withdraw my Ph.D. degree.

Name of student: **Ms. Laraib Kiran**

PLAGIARISM UNDERTAKING

I solemnly declare that, the research work presented in the thesis titled **"Development of Carbon Nanomaterials/Transition Metal Oxides based Hybrid Composites as High-Performance Anode Materials for Lithium-Ion Batteries"** is solely my research work with no significant contribution from any other person. Small contribution/help wherever taken has been duly acknowledged and that complete thesis has been written by me.

I understand the zero tolerance policy of the HEC and **Quaid-i-Azam University Islamabad** towards plagiarism. Therefore, I as an Author of the above titled thesis declare that no portion of my thesis has been plagiarized and any material used as reference is properly referred/cited.

I undertake that if I am found guilty of any formal plagiarism in the above titled thesis even after award of Ph.D. degree, the university reserves the rights to withdraw/revoke my Ph.D. degree and that HEC and the University has the right to publish my name on the HEC/University website on which names of students are placed who submitted plagiarized thesis.

Student/Author Signature: _____

Name: **Ms. Laraib Kiran**

Declaration

I **Laraib Kiran,** Ph.D. scholar in the Department of Chemistry, Quaid-i-Azam, University, Islamabad, Pakistan , hereby solemnly declare that my Ph.D. dissertation titled **"Development of Carbon Nanomaterials/Transition Metal Oxides based Hybrid Composites as High- Performance Anode Materials for Lithium-Ion Batteries"** is the research work that I have performed under the supervision of Professor Dr. Syed Sakhawat shah and co-supervision of Dr. Muhammad Imran Shahzad and previously has not been submitted for any other degree or professional qualification except as specified , from Quaid-i-Azam University, Islamabad or anywhere else.

Signature: _Laraib_

Date: _04-07-2024_

This thesis is dedicated to my father,

the man who taught me to perform all of life's tasks

to the best of my abilities

Acknowledgment

All acclamations and gratitude's are for **ALMIGHTY ALLAH**, the Omnipresent, the Omnipotent, the Beneficent, the Compassionate and the source of all wisdom and knowledge, who granted me the courage, strength and intellectual ability to complete this humble input towards knowledge. I am very proud of being a follower of the Holy Prophet **HAZRAT MOHAMMAD (PBUH) ,** the most perfect, ideal and exalted among and of ever born on the surface of earth, who (PBUH) declared it to be an obligatory duty of every man and woman to seek and acquire knowledge. My heartiest thanks and sincerest gratitude to my supervisor, Professor, **Dr. Syed Sakhawat Shah**, Department of Chemistry, Quaid-i-Azam University for his skillful guidance, important suggestions, sound advices and valuable discussions throughout my research whenever needed. I extend my heartfelt gratitude to my Co-Supervisor, **Dr. Muhammad Imran Shahzad**, National center for physics, for their indispensable guidance, expertise, and continuous support throughout the completion of research. Their valuable insights and dedication significantly enriched this work. I am immensely grateful to **Prof. Dr Mehmet Kadri Aydinol** for providing me opportunity to carry out research work in his group under (Türkiye burslari Scholarships program). I pay my paramount respect and gratefulness to Head of Physical Section, Prof Dr**. Hazrat Hussain** and **Prof. Dr. Zareen Akhter**, Chairperson Department of Chemistry, QAU, Islamabad and **Dr. Muhammad Siddiq** for their sincere attitude, constant help and continuous encouragement throughout the period of my degree. I am grateful to my best friend and roommate **Poshmal Sumreen** for helping me in hard times, and for all the entertainment, advices, support, love and care she provided. No deeds can return and no words can express the affection, love, amiable sacrifices, attitude, unceasing prayers, advices, inspiration and support that my parents (**Muhammad Zafar Abbas and Khursheed Fatima**), brothers (**Muhammad Zaeem Abbas**, **Muhammad Ahmar Ali and Muhammad Ahmad Hasssan**), my uncle (**Muhammad Akhtar Abbas**) throughout my academic career and my life. Furthermore, I feel an enormous admiration and immense obligation for my caring father because of his prayers and love in my life, my asset. May ALMIGHTY ALLAH bless him all a healthy, long and happy life.

Laraib kiran

Abstract

There has been a substantial increase in the use of lithium-ion batteries in a variety of portable electronics and electric gadgets. Graphite is most commercially used anode material in LIBs owing to ecofriendliness, long cycle life, good electronic conductivity, low cost, abundance and low volume changes. However, it displays unsatisfying theoretical specific capacity of 327 mAhg^{-1} and volumetric capacity of 850 mAhcm^{-1} which, hardly meet the requirements for large scale applications (e.g., electric vehicles). Therefore, research is constantly conducted to find good substitute of graphite as anode material. In this context, two dimensional materials such as transition metal oxides (TMOs) have drawn considerable attention as a better substitute of graphite owing to superior electrochemical performance, good specific capacity (between 700 and 1200 mAh g^{-1}) and chemical activity, but application of TMOs is hindered by the capacity decay due to huge volume variation, poor electrical conductivity and slow ion diffusion. Multiple strategies have been proposed to avoid these kinds of problems and to improve electrochemical performance. One attractive approach is to prepare variety of nanostructures including nanorods, nanosheets, porous spheres and nanowires with controlled morphology and dimension and other effective method is to combine TMOs with carbonaceous materials such as multi-walled carbon nanotubes (MWCNTs). MWCNTs is attractive owing to its high aspect ratio, good mechanical properties, high electrical conductivity, remarkable thermal conductivity, good mechanical and chemical stability that can effectively reduce volume expansion and improve the electrode's rate capability and reversible capacity. The structure and tensile strength of MWCNTs not only provide high electrical conductivity, structural flexibility, high surface to volume ratio and chemical stability but also prevent aggregation of nanoparticles and volume expansion/contraction. Therefore, nanocomposite of electrically conductive and flexible MWCNTs anchored with TMO can prove to be a good candidate with superior electrochemical performance in LIBs. In order to overcome further limitations and to increase cyclic stability of anode materials, polyaniline (PANI) has been considered one of the promising polymers due to its high conductivity, low cost, chemical and environmental stability, distinctive physical and electrochemical properties. In this work, a suitable amount of conducting PANI coating was achieved to increase the surface electrical conductivity and to prevent cracking and pulverization of TMOs electrode. PANI coating also promotes Li^{+} ion conductivity,

buffers volume changes, maintains structural integrity during cycling, prevents side reactions between electrode and electrolyte, enhance electronic/ ionic transport, suppresses overproduction of SEI and facilitates high electron transportation because of its large surface area and small size.

Co-precipitation method was used to synthesize MoO_3, and multi-walled CNTs (MWCNTs) were introduced into the active material. Moreover, these materials were uniformly coated with PANI using in situ chemical polymerization. MoO_3-$(CNT)_{12\%}$-PANI exhibited high discharge capacities of 1382 $mAhg^{-1}$ and 961 $mAhg^{-1}$ at current densities of 50 mAg^{-1} and 100 mAg^{-1}, respectively. The homogenous nanocomposite of Cr_2O_3-MWCNTs and PANI exhibit good electrochemical performance. A discharge capacity of Cr_2O_3-$MWCNTs_{(12\%)}$ -PANI is found to be 815 $mAh\ g^{-1}$ at 100 $mA\ g^{-1}$ with coulombic efficiency of 97.5 %. Moreover, the nanocomposite exhibits good rate capability and cyclic stability. A discharge capacity of 840 $mAhg^{-1}$ was observed in case of WO_3-$(CNT)_{12\%}$-PANI nanocomposite at current density of 100 mAg^{-1} with coulombic efficiency of 90.40%. Furthermore, WO_3-$(CNT)_{12\%}$-PANI nanocomposite showed stable rate and cycling performance at higher current densities. Hence, WO_3-$(CNT)_{12\%}$-PANI nanocomposite could be a good anode material for lithium-ion batteries.

Similarly, Cr_2O_3, WO_3 and MoO_3 anode materials were also synthesized with reduced graphene oxides and PANI coating. The WO_3-$(RGO)_{12\%}$-PANI composite electrode exhibited remarkable reversible discharge capacity (~1188 $mAhg^{-1}$ at 100mAg^{-1}), and excellent cycling stability (770.23 $mAhg^{-1}$ at 400mAg^{-1} after 30 cycles). Hence, WO_3-$(RGO)_{12\%}$-PANI nanocomposite could be a good anode material for lithium-ion batteries. Cr_2O_3-$(RGO)_{12\%}$-PANI exhibited discharge capacity of 891.81$mAhg^{-1}$ at 100mAg^{-1} and 535.8$mAhg^{-1}$ at 400mAg^{-1} after 30 cycles, while MoO_3 –$(RGO)_{12\%}$-PANI showed discharged capacity of 1027.6 $mAhg^{-1}$ at 100 mAg^{-1} and 656.8 $mAhg^{-1}$ at 400 mAg^{-1} after 30 cycles.

Table of contents

List of Figures

List of Tables

List of Abbreviation

Title	Abbreviation
Transition metal oxides	TMOs
Hybrid electrical vehicles	HEVs
Electrical vehicles	EVs
Ethylene carbonate/diethyl carbonate	EC/DEC
Polypropylene	PP
Solid electrolyte interface	SEI
Multiwalled carbon nanotubes	MWCNTs
Single walled carbon nanotubes	SWCNTs
Reduced Graphene Oxides	RGO
Polyvinylidene difluoride	PVDF
N−methyl−2−pyrrolidinone	NMP
X-ray diffraction	XRD
Fourier transform infrared	FTIR
Scanning electron microscopy	SEM
Thermogravimetric analysis	TGA
Brunauer−Emmett−Teller	BET
Barrett–Joyner–Halenda	BJH
X-ray Photoelectrons spectroscopy	XPS
Chromium Oxides	Cr_2O_3
Tungsten Oxides	WO_3
Molybdenum Oxides	MoO_3
Polyaniline	PANI

1. INTRODUCTION

1.1 Background

The power sector is essential to the growth of any developing nation since it not only helps meet citizens' immediate need but also paves the way for future progress. Energy plays an important role in different sectors such as education, businesses, agriculture, health and other service sectors. It has become the main reason for a country's progression and development. Alongside Pakistan, various third world countries have suffered from energy crises. In Pakistan, such crises have plagued the industrial sector, increased unemployment, reduced exports, increased prices, reversed foreign investment, affected agricultural yield, and led to the closure of businesses. With urbanization and increasing population, consumption of energy has increased which put huge pressure on domestic resources. There is a growing need for sustainable and eco-friendly energy sources in several aspects of life. According to global energy scenario, approximately 80% of total energy need is fulfilled by fossil fuels. Nonrenewable fossil fuel, like coal, natural gas, and crude oil, are now the sources of energy that are responsible for the greatest amount of consumption. However, there are two significant issues that are connected to these sources of energy. The combustion of fossil fuels results in the emission of a number of toxic gases and particulates, including oxides of nitrogen (NO_x), oxides of sulfur (SO_x), oxides of carbon (carbon mono and dioxide–CO_x), and particulates. These gases and particulates contribute to climate change. In light of the ongoing depletion of non-renewable energy sources, the demand for renewable energy is a viable option for developing countries[1-3]. The increasing energy usage and resulting environmental issues have created a substantial need for renewable and eco-friendly energy sources. [4, 5] as alternatives to traditional fuels. Consequently, researchers are trying to develop affordable, ecofriendly and environment friendly energy storage devices using low cost, potentially abundant material. The development of renewable energy sources such as hydro, biomass, solar, fuel cells, wind, and geothermal energy limits global warming, environmental pollution and reduce consumption of fossil-based resources[6, 7].

According to estimates, the total amount of electricity generated around the globe in the year 2012 was 21.53 trillion kilowatt hours (kWh). It is anticipated that the global

production of electricity would reach up to 39 trillion kWh (81%) by the year 2040. According to the data presented in Fig 1.1, it is anticipated that the renewable energy sources would be responsible for 25 percent, or 9.6 trillion kWh, of the world's total electricity generation in the year 2040. This type of energy is clean, easily accessible and affordable, and it is readily available in a variety of forms. Wind and solar energy have been regarded abundant, clean, and the largest renewable energy source after hydro (3.646 trillion kWh) for the creation of electricity[8-11].
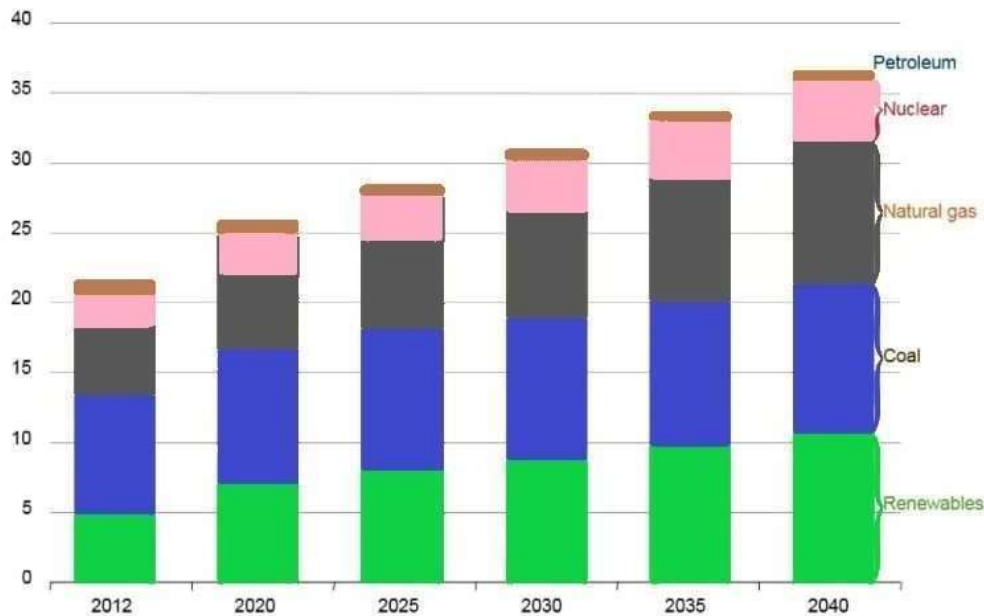
Figure 1.1 World electricity generation by source (Trillion KWh). EIA International Outlook to 2040 Foresees Decoupling of Power Demand and Economic Growth [12].

The degree of power extraction from these sources has increased tremendously over the past decade. By 2014, the capacity extracted from solar power had increased to 177 GW from 2.6 GW in 2004, while the installed capacity of wind has increased from 48GW to 370GW[13].

These energy sources are very promising for future utilization but, the problem with these energy sources are their dependency on weather and time and therefore their smooth running require energy storage systems that can integrate them effectively in to grid[14]. This indicates that heavy research has to be conducted out enhance the quality of energy conversion devices, which produce energy from renewable energy sources as well as energy storage devices which would provide energy from renewable sources during their off-peak time and for smooth integration in to grids to overcome electricity

demands and to obtain a clean environment by switching from ICEs powered vehicles to electricity propelled vehicles in order to avoid use of fossil and nuclear fuels[15].
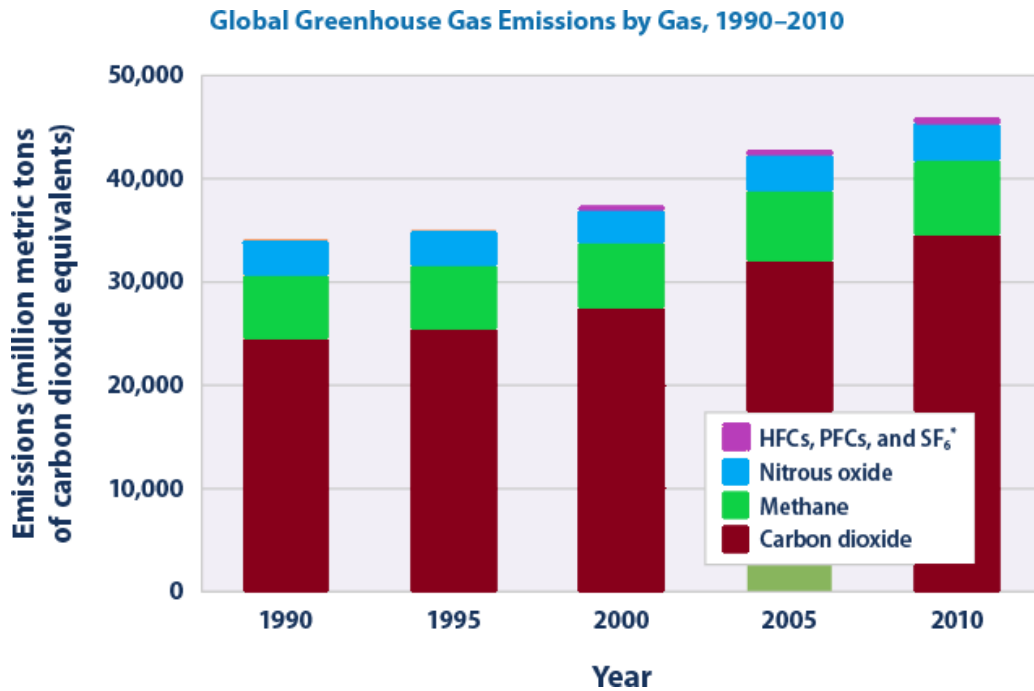
Figure 1.2 GHG emissions during 1990-2010. (global greenhouse emission by gas 1990-2010)[16].

1.2 Energy Storage Devices

There is a wide range of renewable energy sources required to meet global energy needs and address national economic issues. Rechargeable lithium-ion batteries, capacitors, supercapacitors (ultracapacitors), and fuel cells are just a few examples of the energy storage systems available, but, lithium-ion batteries (LIBs) have been proved as promising energy storage devices that are widely used in daily life, such as in hybrid electric vehicles, space exploration, aviation [17] and portable electronic device [18, 19], owing to high power densities, environmental friendliness, long cycle life, low self-discharges, high energy densities, small ionic sizes (which permit fast Li^+ intercalation in solids) that are a main factor for fast charging, cyclic stabilities, small memory effects and high open circuit voltage[20, 21]. To fulfill the current energy demands, the electrochemical performance of LIBs including cycle life, capacity, power density and charging speed should be enhanced[17]. Since the mechanism of LIBs is based on the movement of Li^+ ions between the anode and cathode, the electrochemical and physical properties of the electrode materials have significant influence on the performance of

the battery; typically, a variety of lithium metal oxides such as $LiCoO_2$ have been used as the cathode material [21], and graphite is mainly used as the anode material in commercial LIBs owing to low cost, stable operational potential and environmental friendliness[22, 23]. In recent decades, there have been ongoing efforts to create appropriate anode materials for LIBs. However, achieving high-performance anode materials that meet the energy demands of the future remains a significant issue. [24] [25].

1.3 Battery history

Over the course of time, energy storage systems have undergone various transformations and improvements in response to growing demand and technological breakthroughs. Several significant advancements throughout history have played important role in the development and progression of batteries. In 1938, Wilhelm Konig, a German archaeologist, made a significant discovery in Khujut Rabu, located in close proximity to Baghdad, Iraq. The findings consisted of clay jars, measuring approximately the size of a human fist. The jars consisted of an iron rod encased within a copper cylinder, sealed with an asphalt stopper. There is a prevailing belief that the ancient Parthian culture, which held dominion over the region approximately two millennia ago, employed jars of a specific nature as electrical batteries for the purpose of electroplating gold onto silver. In the year 1786, Luigi Galvani, an Italian physicist, made an observation of an unusual occurrence. He observed that when the legs of a deceased frog were touched while connected to a brass hook and an iron knife, the legs exhibited convulsive movements. He observed that this phenomenon was a result of a correlation between muscular action and electrical impulses. However, these findings resulted in the formulation of the fundamental principles behind contemporary batteries. In the year 1800, Allesandro Volta presented the initial effective exhibition of a contemporary battery, which is presently informally referred to as the Voltaic pile. The device was constructed by arranging a series of zinc and silver plates in an alternating manner, with each plate being separated from its adjacent plate by a cloth soaked in a solution containing a diluted acid and salt.

Lithium-ion battery was discovered 30 years ago. Its structure consist of five parts: Anode, cathode, separator, current collector and electrolyte[26].

1.4   Components of Battery

Lithium-ion battery consist of basic five components, mainly anode, cathode, separator, electrolyte and current collector. Separator is placed to prevent short circuiting. Current collectors are also placed, because anode and cathode are not good at gaining and distributing electrons.

1.4.1 Anode

The anode plays a crucial role in rechargeable batteries, and its morphology and characteristics have a significant impact on battery performance. This is due to the fact that the anode is believed to be an extremely important component of these batteries. Because of the van der Waals forces that exist between molecules, graphite is the anode material that is most commonly utilized in commercial applications. This is because lithium ions may be easily inserted and removed on the layer structure of graphite[27]. On the other hand, it has a low-capacity retention. In an effort to find solutions to these issues, a large number of researchers are currently working on the production of novel anode materials that have a high specific capacity [28]. In certain investigations, alloy-based anode materials like tin (Sn), aluminum (Al), silver (Ag), antimony (Sb), and magnesium (Mg) were utilized, and they showed a capacity that was twice as high as carbon-based materials[27]. In recent years, transition metal oxides have emerged as one of the anodes that have gained a significant amount of attention. They showed to be a better option for graphite as anode materials for future lithium-ion batteries due to the excellent improvement that has been made in electrochemical characteristics. [29]. They do not release hazardous by products into the environment, have a high power density and theoretical specific capacity, may be found in large quantities in nature, and have an inexpensive production method [27].

Graphite is most commercially used anode material in LIBs owing to eco friendliness, long cycle life, good electronic conductivity [30], low cost, abundance and low volume changes [31]. However, it displays unsatisfying theoretical specific capacity of 327 mAh g^{-1} and volumetric capacity of 850 mAhcm^{-1} [24] which, hardly meet the requirements for large scale applications (e.g., electric vehicles). Therefore, research is constantly conducted to find good substitute of graphite as anode material. Recently, some alternative electrode materials based on alloying or conversion reactions such as metal oxides, sulfides or nitrides are being developed. However, the electrochemical

performance of these materials is not up to the mark because of their low conductivity and limited practical capacity. Thus, it is necessary to develop some novel anode materials with good capacity, excellent rate performance and cycle stability. In this context, two dimensional materials such as transition metal oxides (TMOs) have drawn considerable attention as a better substitute of graphite owing to superior electrochemical performance, good specific capacity (between 700 and 1200 mAhg^{-1}) and chemical activity [32].

Thus, many transition metal oxides such as Co_3O_4, CuO, MoO_3, WO_3, NiO and SnO_2 have been prepared. Moreover, Si nanostructures, metal sulfides [33] and tin compounds have also been developed in the field of lithium-ion battery owing to their large theoretical capacities, widespread availability and environmental friendliness[17 34]. Chu et al. prepared MFe_2O_4-HPSs particles confined with a carbon network that exhibited high cyclic stability and good rate performance. Moreover, these nanoparticles maintain structural integrity during charging and discharging [35]. Qinglin et al. prepared $ZnO/ZnFeO_4$ nanospheres. Impressively, $ZnO/ZnFeO_4$ showed good cycling performance (1137 mAhg^{-1} after 80 cycles at 1 Ag^{-1} [36]. Among all of them, transition metal oxides possess variable valence states and diverse morphology [33].

1.4.2 Cathode

The cathode of a lithium-ion battery is composed of a conductive framework and an active material, typically lithium compounds. This active material is crucial to the functioning of the battery.

The evaluation of electrochemical and safety performance of the battery is a crucial factor. Lithium cobalt oxide (LCO), which is the most fundamental cathode material accessible in the commercial market, has been substituted by Lithium Manganese Oxides (LMO) due to its inadequate thermal stability. However, it is important to note that LMO exhibits a lower energy density compared to LCO. Phosphate-based cathode materials, including Lithium vanadium Phosphate ($LiV_2(PO_4)_3$ and Lithium Iron phosphate (LFP), have been generally employed due to their favorable thermal stability and robust P-O bonds
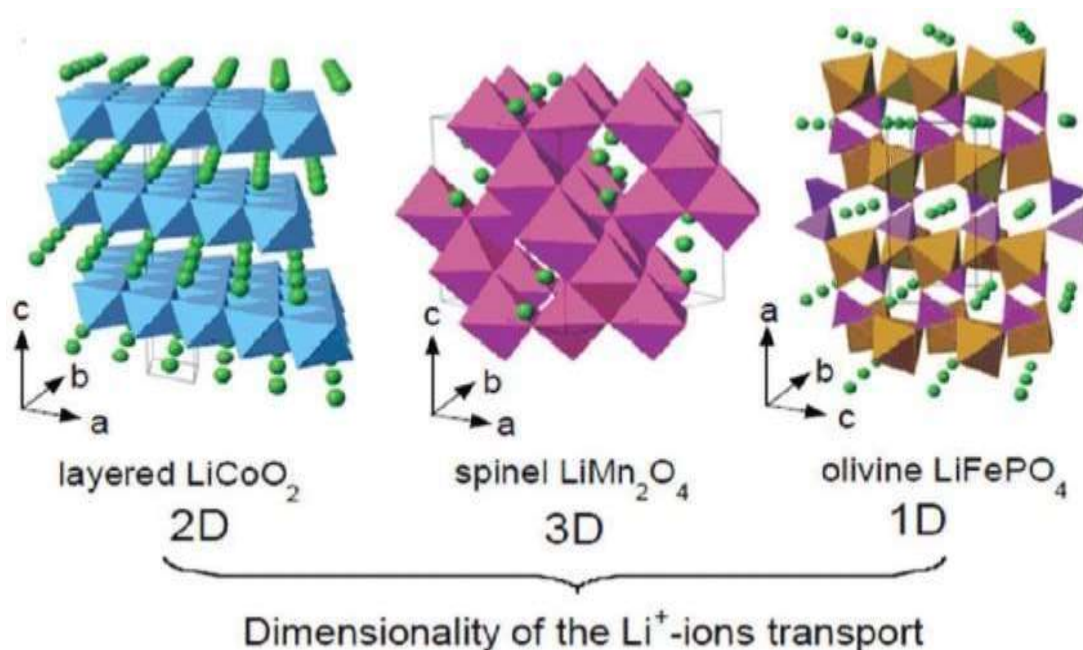
Figure 1.3 Crystal structure of layered LiCoO$_2$ (2D) , spinel LiMn$_2$O$_4$ (3D) ,and olivine LiFePO$_4$ (1D) frameworks[37].

Currently, there are several cathode materials with diverse layered crystal structures accessible in the commercial market. These include LiNiO$_2$, LiCoO$_2$, and LiNi$_{1/3}$Co$_{1/3}$Mn$_{1/3}$O$_2$, which feature layered crystal structures as shown in fig 1.3. Additionally, there are cathode materials with olivine structures, such as LiFePO$_4$, and spinel structures, including LiMn$_2$O$_4$ and LiNi$_{1/2}$ Mn$_{3/2}$ O$_4$.

1.4.3 Electrolyte

It is important for the electrolyte to exhibit stability within a designated temperature range that aligns with the expected operational conditions of the battery. Therefore, it is imperative that the electrolyte's melting and boiling points are situated outside the designated working temperatures and remain constant for its entire lifespan. In addition, it is imperative to consider operational safety and environmental sustainability during the manufacturing process, as well as in the routine utilization and disposal of electrolytes.

During the electrochemical cycling process of the battery, lithium ions undergo diffusion over the electrolyte medium, thereby traversing the spatial gap that separates the cathode and the anode. The solid electrolyte interphase (SEI) is commonly recognized as the primary protective layer for an electrode. However, its effectiveness is contingent upon the specific electrolyte employed and its intrinsic breakdown

properties. Organic molecules present in the electrolytic volume can undergo decomposition. The process of breakdown has the potential to reduce electrochemical performance. If the strength of electrolyte-ion interaction is excessive, it can lead to a decrease in the intercalation of Li^+ ions into electrode. This is because the ion must be capable of departing from its solvation shell in order to enter the electrode. The diffusion process is further difficult due to the tendency of Li ions to aggregate into clusters, referred to as solvation shells, in the presence of other organic solvent molecules and anions inside the electrolyte. The diffusivity of lithium ions is decreased, resulting in a reduction in the ion's mobility across the electrolyte. Furthermore, the presence of solvation shells can significantly impact the stability of electrodes. Hence, it is imperative to enhance our comprehension of the interactions between electrolyte molecules and Li ions in order to maximize the efficiency of the battery[38].

1.4.3.1 Lithium salt optimization

Lithium hexafluorophosphate ($LiPF_6$) is the lithium salt most often used in LIBs because it works well with Al current collectors. $LiPF_6$ can't meet the need for high-performance LIBs, though, because it isn't very stable at high temperatures and is very sensitive to moisture. A lot of work went into making new lithium salts, which are a great replacement to $LiPF_6$. In 2012, Seo et al. used Raman spectroscopy, molecular dynamics, and quantum chemistry to show that the strength of the bond between anions and Li^+ changes the structure of the solvation, which in turn changes the formation of SEI, which is similar to ICE[15] [39].

The mechanism behind the influence of water on the electrolyte is attributed to a sequence of steps by the reaction of water with $LiPF_6$. These reactions are responsible for the effect that water has on the electrolyte. The particular equation for the reaction is as it follows:

$H_2O + LiPF_6 \rightarrow POF_5 + LiF + 2HF$

$LiPF_6 \rightarrow LIF + PF_5$

$H_2O + PF_5 \rightarrow POF_5 + 2HF$

$H_2O + POF_5 \rightarrow PO_2F + 2HF$

$2H_2O + PO_2F \rightarrow H_3PO_4 + HF$
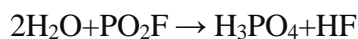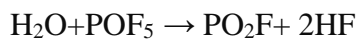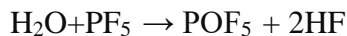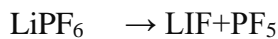
The reaction between water and lithium salt $LiPF_6$ is recognized to primarily yield solid precipitate LiF and hazardous substance HF. LiF is responsible for the resistance of the battery, primarily by increasing the thickness of the solid electrolyte interphase

(SEI) film. Conversely, HF is known to disrupt the integrity of the SEI film layer, resulting in the deterioration of the SEI film. The process of battery cycling leads to a gradual deterioration in battery cycle performance due to the ongoing reconstruction and restoration of the membrane layer.

The hydrolysis of electrolytes triggers the formation of hydrofluoric acid, which aggravates the dissolution of transition metals and hinders the advancement of high energy-density lithium batteries that rely on high voltage cathodes. In order to mitigate the laborious and time-intensive processes involved in industrial water removal, the utilization of only metal-organic frameworks (MOFs) was implemented within the cells as highly efficient integrated water-removal agents. Consequently, the integration of the intrinsic water scavenger with diverse high-voltage cathodes yielded enhanced cycling stability, as evidenced by the higher performance seen after 400 cycles, even under challenging conditions characterized by the 200 ppm water in the electrolyte. The utilization of MOFs as water adsorbents has the potential to concomitantly decrease the production expenses of lithium-ion batteries (LIBs), enhance their durability, and improve their safety [40].

Lithium hexafluorophosphate ($LiPF_6$) is a chemical compound that is commonly used as an electrolyte in lithium-ion batteries. Lithium hexafluorophosphate ($LiPF_6$) is a commonly employed salt in lithium-ion batteries.

The compound exhibits a high solubility in many solvents, particularly dipolar aprotic organic solvents commonly employed in scientific research. These solvents include cyclic carbonates like ethylene carbonate, as well as linear carbonates such as dimethyl carbonate, diethyl carbonate, and ethyl methyl carbonate. The dissolution in these solvents results in the generation of high levels of ionic conductivities. The ionic conductivity is significantly influenced by the size of the anion. In the case of $LiPF_6$, the anionic size is 0.255 nm.

The enhancement of ionic conductivity is dependent upon the reduction in the size of the anions. $LiPF_6$ exhibits outstanding electrochemical properties. $LiPF_6$ is electrochemical inert, enabling it to generate a protective coating on the aluminium current collector, preventing it from corrosion. Additionally, $LiPF_6$ demonstrates significant anionic mobility. The thermal stability of $LiPF_6$ at temperatures exceeding 55 °C is found to be inadequate. This is due to the decomposition reaction of $LiPF_6$, resulting in the formation of LiF (solid) and PF_5 (gas). It is important to note that the

reaction between PF_5 and solvents can produce highly toxic substances. Additionally, $LiPF_6$ exhibits significant moisture instability. Furthermore, when compared to other salts, $LiPF_6$ demonstrates low anodic stabilities.

1.4.4 Solvent

The basic function of the solvent in a battery is to facilitate the dissolution of the electrolyte salt, hence facilitating the transit of lithium ions and enabling the flow of ionic current.
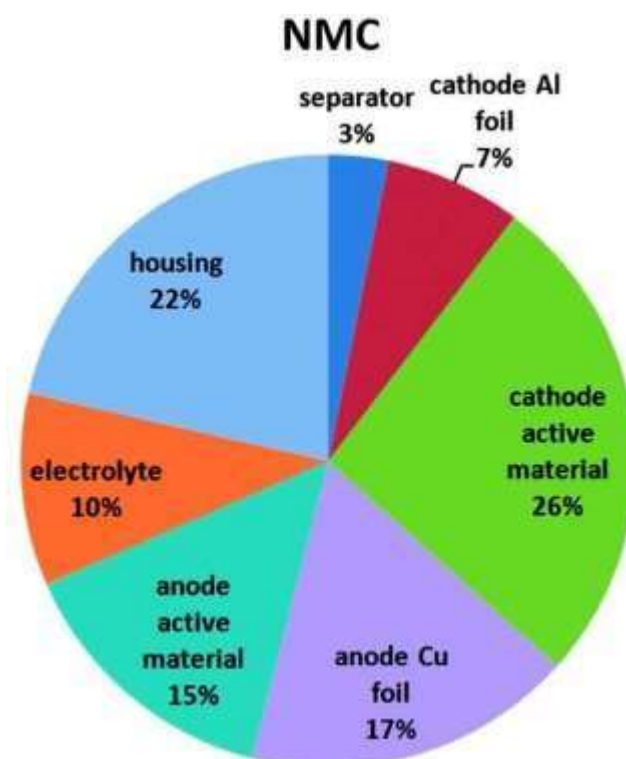
Figure 1.4 Components of a battery with their corresponding mass and percentages in a cell[41].

Dimethylformamide (DMF), ethylene carbonate (EC), propylene carbonate (PC), dimethyl carbonate (DMC), diethyl carbonate (DEC), and ethylmethyl carbonate (EMC) are frequently employed as polar and non-volatile solvents. The necessary characteristics for an optimal electrolyte solvent are as follows. The device must possess the ability to dissolve lithium salts to a sufficient concentration. The substance demonstrates a low viscosity, specifically equal to or less than 1 centipoise (cP), which facilitates rapid ion transportation. The substance should exhibit a liquid state across a broad spectrum of temperatures, characterized by a low melting point and a high boiling point.

The material should exhibit enough wettability with respect to both the electrodes and the separator. The substance should possess a low vapor pressure. The selection of a solvent should prioritize environmental sustainability and affordability. The interaction between electrode materials is inert. The cell components exhibit a state of inactivity, mostly limited to the charged surfaces of the electrodes and the current collectors[42].

1.4.5 Effect of binder

The purpose of the binder is to ensure that the active particles and the conductive substance that is combined with the current collector have a strong adherence to one another.

Figure 1.5 Schematic diagram of a battery representing binder adhesion of active particles with current collector[43].

In order to establish a stable SEI with an electrolyte, a suitable binder should have the properties of maintaining a good adhesion between the electrodes, as well as the ionic connection, and it should also make the development of the SEI easier. Even though it only accounts for two to five percent of the total mass of a commercial electrode, the binder is an essential component in improving the performance of the cell. Because of this, making the appropriate selection of binders is essential in determining both the cycle life of the cell and its rate capability[43].

Poly(vinylidene fluoride) (PVDF) is binder that is commonly used but has limited elastomeric characteristics. In addition to this, PVDF necessitates the utilization of organic solvents during its manufacturing, resulting in extended drying periods that subsequently escalate both costs and environmental degradation. Therefore, additional research is being conducted to enhance the elastomeric properties of binders, while reducing toxicity and improving cost-effectiveness. In this regard, it has been observed that sodium carboxymethyl cellulose (CMC), as an aqueous binder, exhibits more efficacy in enhancing capacity retention compared to polyvinylidene fluoride (PVDF) and other elastomeric binders [44, 45].

1.5 Working Principle of Lithium-ion Battery

The fundamental working principle of a lithium-ion battery is the extraction and insertion of lithium ions between the two electrodes. The intercalation and de-intercalation reactions of lithium ions at respective electrodes can be described as following equation.

The movement of lithium ions back and forth between the two electrodes of a lithium-ion battery in a reversible manner constitutes the fundamental mechanism that demonstrates the operation of the battery. The equation that summarizes the intercalation and de-intercalation reactions of lithium ions at their respective electrodes may be found in equation 1.3 [12].

The fundamental operational principle of a lithium-ion battery involves the reversible movement of lithium ions between two electrodes. The intercalation and de-intercalation reactions of lithium ions at their corresponding electrodes can be expressed by the following equation [12].

Cathode: $LiCoO_2 \leftrightarrow Li1\text{-}xCoO_2 + xLi+ + xe^-$ (Eq. 1.1)

Anode: $C + yLi+ + ye- \leftrightarrow LiyC$ (Eq. 1.2)

Overall reaction: $LiCoO_2 + xC \leftrightarrow yLi1\text{-}xCoO_2 + xLiyC$ (Eq. 1.3)
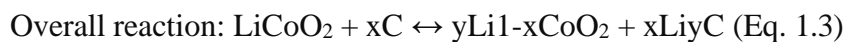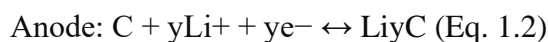
The relationship between the variables "x" and "y" in Equation 1.3 is depending upon the composition of the electrodes employed in the actual cell. Lithium-ion batteries, similar to lithium metal batteries, encompass the process of lithium ions being transported back and forth between anodes and cathodes. When an electrical potential difference is imposed across the electrodes, the lithium ions situated inside the porous oxide layers of the cathode are compelled to migrate, move across the electrolyte, and ultimately insert themselves into the interstitial spaces situated between the layers of

the anode material. The phrase "intercalate" is frequently used in lithium-ion battery in reference to the process of incorporating lithium-ion batteries, instead of the term "insert". To ensure charge neutrality, the ionization process occurring within the cathode of lithium metal oxide leads to the reduction of the metal, hence generating free electrons. The liberated electrons generated through this process move through the wire.
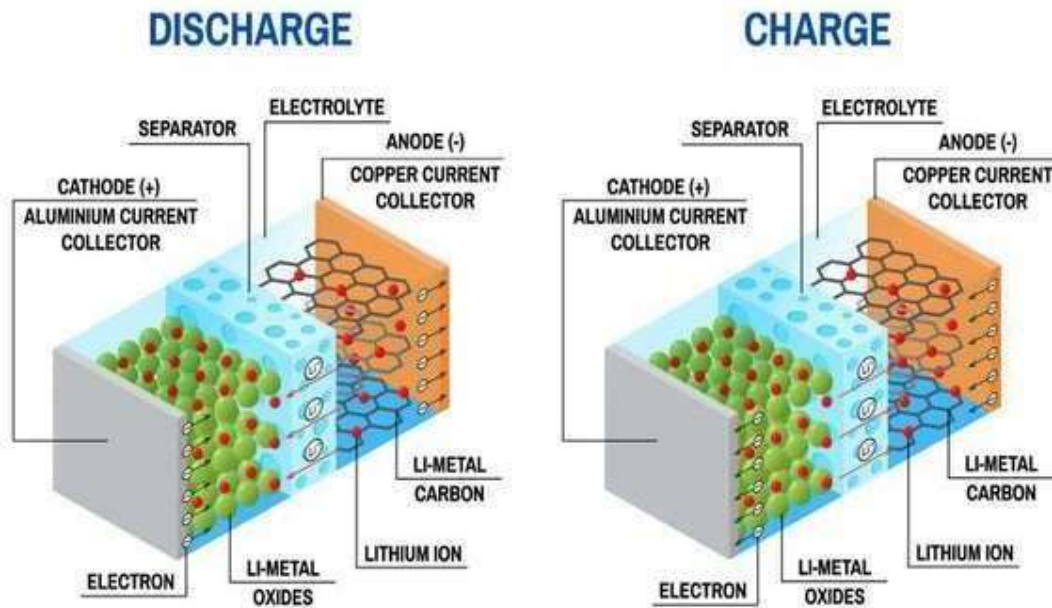
Figure 1.6 Representation of Lithium-ion battery(LIBs)[46].

The nature of the metal that is present in lithium metal oxide-based cathode, the nature of the anode material, and the type of electrolyte that is employed are the factors that define the voltage that must be applied during this process. The process of discharging is the opposite of charging, in which lithium ions deintercalated from the anode material and are once again accommodated by cathode material. This process occurs while the battery is being discharged. During this procedure, powering devices is accomplished by utilizing the difference in potential that is created between the two electrodes. As a result, during the discharge process, electrons go from the anode to the cathode, and a positive current emerges from the cathode, which serves as the positive terminal because it is the source of the positive current[47-49].

1.6 Fundamental Parameters for LIBs

The measurement of battery performance for both the anode and cathode is often described in terms of capacity per unit mass or per unit area of the electrode material. Capacity, in this context, refers to the maximum number of amperes-hours that can be recovered from a fully charged cell during the process of discharging. This section

provides an explanation of the charge/discharge capacity and other terms commonly employed in batteries, including charge-rate, cycle life, and coulombic efficiency

(a) Capacity or electric charge

The term "capacity" in the context of a battery refers to the amount of electric charge that can be stored and accessed by a specific active anode or cathode material within the cell or battery. This concept is commonly referred to as gravimetric capacity (expressed in Ah kg^{-1}) or volumetric capacity (expressed in AhL^{-1}). whereby Q denotes the electric charge, I represent the current, and t signifies time.

$$Q=I.t \qquad (1.1)$$

The theoretical capacity of any redox system i.e. of any active material is calculated by the Faraday's law of electrolysis

$$Q_{theo}= m.z.F/M = n.z.F \qquad (1.2)$$

Whereby, m represents and M denotes the molar mass of the respected sample, z represents the number of electrons participating in the redox process. However, n denotes the number of substances (in mol) and F is the Faraday constant.

(b) Charge capacity and discharge capacity

The charge capacity signifies the quantity of charges stored when a lithium-ion cell is charged. However, the discharge capacity represents the quantity of charge, which is attained during the discharge process of a lithium-ion cell.

(c) Overcharging

Overcharging is a phenomenon that arises when a charger persists in supplying electrical energy to a battery beyond its designated capacity or subsequent to the battery reaching its maximum charge level. Excessive charging has the potential to cause significant harm to the battery, including but not limited to severe damage, explosion, irreversible capacity loss, or leaking.

(d) Short circuit

Anomalous electrical connections occur when two nodes in an electric circuit, which are designed to have distinct potentials or voltages, are linked together. The probable consequences of this phenomenon include circuit damage, overheating, fire, or explosion.

(e) Open circuit voltage OCV)

Open circuit voltage (OCV) refers to the electrical potential difference between two terminals of a battery when it is not actively supplying or receiving any current, and when it is detached from any circuit.

(f) Coulombic efficiency (CE)

The Coulombic efficiency of a lithium-ion cell can be defined as the ratio of the discharge capacity (Qd) to the charge capacity (Qc) [50].

$$CE = Qd/Qc*100 \qquad\qquad 1.3$$

The coefficient of efficiency (CE) should be maximized to approach a value of 100%. A high coulombic efficiency is indicative of strong reversibility and suggests minimal ion loss resulting from undesired side reactions.

(g) Irreversible capacity, irreversible specific charge (Qirr) or charge loss

The term "irreversible capacity losses" refers to the disparity between the charge and discharge capacities during a single cycle, hence establishing the charge capacity that cannot be fully restored upon discharge. Therefore, in order for the lithium-ion battery (LIB) cell to be practically applicable, it is imperative that the value of Qirr is minimized. [51].

$$Q\ irr= Q\ charge\ -Q\ discharge \qquad\qquad 1.4$$

The equation for the net charge (Q irr) is equal to the charge when charging (Q charge) minus the charge during discharging (Q discharge)

Open circuit voltage (OCV) refers to the electrical potential difference between the two terminals of a battery when it is not actively supplying or receiving any current, and when it is detached from any circuit.

(h) Charge rate or C -rate

The C-rate of a battery or cell refers to the rate at which the battery is charged or discharged, expressed as a ratio of the battery's capacity to the time taken to complete a full charge or discharge cycle. The C-rate denoted as 1C signifies the full charge or discharge of a battery within a duration of one hour. Conversely, a C-rate of 10C indicates that a single charge or discharge cycle will be accomplished within a time frame of 1/10 hour.

(i) Specific power and power density

The amount of power delivered by a battery expressed per unit mass or per unit volume is termed as specific power and power density and given as

Specific power (WKg^{-1}) =SE/t

Power density (WL^{-1}) =ED/t

Where SE represent specific energy and ED represent energy density.

1.7 Anode Materials for LIBs

When a lithium-ion battery is being charged, the anode will intercalate lithium ions, and when the battery is being discharged, it will de-intercalate lithium ions. Although the name "anode" is commonly used for the negative electrode in lithium-ion batteries across the scientific literature, this designation is only accurate when the battery is being discharged. The following are some of the most important criteria that must be met by a substance before it can be utilized as an anode in a lithium-ion battery.

- The reaction potential of the anode should be very low so that the battery's potential can be raised to a higher level.
- In order to have a high specific capacity, the material must have an adequate number of vacancies that are capable of accommodating the greatest possible amount of lithium ions.
- The anode material should have a structure that is robust enough to withstand repeated lithium intercalation and deintercalation without suffering any structural damage.
- The material should maintain its chemical stability across the whole temperature range of its operational environment and while subjected to high power states.
- The material needs to be simple to work with and inexpensive.

1.7.1 Alloy-based anode materials

Alloy anodes possess high energy capacity ,are considered to be competent anode materials for lithium ion batteries [52]. Certain metallic elements (M = Si, , Pb, Sn, As, Sb, Bi, , In, Ge, Cd, Zn and Pt and Au) have a propensity to react with lithium to generate lithium metal alloys of the LixMy type. These lithium metal alloys can be distinguished by their high lithium content.'

$yM + xLi^+ + xe- \leftrightarrow LixMy$
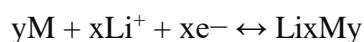
When battery is being charged, lithium ions are taken up by the anode, which results in the formation of an intermetallide. On the other hand, when the battery is being discharged, the anode dissolves, which results in the release of lithium ions. The theoretical specific capacities of the alloy anodes are two orders of the magnitude larger than those of the graphite electrodes that are employed in commercial applications. On the other hand, alloy-based anodes have a quick decline in capacity during cycling as a result of the substantial volume changes that occur while transitioning from pure metals to metal alloys[53] . When compared to the 10% variance in volume that LiC_6 exhibits, the volume of certain alloy-based anodes can grow by many orders of magnitude. The reason for this is that the atoms of the metal expand to more than three times their normal size when lithium ions are added to an alloy to make it, and then they contract when the lithium ions are removed. After a few cycles of intercalation and deintercalation, the structure of the metal begins to break down, and it is unable to effectively house lithium ions [54, 55].

1.7.2 Transition metal oxide anode materials

TMOs have received a significant attention as a potential anode material for lithium-ion batteries as a result of their high theoretical gravimetric capacity (800–1200 mAh g^{-1}) and high density (5–7 g cm^3) as compared to the graphite anode that is often utilized in commercial applications (372 $mAhg^{-1}$, 2.21–2.26 g cm^3). In the year 2000, Tarascon et al. announced a variety of TMOs that can be used as anode material for lithium-ion batteries.

The mechanism that underlies the reaction that occurs when TMOs and lithium ions interact is somewhat distinct from the mechanisms that underlie the reversible intercalation/deintercalation reaction and the lithium alloying reaction. The majority of 3d-TMOs crystallize in a rock salt structure, which has essentially no vacant sites for lithium ions to occupy. Furthermore, these TMOs are considerably less reactive toward lithium in terms of their ability to form alloys. These two factors account for the difference. In point of fact, the TMOs use a displacive redox mechanism to carry out the electrochemical reaction, which requires the synthesis of Li_2O as well as its subsequent decomposition.

$$M_xO_y + 2yLi+ + 2ye^- \leftrightarrow xMo + yLi_2O$$

Furthermore, the decomposition of inactive Li_2O can only be accomplished when working with materials on the nanoscale, as this scale has a significant impact on the

chemical and physical events that occur. When the size of the particles is reduced to the nanoscale, a greater proportion of the total number of atoms can organize themselves on surface of the particles, leading to an increase in the electrochemical reactivity of the particles. There have been previous attempts made to use certain TMOs. These TMOs include ZnO, Co_3O_4,, Fe_2O_3, FeO_4 , NiO , CuO , and Cu_2O . The findings are very promising; nevertheless, the extreme volume fluctuations that occur during cycling result in a pulverization problem. This problem disrupts the electrical contact, which in turn results in a quick loss in capacity[54-61].

1.7.3 Carbon/graphite as anode materials

A lot of carbon-based materials, in a variety of forms, have been utilized frequently as electrode materials in batteries. Graphite has been utilized as a negative electrode in rechargeable lithium-ion batteries ever since the introduction of the very first lithium-ion battery designed for commercial use in the year 1990. In comparison to the vast majority of TMOs, chalcogenides, and polymers, graphite has the benefit of possessing greater specific charges in addition to larger negative redox potentials (0.5V vs. Li/Li^+). Because of its excellent dimensional stability, graphite has a far longer cycle life than anodes based on metal alloys, so it's a superior choice for batteries. Based on the equation 1.5, the theoretical capacity of graphite is calculated to be 372 mAh g^{-1}.

$$Li+ + 6C + e- \leftrightarrow LiC_6 \qquad\qquad 1.5$$

The carbon atoms in graphite are organized in the shape of hexagonal sheets and graphite has a layered structure. The layers, also known as graphene layers, are held together in an ABABAB…. stacking at an interplanar spacing of 0.335 nm by the weak van der Waals forces that are present along the c-axis two adjacent carbon layers in LiC_6 are directly confronted by one another. Lithium ions that are resident in the graphene layers organize themselves at a distance of approximately 0.430 nm from one another so as to reduce repulsion.

1.8 Limitations of Graphite-Based Anodes

The use of an anode that is based on graphite is quite widespread in commercial lithium-ion batteries. The fact that this anode has a low energy density (372 mAhg^{-1}), which is directly related to its operating principle, is one of its most significant shortcomings. When lithium ions fill the graphene layers, they do so in a way that prevents them from occupying interstitial spots that are directly close to one another. As a consequence of

this behavior, lithium ions are present in alternate hexagonal carbon positions within the graphene layer. This behavior results in the optimal arrangement of one lithium atom for every six carbon atoms.

The redox potential for Li intercalation into graphite is greater than the electrolyte stability, and preventing the development of the SEI is a significant challenge that must be met. During the first charge of the battery, a charge-consuming side reaction takes place on the graphite electrode. Additionally, the solvent co-intercalation promotes the expansion of graphene layers, which ultimately leads to a loss of capacity as a result of structural defects. The effectiveness of graphite as an anode across multiple cycles, rather than its capacity, is the primary factor contributing to its widespread use in the market. Because of this, lithium-ion batteries stand to benefit significantly from an increase in this value.

1.9 Group VIB as anode materials for LIBS

The purpose of the project was to develop anode materials based on transition metal oxides hybrid composites for rechargeable batteries (lithium-ion batteries). The transition metals are chosen from group 6B including Tungsten (W), Molybdenum (Mo), Chromium (Cr) etc., because of their distinctive electronic, optical, catalytic, and electrochemical properties. These materials have a layered structure, resembling graphite, which enables the insertion of Li-ion and exhibits a wide range of chemical properties, as well as distinct electrical, chemical, mechanical, and thermal characteristics.

1.9.1 Molybdenum trioxide (MoO_3)

Molybdenum trioxide is a significant transition metal oxide derived from molybdenum, a member of group VI-B in the periodic table, positioned below chromium. Compounds derived from molybdenum exhibit complex chemical behavior due to the diverse range of oxidation states (-2 to +6) and coordination numbers (0-8) that molybdenum metal can adopt. Moreover, molybdenum has a low level of toxicity. Additionally, it falls under the lowest category in the most recent classification of possibly carcinogenic substances [62].

MoO_3 exist in different crystalline phases most common of which include orthorhombic, and hexagonal crystal structures as shown in Fig 1.7.
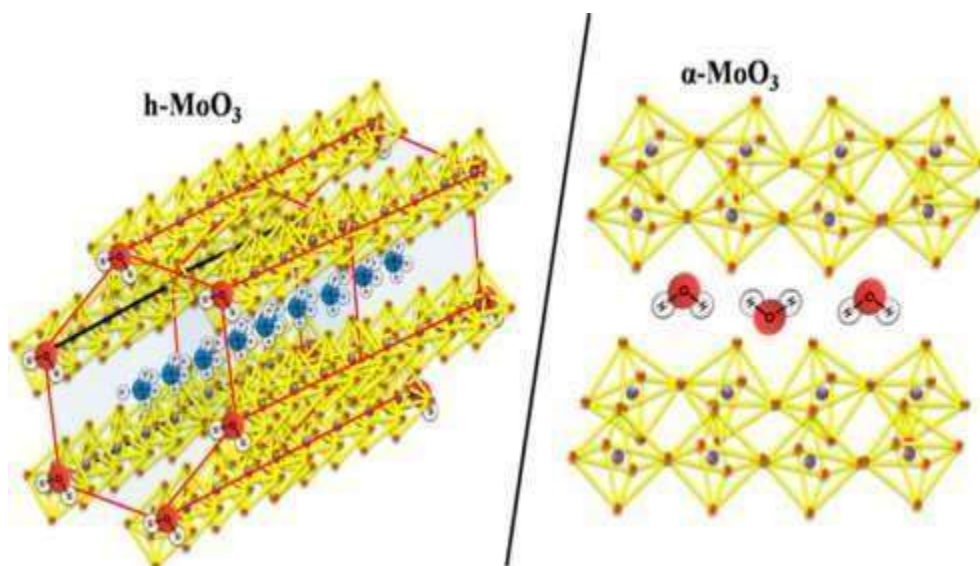
Figure 1.7 Structure of h-MoO$_3$ and α-MoO$_3$[63]

The basis building unit of all these structures is distorted MoO$_6$ octahedra, which shows a transitional stage between octahedral and tetrahedral coordination. Four oxygen atoms surround molybdenum atom closely at bond distances of 1.94, 1.95, 1.73 and 1.67Å forming MoO$_4$ tetrahedra, while two oxygen atoms are present at longer distances of 2.25 and 2.23 Å leading to formation of distorted MoO$_6$ octahedron. More distorted octahedron causes increased dipole moment and easy separation of charges during electrochemical reactions[64]. The repetition and combination of this octahedron in different arrangement led to the formation of different crystal phases.

It is widely regarded as a highly promising candidate for a range of technological applications, such as energy storage devices, chromic devices, solar cells, catalysis, and gas sensors [65].

Orthorhombic α-MoO$_3$ is formed when these MoO$_6$ octahedra are joined together with each other by covalent forces along the edges to form zigzag rows and these rows are further connected by corners to fom layers in ab plane. These layers are alternatively stacked with each othr along c-axis. Between these layers weak vander waal forces exist which reflect an interlayer distance of 6 Å[64] . The bond at unshared position terminates by forming Mo=O along c-axis, while the layers are connected through bridging O-Mo-O bond[66-70].

Metastable form of MoO$_3$, which undergo conversion to stable orthorhombic MoO$_3$ around 430°C is known as hexagonal molybdenum trioxide (h-MoO$_3$) and is formed by connecting zigzag chains of MoO$_6$ octahedra through c-axis with the help of structural

20

directing moieties, giving rise to a 3D lattice. This leads to hexagonal tunnels with radium of sphere 1.5-1.6Å, which are stabilized by intercalated ions such as Li^+ ions[63]. Due to unique structure, the formation of this phase is extreme interest because it provides various intercalation sites for ion storage such as hexagonal tunnel and square along with trigonal cavity. Also, the tunnel structure increases the hole and electron separation and facilitates its rapid transport towards substrate. The formation of orthorhombic α-MoO_3 occurs through the covalent bonding of MoO_6 octahedra along their edges, resulting in the arrangement of zigzag rows. These rows are then interconnected through corner sharing, leading to the formation of layers inside the ab plane. The layers are arranged in an alternating manner along the c-axis. Weak van der Waals forces are present between these layers, resulting in an interlayer spacing of 6 Å [34]. The link at the unshared position is terminated by the formation of a Mo=O bond along the c-axis, while the layers are joined through a bridging O-Mo-O bond. h-MoO_3 exhibit superior properties in comparison to its layered counterpart because more paths are provided for the ions movement in contrast to single direction therefore, it can as excellent electrode material for lithium ion battery because it possess theoretical capacity of 1117mAhg^{-1}, which is three times higher than the commercial anode used for LIBs (graphite showing capacity of 327mAhg^{-1}).

The charge transfer behavior of both these phases was studied by chithambararaj et al. whose results revealed 550 times higher conductivity for h-MoO_3 than α-MoO_3. They suggested an ion diffusion model for h-MoO_3 with polarization model for alpha MoO_3 as represented in Fig 1.7. The latter show resistive behavior because conduction only takes place through polarization. i.e. the hop of charge carriers from one site to other whenever it overcome the potential barrier which is developed between two sites separated by some distance. In case of h-MoO_3 conduction occurs both through polarization as well as in diffusion because the structure contains intercalated water and ammonium ions , which can freely move in various cavities and tunnel present in h-MoO_3[63].
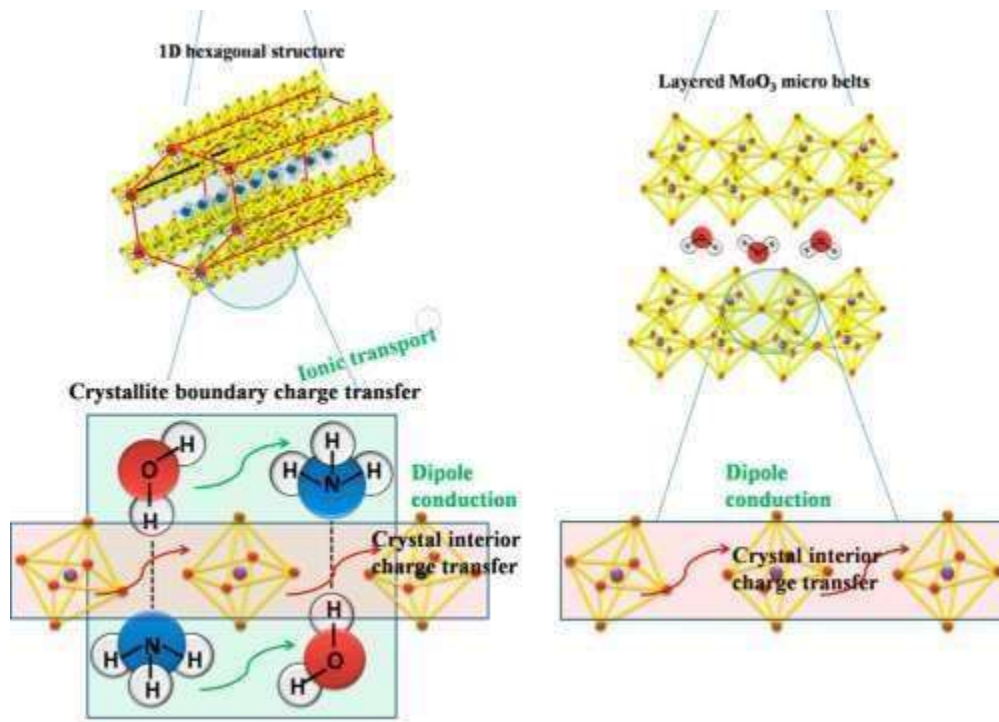
Figure 1.8 Charge transfer mechanism of α and h-MoO$_3$[63]

Various studies have been reported, which employed MoO$_3$ as anode materials for lithium-ion batteries. Li et al prepared α-MoO$_3$ micro belts, which sowed high capacity of 344.5 mAhg^{-1} with low initial columbic efficiency of 41.18%. Initially the capacity decreases and stabilizes at 300mAhg^{-1}, which was ascribed to volume expansion of the electrode. Hariharan et al. also evaluated the performance of α-MoO$_3$ with block morphology, which delivered reversible capacity of 410mAhg^{-1} with initial columbic efficiency of 53% with good cycling stability after initial degradation.

In their study, Liu et al. synthesized a composite material by including graphene, and observed a significant decrease in capacity from 386.7 mAhg^{-1} to 23 mAhg^{-1} after 50 cycles at a rate of 100 mAhg^{-1} for pure MoO$_3$. The researchers attributed this quick capacity degradation to the low conductivity and swelling of the electrode upon sodiation. [71]. In a study conducted by Zhou et al., it was observed that h-MoO$_3$ nanorods exhibited promising performance as anode materials for lithium-ion batteries (LIBs). Specifically, these nanorods shown a capacity of 780 mAhg^{-1} after undergoing 150 cycles at a rate of 150 mAhg^{-1}. Notably, this capacity was found to be higher than that reported for α-MoO$_3$ in certain previous publications [72].

The researchers faced challenges related to the material's low intrinsic conductivity, as well as issues with volume expansion and low initial columbic efficiency. The aforementioned challenges can be effectively addressed through the implementation of

many approaches, including cationic doping to enhance the intrinsic conductivity of the material, integration of carbon nanomaterials, and application of polymer coatings.

1.9.2 Tungsten oxide (WO$_3$)

Tungsten oxide and its compounds exhibit variety in their structures. They show distinct stoichiometry's among various forms of the tungsten oxide, WO$_3$ has been considered to be very capable and versatile electrode material for primarily and energy-storage applications. Usually, WO$_3$ is complicated material owing to its different crystal structures, thermal stability such as triclinic, cubic, tetragonal, monoclinic, hexagonal and orthorhombic with nonstoichiometric and stoichiometric WO$_3$. Furthermore, WO$_3$ compounds has been synthesized via numerous techniques showing many structural properties that can be changed on thermal treatment. Due to its sub stoichiometric phase transitions and structural transformation, WO$_3$ has captivated important attention in present years to examine potential in diverse applications. Crystal structures of WO$_3$ depends upon temperature. As the temperature changes crystals exist in different polymorphic forms like monoclinic, tetragonal, orthorhombic and triclinic. Some Crystal structures are shown in Fig 1.9. Monoclinic I (g-WO$_3$) is very stable phase observed at room temperature, For monoclinic the distance among two neighboring atoms of tungsten is 0.375 nm and each unit cell accommodate eight WO$_6$ octahedra. If monoclinic WO$_3$ is hardened at high temperature, it changes to another crystalline forms (tetragonal and orthorhombic). However, it cannot come back to another phases when it come back to room temperature. This transformation from monoclinic to orthorhombic is distinguished by a decrease in bond displacement of W-O along (001) direction, which might shift the W atoms by tilting of WO$_6$ octahedral. Monoclinic and Triclinic WO$_3$ are the two transformations of WO$_3$ at low temperatures. These two phases are stable thermodynamically and exhibit many important physicochemical properties. Tungsten show broad range of the oxidation states of -2 to +6 and rich electrochemistry. Through an electrochemical route tungsten can transform into numerous oxides of tungsten. WO$_3$ are the main class of transition-metal oxides (TMO) that show high electrical conductivity and good specific capacity values compared with the conventional electrode materials. Their physicochemical properties make better electrode materials for numerous applications[73, 74]. Even though tungsten oxides have excellent charge storage properties due to several transition states, current investigations have demonstrated that WO$_3$ based materials often have a large

irreversible capacity, poor rate capability, energy shortage, low cycling stability and low coulombic efficiency. Anyhow, it is hard to say that these are completely linked to microstructures without comprehensive understanding their effects and causes. Anyhow, current reports in literature involve that volume change of an electrode material in charge de-intercalation/ intercalation reactions cause reduced energy-storage capability and a lower cycling stability. Unique physical properties and numerous useful features of WO_3 have made them cost-effective, outstanding and effective for energy storage devices.

(a) Simple cubic WO_3

(b) Monoclinic WO_3

(c)Tetragonal WO_3
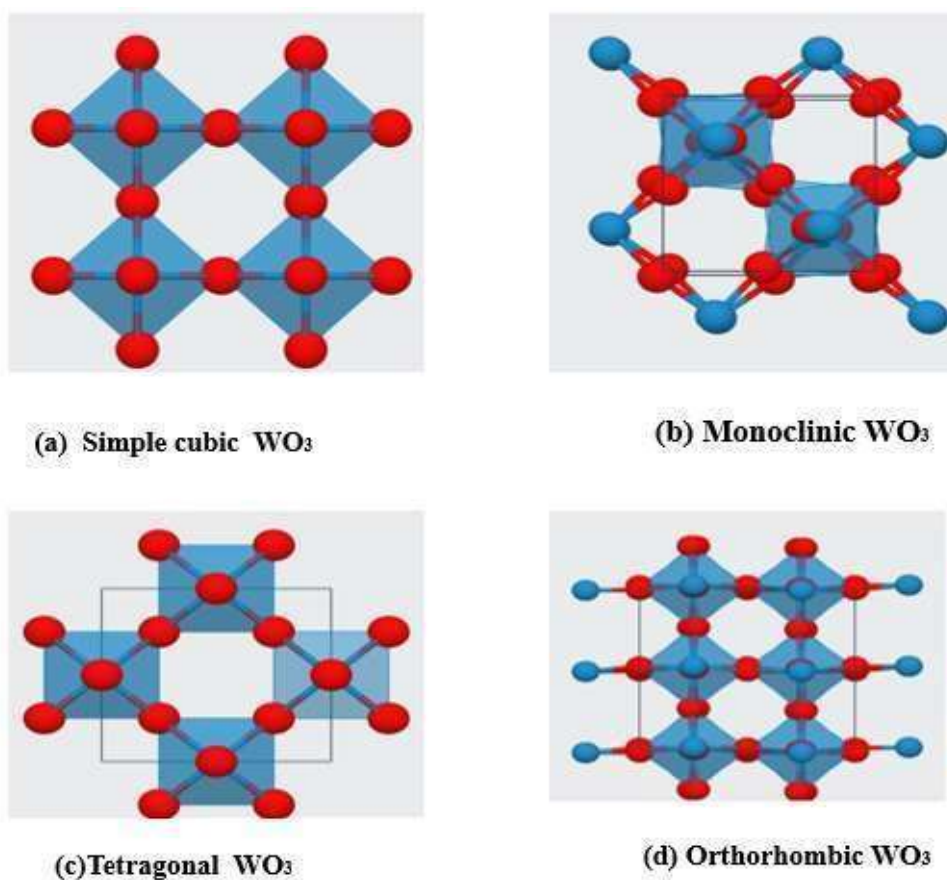
(d) Orthorhombic WO_3

Figure 1.9 a) Structural models of several structures of WO_3:, a) simple cubic, b) monoclinic at room temperature (c) tetragonal(d)orthorhombic structures (red and blue spheres represent W and O atoms, respectively).

Nanostructured WO_3 electrodes have generated broad research interest due to their attractive performance. WO_3-based electrodes have exhibited multiple transition states and high charge storage capacity in the course of electrochemical reactions. However, due to small specific surface area of WO_3 and poor electrical conductivity the electrochemical properties cannot be noticed efficiently. With For this aspect, researchers manufactured many nanostructured WO_3 along with its

24

composites with various conducting substances, which might enhance its performance[75]. Among different transition metals oxides, the tungsten oxide family, including WO_2, $WO_{2.9}$, $WO_{2.72}$, $WO_{2.8}$ and WO_3 has been extensively studied for LIB_S. More specifically, WO_3 have been extensively used as anode material for LIBs exhibiting theoretical capacity of 700 mAh/g [76], providing large crystal lattice spacing. Nevertheless, low conductivity of WO_3, poor capacity retention and large volume and structural variation during conversion and insertion of Lithium ions can collapse the lattice structure, resulting decrease in specific capacity. Therefore, numerous efforts have been put forward to overcome these obstacles. For selection of good anode materials high surface area and mesoporous nature of material is necessary, which provide storage sites and facilitate Li^+ ion transport in electrolyte. WO_3 has different polymorphs, including cubic, tetragonal, hexagonal, triclinic, orthorhombic, and monoclinic structures as shown in Fig 1.9.[77].

To tackle these problems, nanocomposites were prepared with reduced graphene oxides. Carbon based 2D anode materials such as reduced graphene oxide RGO is becomes the forefront of research. The RGO having excellent electronic conductivity, high stability, best electrochemical properties and provides large surface area for intercalation and deintercalation of Li^+ ions during cycling process as compared with TMOs. The nanosized ability, high aspect ratio, large surface made them very useful in different fields of nanoscience[78].

1.9.3   Chromium oxides (Cr_2O_3)

The compound chromium (III) oxide (Cr_2O_3) has gained a considerable interest as a promising anode material in recent research. This is mostly due to its distinctive properties, including a high theoretical capacity of 1058 $mAhg^{-1}$ and a relatively low voltage required for lithium insertion, measured at $1.085V$[79-81]. The surface morphology of this material shows a significant correlation with its electrochemical performance as electrode material. Previous studies have reported that the presence of defects and vacancies in this material has a substantial impact on enhancing the electrochemical activity and other characteristics of the electrode[82-84]. A significant benefit of employing Cr_2O_3 as an electrode material for lithium-ion batteries (LIBs) is its charge storage mechanism, which is based on a conversion reaction.
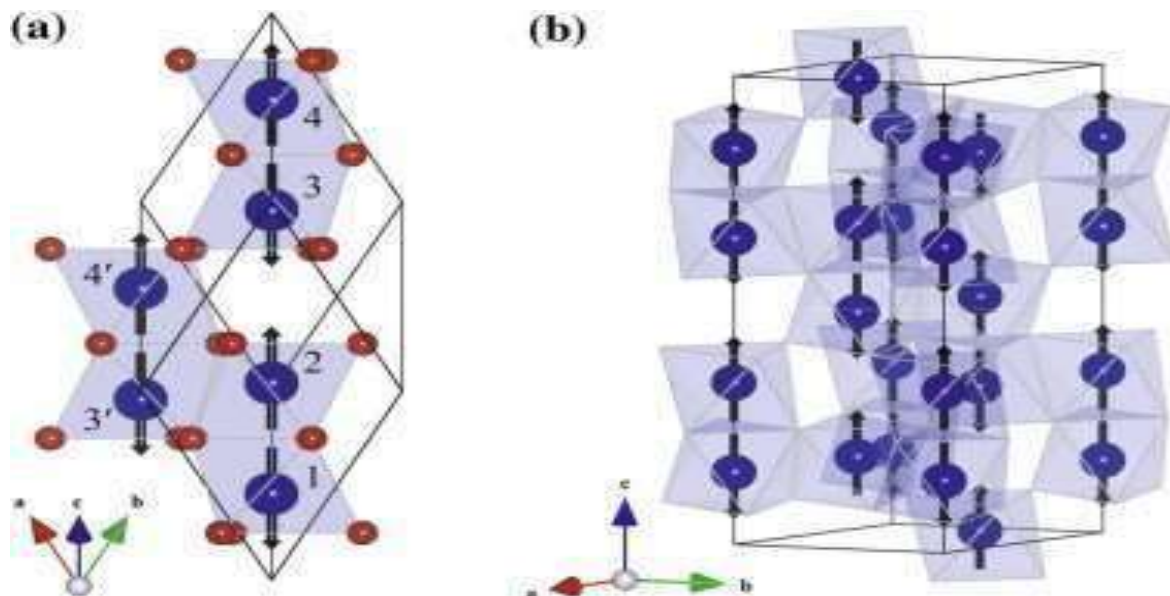
Figure 1.10 (a) rhombohedral (fractional co-ordinates between; x = 0 and 1; y = 0.5 and 1; and z = 0 and 1), and (b) hexagonal unit cell of Cr_2O_3 showing the magnetic moment arrangement[85].

This mechanism results in a considerably higher energy density compared to conventional electrode materials that typically rely on intercalation reactions for charge storage [82, 83]. To enhance the charge storage capacity of lithium-ion batteries (LIBs), it is imperative for metal oxide-based materials to exhibit several crucial material characteristics. These include a controlled mesoporous structure, a high surface area, a reduced grain size, and an increased number of active sites to facilitate rapid conversion/reconversion reactions. The conversion reaction for Cr_2O_3 can be expressed as:

$$Cr_2O_3 + 6e^- + 6Li^+ \rightarrow 2Cr^0 + 3Li_2O$$
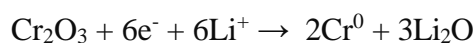
which leads to high theoretical charge storage capacity as compared to the common graphitic carbon electrode (372 mAhg^{-1}) that involves intercalation/deintercalation mechanism given as: $C_6 + xe^{-1} + xLi+ \rightarrow Li_xC_6$ [85-87].

1.10 Strategies to Improve Performance of Anode Materials

During cycling, a major issue with transition metal oxides is pulverization and cracking, which causes aggregation and dispersion in electrode material. In order to cope with these kinds of problems, multiple strategies have been applied to improve electrochemical performance, mechanical strength, surface area, electron and mass transport kinetics and conductivity of TMOs, such as designing nanostructures,

introducing conductive agents and engineering defects [88]. TMOs have been converted into various forms such as nanowires, nanorods, nanobelts [89], nanofibers and nano sheets [90]. The small size of nanoparticles shortens Li^+ diffusion path and the large surface area provides active sites. Furthermore, one of the most important approaches to increase electronic conductivity of TMOs and to improve Li^+ ion diffusion and electronic conductivity, carbon materials and matrices have been introduced into TMOs such as carbon nanotubes(CNTs), carbon black (graphene) [91] and polyaniline (PANI). Moreover, the conducting polymer also provides the conducting backbone, which increases the lithium-ion conductivity, stability and electrochemical performance of the electrode[92]. Polymer materials such as polypyrrole (Ppy) and polyaniline (PANI) have been coated and the performance has improved. Recently, nanocomposites of TMOs with polypyrrole were synthesized and the nanocomposites exhibited good cycling stability and electrochemical performance in lithium-ion batteries, signifying the successful use of the polymer. Polyaniline is considered another polymer for a potential conductive polymer due to its environmental stability, easy synthesis and high conductivity. PANI has a function of improving conductivity and stabilizing the structure. Cai et al. utilized nest-like PANI that reduced volume changes to increase electrochemical performance of Si-based anode materials. Wu et al. prepared a 3D hydrogel conducting network by in situ polymerization that demonstrated good cycling performance. Furthermore, PANI coating on the surface of TMOs acts as a good anode material for a Li^+ ion host. Moreover, carbon also acts as a buffer that reduces the stress owing to a large volume of expansion during the charging–discharging by enhancing the electrical conductivity of anodes. Furthermore, carbon increases the structural stability by surrounding the active material particles because it prevents active material aggregation during cycling. However, comparatively, CNTs displayed a good rate capability and cyclic stability over carbon. Conductive carbonaceous materials such as CNTs and reduced graphene oxide (RGO) have been used with TMOs, which can improve conductivity and structural stability, thus increasing the overall electrochemical performance[93, 94].

1.10.1 Carbon nanotubes (CNTS)

Carbon nanotubes (CNTs) have been the subject of intense research since their discovery in the late 20th century due to their notable characteristics, including high electrical and thermal conductivities, as well as strong mechanical qualities. They are

defined as one-dimensional allotropes of carbon due to their growth occurring solely along a single dimension, namely length. The remaining two dimensions are confined to the nanoscale and are achieved through the process of rolling graphene sheets.

Carbon nanotubes (CNTs) can be categorized into two distinct groups based on the number of graphene layers they consist of, namely single-walled carbon nanotubes (SWCNTs) and multi-walled carbon nanotubes (MWCNTs). Single-walled carbon nanotubes (SWCNTs) are fabricated through the process of rolling a single graphene sheet, resulting in cylindrical structures with outer and inner diameters ranging from 0.4 to 2 to 3 nm. These nanotubes typically exhibit lengths in the micrometer range. On the other hand, multi-walled carbon nanotubes (MWCNTs) are produced by rolling multiple layers of graphene sheets, resulting in nanotubes with diameters ranging from 2 to 20 to 30 nm. The lengths of MWCNTs can vary from micrometers to centimeters. The characteristics of carbon nanotubes (CNTs) exhibit variations based on factors such as the angle of rolling, number of walls, and length[95-97]. The angular displacement of the rolling angel, situated between the hexagon and tube axis, is referred to as the chiral angel. This parameter ranges from 0 to 30° and is dictated by the chiral vector. The chiral vector in the context of graphene can be expressed mathematically as $Ch = na1 + ma_2$, where a1 and a_2 represent the base cell vectors of the hexagonal lattice structure of graphite. The variables m and n correspond to the number of hexagons in two directions of the graphene sheets. Based on the values of these indices, three distinct types of single-walled carbon nanotubes (SWCNTs) can be identified. Specifically, when m is equal to zero, the SWCNTs exhibit a zigzag configuration. Conversely, when m is equal to n, the configuration transforms into an armchair shape. Finally, when m does not equal zero or n, the SWCNTs are classified as chiral, as depicted in the accompanying Fig 1.11.

There are two models that can be used to explain the structure of MWCNTs. These models are the parchment model and the Russian Doll model. In the parchment model, a single sheet of graphene is rolled up like a piece of paper, but the diameter of the inner tube that is inserted inside another layer of SWCNTs does not match. When compared to SWCNTs, they are considerably more robust and inert due to the fact that the outside wall serves to screen and protect the inner wall. The chirality of the SWCNTs determines the electrical properties that they exhibit. When the criterion n-m=3q is satisfied, they exhibit conductivity similar to that of a metal. On the other hand, when

n-m=3q+1 is satisfied, they exhibit semiconducting behavior, where q is an integer. MWCNTs are made up of numerous SWCNTs, and because at least some of those SWCNTs have metallic properties, MWCNTs themselves are metallic in nature and are unaffected by chirality.
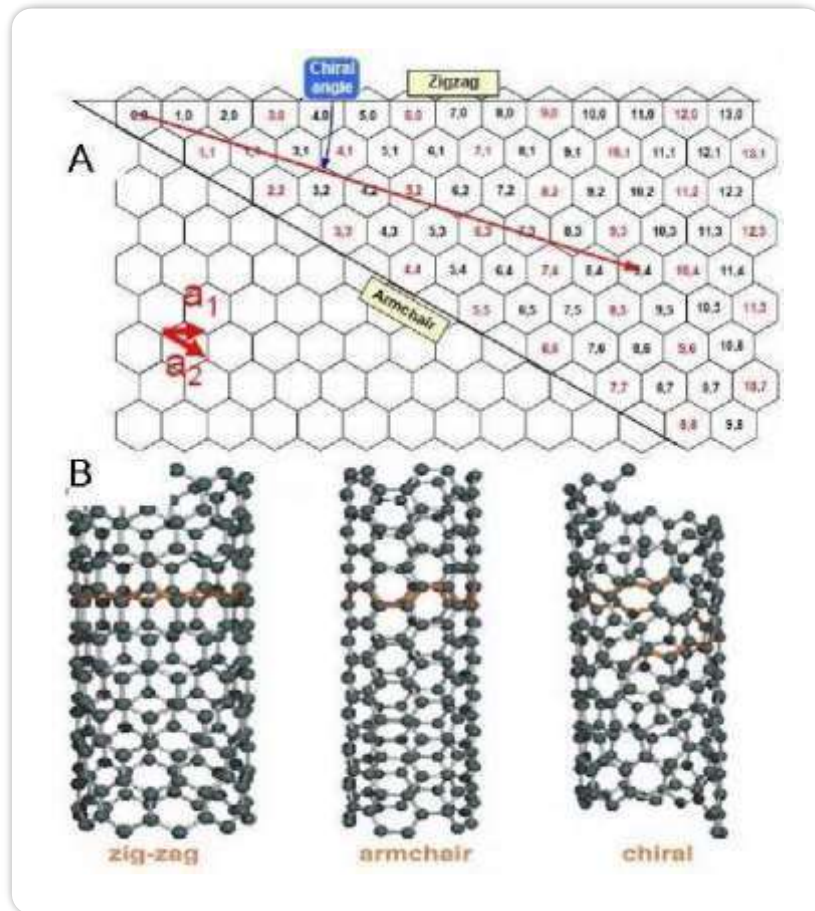
Figure 1.11 Chirality of SWCNTs[98]

However, the conductivity of MWCNTs is inhomogeneous due to the presence of semi-conductive nanotubes as well. The conductivity of carbon nanotubes can be traced back to the presence of delocalized electrons throughout the structure of the nanotubes. CNTs have exceptionally high mechanical qualities and considerable flexibility thanks to the presence of strong covalent connections between the carbon atoms in their structure. This enables them to keep their structure even when subjected to a variety of stressors. SWCNTs have been seen to have a young modulus of 1.25, whereas MWCNTs have been observed to have a young modulus of 1.8TPa, which is 9 times higher than alloyed steel. Both CNMs have promising electrical and mechanical properties, and as a result, they are considered to be effective materials. These materials can help solve the low conductivity issues that are associated with transition metal oxides by providing

channels via which ions and electrons can be transported. Because these materials have strong mechanical properties, they will be able to accept the strain caused by ions intercalation. As a result, the swelling of the electrode will be reduced, at least to some amount, when cycling is performed.

1.10.2 Graphene

Graphene, as defined by characterized by a single layer of graphite. It is often analogous to a polycyclic aromatic hydrocarbon of quasi-infinite size. In research, materials with a thickness of 10 layers or less are commonly referred as graphene, while those with more than 10 layers are classified as graphite.

(a) Single-layer graphene

(b) Multi-layer graphene

(c) GO

(d) rGO
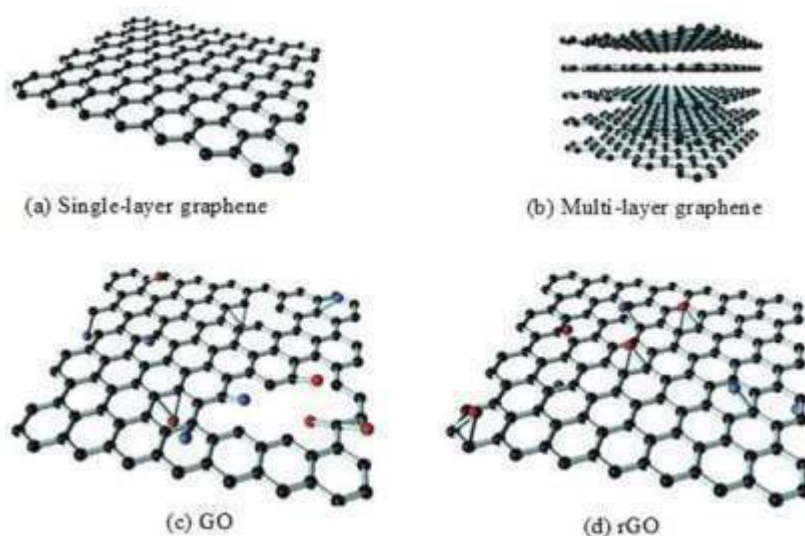
Figure 1.12 Single, bi and trilayer Graphene[85].

The distinction is based on the electrical conductivity characteristics exhibited by these materials. Graphene, which is regarded as the mother of all allotropes associated with graphite, is categorized as a two-dimensional nanomaterial due to its growth occurring in the dimensions of width and length (x and y), while its height remains within the nanometer scale. The fundamental architecture of many materials, including the formation of 1D carbon nanotubes through rolling, the creation of 0D Bucky balls through folding, and the stacking of layers resulting in the formation of 3D graphite, establishes a connection between the structure of graphene and that of graphite.

Each carbon atom in graphene layer undergoes sp^2 hybridization, which leads to the formation of 3 sigma bonds with adjacent carbon atoms forming flat hexagonal lattice, while leaving behind one un-hybridized p-orbital, which forms π-bond with the adjacent carbon atoms. These π-bond interact with adjacent graphene layers present

out of plane through vander waals forces in bi and few layers graphene. The structure of various types of graphene are represented in Fig 1.13.
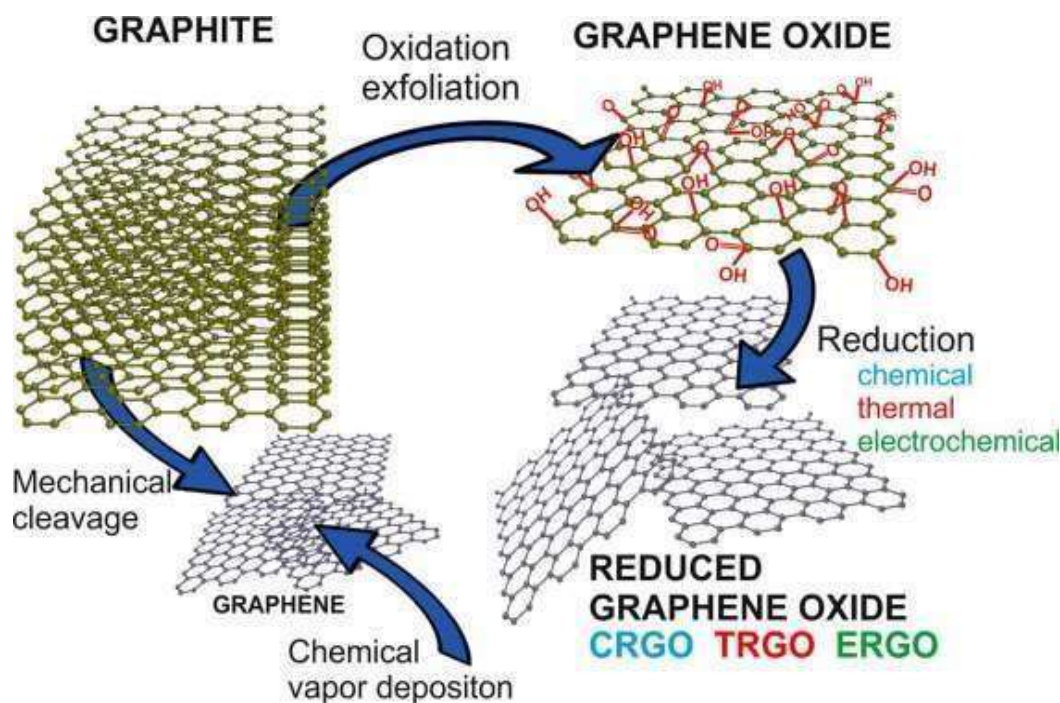
Figure 1.13 structure of Graphene and reduced graphene oxide

Single layer of graphene exhibit phenomenal carrier mobility of $>20,000$ cm^2/V sec^2 and electronic conductivity of 6000 S/cm^3 at room temperature and is classified as zero band gap semiconductor , because there is no energy gap between HUMO and LUMO of π -bond , which is also responsible for high carrier mobility , because it forms an electronic cloud that extends in 2D over the carbon atoms in graphene sheets. Band gap can be induced in single layer graphene by chemical modifications, while in case of bilayer graphene, disturbance in electronic cloud Causes an opening of 250 meV in the presence of electric field. The band structure for few layers graphene becomes complicated and imparts graphene the nature of a semi metal, where electric field can be used to control the extent of band overlap. The electrical properties of material with greater than 10 layers become similar to graphite showing maximum overlap between HUMO and LUMO orbitals.

Graphite exhibits superior mechanical properties, which can be attributed to the presence of short and strong covalent bonds present between carbon atoms. It is considered as strongest material having strength 300 times greater than steel and possess sheer and young's modulus of 280 GPa and 1000 GPa with intrinsic or fracture strength of 130 GPa, but structural defects such as presence of grain boundaries or disclocation decreases the intrinsic strength to 35 GPa.

Graphene production is difficult and expensive therefore, several compounds related to graphene are used in order to utilize its remarkable properties. Graphene oxide (GO) is considered as oxidized form of graphene in which the single layer of graphene is modified with oxygen containing functional groups. These functionality helps in easy dispersion of graphene oxide in solvent, but also makes it electrical insulator because of disruption of sp^2 character. Reduction of graphene oxide by thermal, hydrothermal or chemical method leads to the restoration of sp^2 character and increased conductivity of graphene oxide[99-103].

1.10.3 Conducting polymers

The application of a conducting polymer coating onto transition metal oxides is a widely employed technique aimed at improving both the inadequate electrical conductivity and cyclic stability. Additionally, it aids in the prevention of the dissolution of transition metal oxides into the electrolyte, hence mitigating the deterioration of capacity during cycling. In their study, Mohan et al. fabricated composites of polyaniline-coated MoO_3, which exhibited a specific capacity of $171mAhg^{-1}$, in contrast to the $92mAhg^{-1}$ seen in the unmodified sample, following 25 cycles. The performance of the system was ascribed to the electrical connections facilitated by polyaniline (PANI), even following repeated cycles. The polymers commonly employed in this context typically consist of polyaniline and polypyrrole. One advantage of the former option is its low cost in terms of precursor materials, as well as its ease of synthesis.

Polyaniline (PANI) is a widely studied and known polymer due to its fascinating properties such as easy synthesis, environmental stability and interesting redox properties. A chemical flexible amine NH functional group is present in a PANI which is on either side by a polyethylene ring.

Conductive polymers are defined as materials which possess electrical features of metals and mechanical properties of conventional polymers. PANI is also a conducting polymer known since 1862 and was called aniline black, a typical name given at that time to any product obtained from oxidation of aniline. The general structure for PANI is shown in figure and the variety of physiochemical properties exhibited by PANI is attributed to the presence of-NH- group. The structure of PANI was first of all depicted by green and Woodhead as a chain of aniline attached head to tail to each other at the para position of aromatic rings. The fundamental constituents' units of PANI are

benzenoid and quinoid units. Between each repeating benzenoid and quinoid moieties, nitrogen is present in form of mine and imine group. The amine nitrogen and imine nitrogen have either a free pair of electrons or an electron with positive charge respectively.
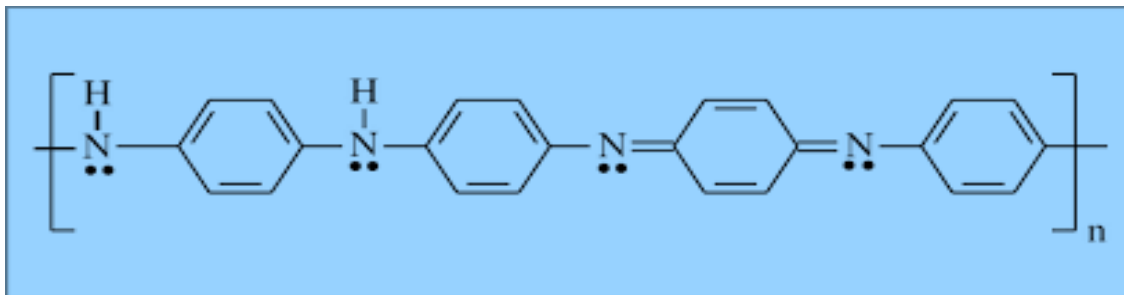
Figure 1.14 Structure of Polyaniline

It can exist in three different oxidation states known as leucoemeraldine which is the fully reduced state, emeralidine the intermediate state and per nigraniline, the fully oxidized state. These states are represented in Fig 1.15.

Doping can be used to variate the properties of polymer as it provides additional levels for the jump of electrons , rendering the material hole conducting or electron conducting depending upon the situation .Doping in polymers is different from that of semiconductors in a sense that doping in polymers occurs through charge transfer which can be reversed and is interstitial while in semiconductors it occurs through substitution and is irreversible , polymers doping is usually classified into redox, non -redox doping or doping byion implantation or heat treatment.

Non -redox doping which is defined as the process in which number of electrons associated with polymer chain remains the same while the properties are tuned from non-conducting to highly conducting from only by charge transfer when treated with protonic acid.

Emeralidine base treatment wih HCl was the first example of this type of doping which increased conductivity of emeralidine base now called emeraldine salt by 9 to 10 orders of magnitude from the undoped polymer. In this case the imine nitrogen is protonated and converted to radical cation in which spin and charge are delocalized over the polymer back bone. Polyaniline has the special feature that it can be doped by protonic acid which changes its properties and imparts electrical conductivity to the polymer.

The conductivity is governed by polaron or bipolaron. Thus coating conductive polymer over tranition metal oxides will increase its surface conductivity and will

impart path for migration of ions and electrons during cycling leading to better performance[66, 104, 105].
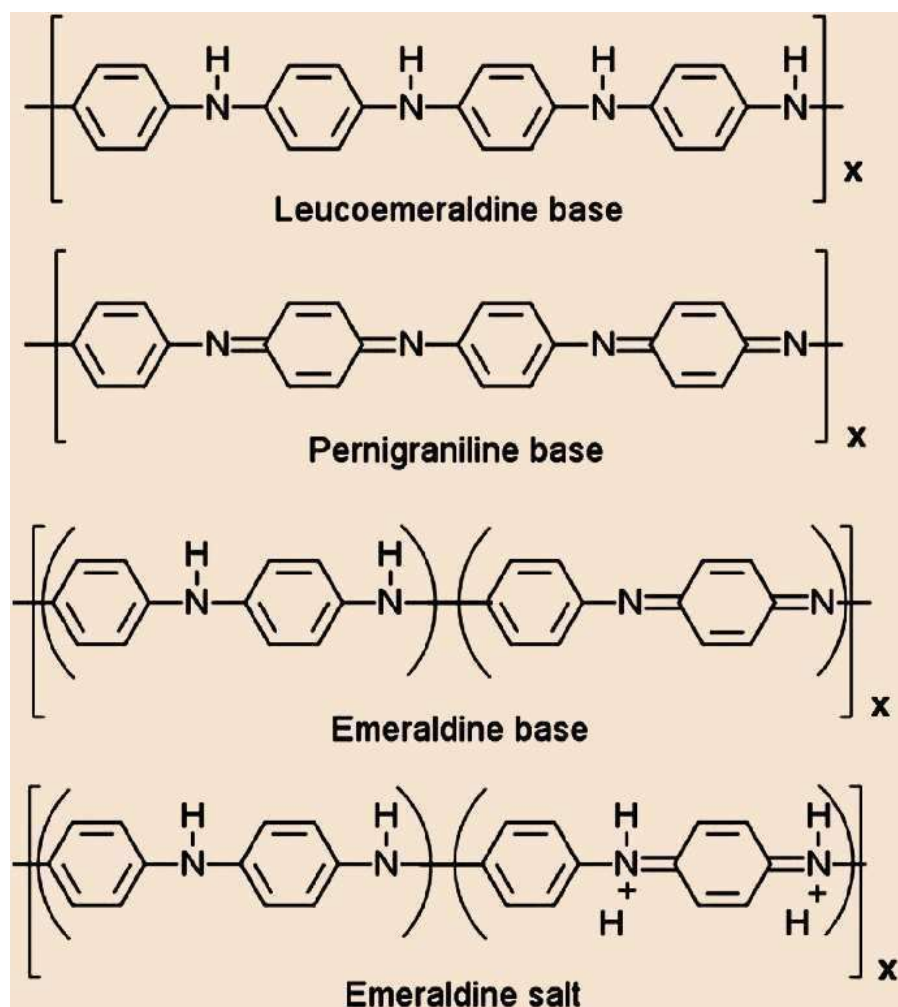
Figure 1.15 Different redox forms of Polyaniline[106]

Secondly, PANI coating was employed over WO$_3$ nanoparticles. Polyaniline (PANI) derived from polymerization of aniline, has specific optical and electrical properties, which can form five structures, nigraniline, pernigraniline, leucoemeraldine, leucoemeraldine and emeraldine. Polyaniline is a conductive polymer owing to its high conductivity, easy synthesis and environmental stability. Wu et al. prepared continuous 3D conducting hydrogel network by in situ polymerization, the Si-PANI hydrogel composites displayed stable cycling performance[107]. Conducting polymers have drawn considerable attention because they improve electrochemical performance. Polyaniline (PANI) is proved as one of the most promising conducting polymer owing to its simple synthesis, chemical and environmental stability, low cost and excellent electrochemical and physical properties owing to its high conductivity and small particle size, PANI

offers high surface area that is capable of high electron transportation, and hence improve the electrochemical performance[108].

1.11 SEI (Solid Electrolyte Interphase)

The SEI layer is multicomponent material formed through the irreversible decomposition of the electrolyte with electrode material. The SEI is characterized as a layer with a thickness ranging few angstroms to tens or hundreds of angstroms. This layer encompasses the active material particle, which experiences volume changes throughout the process of lithium-ion de-intercalation and intercalation. The cycle life of the battery could be affected if SEI layer get damaged as a result of the repeated expansion and compression of the material as it act as a protective coating around active materials particles [109].

The solid electrolyte interphase (SEI) is rapidly produced on the surface of lithium-metal when it comes into contact with the electrolyte solution, or during first charging process of the anode in a lithium-ion battery. This layer comprises of insoluble products resulting from the reduction process of the electrolytic solution and act as an interface between metal and the solution, exhibiting properties of solid electrolyte that restrict the passage of electrons.

When temperature of the cell surpasses the range of 70-100 °C, a phenomenon known as self-accelerated breakdown of the solid electrolyte interphase (SEI) initiates. Consequently, the temperature of the cell increases rapidly until it reaches a state of thermal runaway. Furthermore, it is worth noting that regenerative braking, particularly under low temperature conditions, exhibits a pronounced inclination towards the formation of lithium-metal dendrites on anode. This phenomenon internal short circuit and thermal runaway [110].

The formation of a passivation layer, known as SEI, occurs on the surfaces of electrodes by the decomposition of electrolyte components. The SEI (Solid Electrolyte Interphase) serves the purpose of facilitating Li^+ transit while impeding electron flow, hence mitigating electrolyte breakdown and promoting sustained electrochemical reactions.
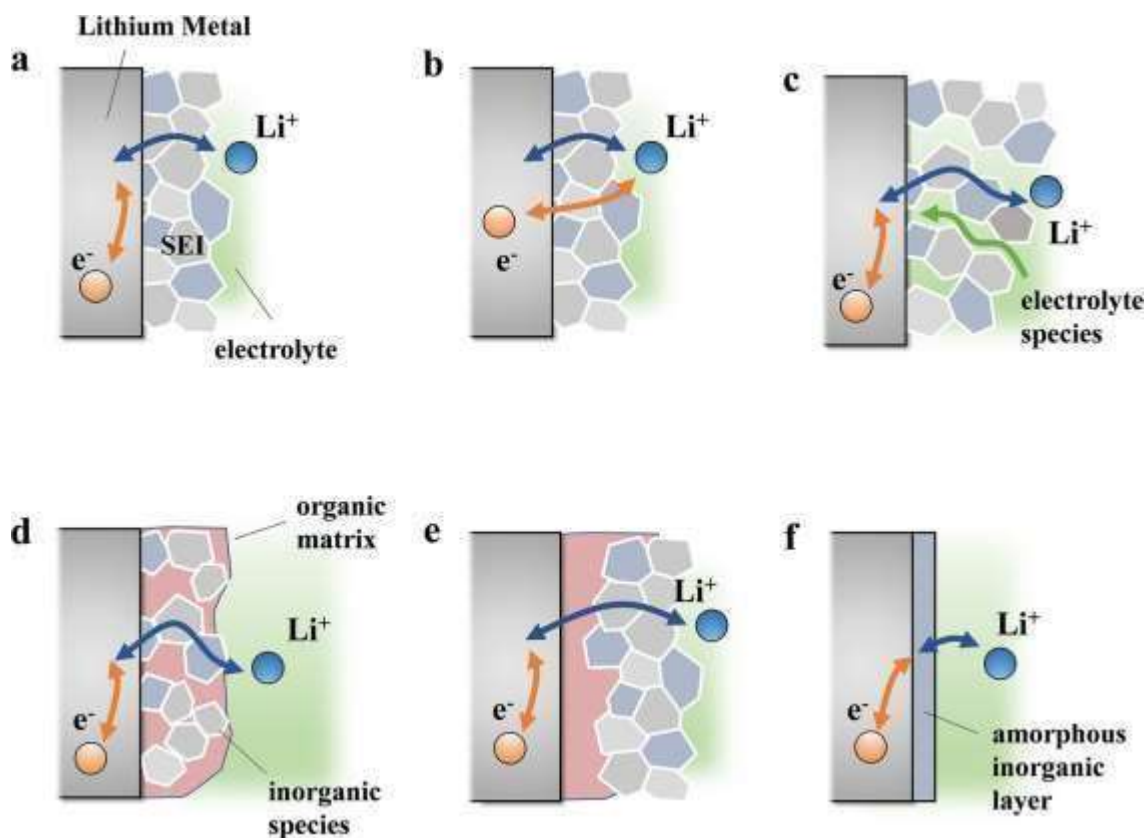
Figure 1.16 Possible morphologies and resulted charge transport across the SEI[111]

The thorough understanding of the creation and growth mechanism of nanometer-thick solid electrolyte interphase (SEI) films remains a challenge due to their complex structure and the absence of in situ experimental tools.

The remarkable progress in computational techniques has enabled the predictive modeling of the fundamental aspects of solid-electrolyte interphase (SEI). It is believed that the integration of computational modeling and experimental approaches can serve as a complementary strategy, facilitating a more comprehensive comprehension of the intricate solid-electrolyte interphase (SEI) phenomenon. This, in turn, holds the potential to advance the development of exceedingly efficient batteries in the future [112].

From a thermodynamic perspective, it can be observed that the majority of metals suffer from decomposition when they are exposed to oxidizing environment. However, metals mostly exhibit passivity on their surfaces, which limits their use as structural materials. The presence of a thin passivating coating on the surface of the metal serves to slow down the deterioration processes by providing a protective barrier. Passivation occurs when the formed film reaches thermodynamic equilibrium with the electrolyte, or when the kinetics of cation transfer from the resulting film to the electrolyte are slow enough

that the dissolution current becomes negligible. This protective mechanism shields the metal from dissolution, even if the passivating layer has not yet reached dissolution equilibrium. The passivation current density depends upon the electrode potential, as it can be elucidated by the increase of the oxidation state of the cations present on the surface of the layer. This, in turn, leads to a modification in the composition of the passivating film as the potential varies. Li metal is known to exhibit instability in various environments and when exposed to different electrolytes due to its significantly positive passivation potential. Indeed, previous studies have demonstrated that Li is prone to degradation, even when efforts are made to keep it within an inert environment.[111].

1.11.1 Influence of SEI on battery performance

The performance of batteries is significantly influenced by various parameters and properties of the solid electrolyte interphase (SEI). Several factors contribute to the characteristics of a material, including its composition, thickness, morphology, and compactness. The irreversible charge "loss" (ICL) observed in the initial cycle is a result of solvent reduction and formation of a solid-electrolyte interphase (SEI), thus indicating its association with SEI formation. The occurrence of detrimental processes during storage, specifically self-discharge upon the SEI's capability to passivate the surface of the active material. Therefore, the longevity of a battery is also contingent upon the solid electrolyte interphase (SEI). As previously stated, the SEI may undergo dissolution and/or transformation throughout the cycling process. Therefore, the establishment and maintenance of an efficient and durable solid electrolyte interface (SEI) is imperative for ensuring a prolonged lifespan of the battery in cycling applications. The significance of this factor is further heightened when cycling at elevated rates and deeper levels of discharge. The components of the Structural Engineering Institute (SEI) exhibit a significant degree of sensitivity to changes in temperature. The performance of the battery at high and low temperatures is contingent upon the solid electrolyte interphase (SEI). Nevertheless, the safety of the battery is the most significant outcome of SEI.

1.11.2 Features of ideal SEI

The kinetics of SEI production should be very quick in order to allow for its complete formation before the beginning of Li$^+$ intercalation. The potential for SEI formation

ought to be more positive than the potential for Li$^+$ intercalation. The perfect SEI would have a consistent morphology and composition throughout. It should comprise passivating agents that are stable and insoluble, such as Li$_2$CO$_3$, rather than metastable passivating agents like ROLi and ROCO$_2$Li, which are less effective. A strong SEI should be characterized by a dense layer that has strong adhesion to the carbon. It needs to be elastic and flexible so that it can tolerate non-uniform electrochemical behavior as well as the breathing of active material[113].

1.11.3 Properties of Solid Electrolyte Interphase

The optimal solid electrolyte interface (SEI) on lithium (Li) is characterized by its excellent ionic conductivity, electronic insulation, chemical stability against Li, and ability to prevent direct contact between Li and the electrolyte, even when subjected to substantial mechanical strain resulting from morphological changes.
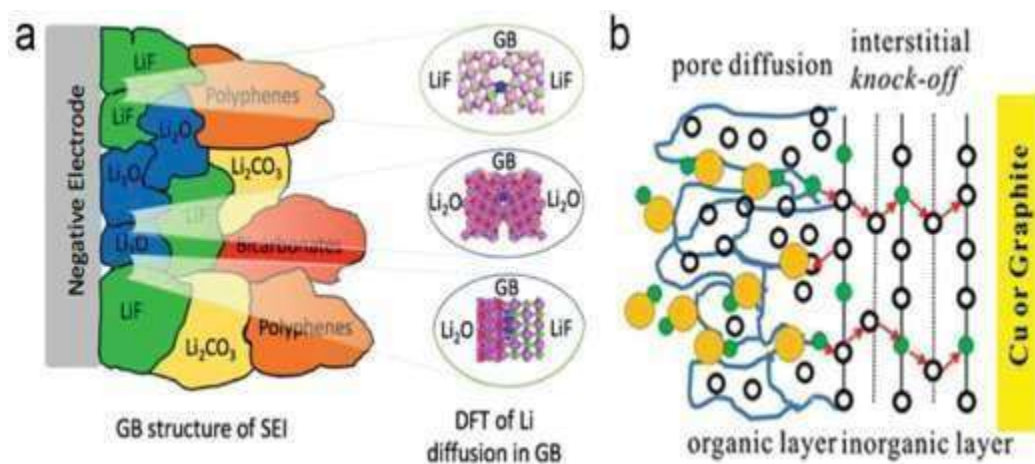
Figure 1.17 Li$^+$ ions transport through grain boundaries, two-layer/ two-mechanism model[114].

The relationship between the structure and chemical composition of the solid electrolyte interphase (SEI) is widely recognized as a crucial factor in determining the properties of the SEI. Nevertheless, a comprehensive correlation between the structure and chemical content of the solid electrolyte interphase (SEI) and its properties has not been demonstrated to far [114].

1.12 Literature Survey

Sreedhar et al. conducted a synthesis of few layered MoO$_3$/graphene materials, which demonstrated a reversible capacity of 934.4 mAhg^{-1}, accompanied by an initial columbic efficiency of 88% [65]. In a similar manner, Zhang et al. synthesized a

composite of MoO_3/RGO, which exhibited a current density of 208 mAg^{-1} after 50 cycles, as opposed to the initial current density of 50 mAg^{-1}. The observed performance of this particular event was ascribed to the existence of RGO, which effectively reduced the fluctuations in volume and facilitated electrical connectivity[115]. In a study conducted by LIBs, it was shown that the composite of MoO_3/graphene nanoribbons exhibited a capacity of 834 mAhg^{-1} at a current density of 200 mAg-1 after undergoing 70 cycles[116]. In their study, Ma et al investigated the performance of MoO_3/MWCNTs composites as anode materials for lithium-ion batteries (LIBs). The composites exhibited a specific capacity of 1041.1 mAhg^{-1} at a current density of 0.5 Ag^{-1}. Remarkably, the specific capacity improved to 1350 mAhg^{-1} after 300 cycles, as stated by the authors [117]. Wang et al. also discovered enhanced performance and improved cycling stability by the inclusion of multi-walled carbon nanotubes (MWCNTs). The performance of MoO_3 was improved by the use of single-walled carbon nanotubes (SWCNTs), resulting in a reversible capacity of 1357 mAhg^{-1}. Furthermore, only a minor capacity loss of 1.2% was observed after 100 cycles[118].

Feng ma et al. prepared MoO_3/multiwalled carbon nanotube (MWCNT) nanocomposite material by an innovative surfactant-assisted solvothermal technique, and then it was calcined at a low temperature. This composite material possesses not only a large capacity but also outstanding rate capability and cyclability in addition to its high capacity. For instance, the reversible charge capacity only drops from 1138.3 to 941.4 mAhg^{-1} when the discharge/charge current density is increased from 0.1 to 2 A g^{-1}. This results in a capacity retention rate of 82.7%. A reversible charge capacity of 490.2 mAh g^{-1} is still kept even after being cycled at a high current density of 20 A g^{-1}, displaying a capacity retention of 43.1%. This is the case even when the device is subjected to a high current density. The initial reversible charge capacity is 1041.1 mAh g^{-1} when it is repeatedly cycled at a current of 0.5 A g^{-1}; this is the capacity of the battery. When the battery has been through 292 cycles, it will have reached its maximum charge capacity of 1392.2 mAh g^{-1}. Even after being subjected to 300 cycles, the high charge capacity of 1350.3 mAh g^{-1} is preserved [117].

Chun Ling Lu prepared a-MoO_3/graphene (MoO_3/G) via in situ hydrothermal method. The composites were characterized via a range of techniques for characterization, such as powder X-ray diffraction, transmission electron microscopy, scanning electron microscopy, X-ray photoelectron spectroscopy, and an electrochemical performance

test. The findings indicate that the MoO₃/G composites demonstrate notable capacity and favorable cycle stability when employed as the anode for lithium-ion batteries. Out of all the samples examined, the MoO₃/G-27 sample demonstrates the most favorable electrochemical performance. It exhibits an initial charge capacity of 977.7 mAh g^{-1} when subjected to a current density of 50 mA g^{-1}, along with a first coulombic efficiency of 69.5%. After undergoing eighty cycles, the electrode demonstrates a sustained capacity of 869.2 milliampere-hours per gramme (mAh g^{-1}), indicating a high level of capacity retention at 88.9%. The excellent electrochemical performance of the composite anode is strongly influenced by its structure. Specifically, the MoO₃ nanobelts are uniformly attached to the surface and also embedded within the interlayer of the graphene sheets. This arrangement effectively prevents the volume change and aggregation of the MoO₃ nanobelts during the process of lithium-ion insertion and extraction. In contrast, it should be noted that graphene possesses electronic conductivity. The connection between graphene and MoO₃ nanobelts results in a significant electrode/electrolyte contacting area, as well as a short path length for the transportation of Li$^+$ during the process of lithium insertion and extraction[67].

Shahsank et al. prepared MoO₃ nanoparticles as anode materials for lithium-ion batteries (LIBs). This article presents a study on the synthesis of MoO₃ nanoparticles through a solution combustion method. The researchers utilized tamarind seed powder as a unique fuel source, which resulted in the production of excess carbon in situ. This carbon content eliminates the need for acetylene black as a conducting material during the electrode preparation for lithium-ion batteries (LIBs). The MoO₃ nanoparticles that were synthesised were subjected to various characterization techniques for comprehensive study. X-ray diffraction (XRD) was employed to determine the structural properties of the nanoparticles. Fourier-transform infrared spectroscopy (FTIR) was used to investigate the vibrational bonding present in the nanoparticles. CHN elemental analysis was conducted to determine the elemental composition of the nanoparticles. The pore size distribution and specific surface area. The MoO₃ nanoparticles exhibit remarkable electrochemical performance due to the inclusion of carbon content. This is seen by an initial discharge capacity of 1171 mAhg^{-1}, which stabilises at 162 mAhg^{-1} after 200 cycles. Additionally, the Columbic efficiency of these nanoparticles approaches 100% [68].

Reddeppa, Nadimicherla, et al synthesized flowerlike a-MoO₃ nanorods by one-step solvothermal process. This method did not require the use of any catalysts, surfactants,

or templates. Nanorods made of highly crystalline a-MoO_3 grow in the direction of [001] with lengths of up to 2mm and diameters ranging from 150 to 200 nm. X-ray diffraction, Raman spectroscopy, scanning electron microscopy, transmission electron microscopy, X-ray photoelectron spectroscopy, Fourier transform infrared spectroscopy, and electrochemical measurements as an anode material for lithium-ion batteries are used to characterize the nanorods after they have been prepared. The flower-shaped a-MoO_3 nanorod electrodes have been measured to have initial discharge capacities of 1182 mAh g^{-1} and initial charge capacities of 1158 mAh g^{-1}, respectively, with a Coulombic efficiency of 99.45%. In addition, because of their one-of-a-kind flowerlike architecture, they demonstrate excellent cyclability, endurance, and reliability, making them a promising anode alternative for lithium-ion batteries [69].

 Fu et al. employed a sol-gel method in conjunction with a glycine-based carbonization technique to synthesize chromium(III) oxide (Cr_2O_3) nanoparticles that were embedded into carbon sheets. The researchers conducted tests on Cr_2O_3/carbon nanocomposites as anode materials for lithium-ion batteries (LIBs). The results showed that these nanocomposites exhibited superior cycling and rate performances compared to pure Cr_2O_3. Specifically, after 150 cycles at a current density of 100 mAg^{-1}, the nanocomposites had a reversible capacity of 465.5 mAhg^{-1}. Additionally, at current densities of 200, 400, and 800 mAg^{-1}, the nanocomposites had discharge capacities of 448.7, 287.2, and 144.8 mAhg^{-1}, respectively. In contrast, pure Cr_2O_3 had a reversible capacity of 71.2 mA h g 1 after 150 cycles at a current density of 100 mAg^{-1}, and discharge capacities of 174.4, 60.5, 29.5, and 13.6 mAhg^{-1} at current densities of 100, 200, 400, and 800 mAg^{-1}, respectively. The improved performance of the nanocomposites can be attributed to the presence of carbon sheets, which effectively mitigate the volume change during lithiation/delithiation and enhance the electrical conductivity between Cr_2O_3 nanoparticles [119].

Mesoporous Cr_2O_3 with a high specific surface area of 162 m^2g^{-1} was synthesized by Zhiqin Cao et al, and it was created using the solution combustion process. The nanoparticles that make up the mesoporous Cr_2O_3 have an average particle size of 20 nm and are arranged in a sheet-like shape. Mesoporous Cr_2O_3 nanoparticles have improved electrochemical performance when used in rechargeable lithium-ion batteries as an anode electrode material. After 55 cycles, a capacity of 480 mAhg^{-1} that is both stable and reversible has been demonstrated. The increased electrochemical

performance of Cr_2O_3 can be due to the high surface area and geometrical properties of mesoporous materials [1].

Bai et al. observed that the cyclic stability of chromium (III) oxide (Cr_2O_3) is significantly compromised as a result of the substantial volumetric alterations that occur throughout the process of lithiation and delithiation. The present study demonstrates that the cyclic stability of Cr_2O_3 nanocrystals can be enhanced through the utilization of a straightforward hydrothermal synthesis process. The sample was calcined at a temperature of 430 °C exhibits characteristics of uniform size, a compact structure, and a high degree of crystallization. The Cr_2O_3 nanocrystals demonstrate a consistent cyclic performance of 185 mAh g^{-1} following 100 cycles at a current density of 100 mA g^{-1}. The practical applications of this technology extend to several real-world scenarios, including the provision of power consumption for small-scale devices, among other potential uses [120].

Jongmin Kim et al. presented a viable approach that can be universally employed to enhance the performance of lithium-ion batteries using anode materials composed of insulating metal oxides. Density-modulated multilayered homo-junction tungsten oxide (WO_x) films were synthesized as anode materials for lithium-ion batteries. The fabrication process involved the deposition of high- and low-density thin layers on copper current collectors using radio frequency magnetron sputtering. The optimization of the battery's performance was methodically conducted by varying the number of layers and the deposition order of the multilayered WO_x. The performance of a 4-layer density-modulated WO_x anode, characterized by a low density on the top WO_x layer, was found to be superior. It exhibited a high reversible capacity of 508 mAh g^{-1} after 200 cycles, when subjected to a current density of 0.2 Ag^{-1}. In addition, the tested material exhibited a reversible capacity of 150 milliampere-hours per gramme and a favorable coulombic efficiency of 93.7% following 1000 cycles under a high current density of 2 amperes per gramme. Furthermore, it demonstrated exceptional rate capability and cycling stability. The exceptional battery performance exhibited by the density-modulated multilayer WO_x anode can be ascribed to its regulated mass loading, enhanced charge-transfer kinetics, and advantageous shape[121].

Sul Ki Park et al. reported the production of tungsten trioxide (WO_3) particles that are coated onto three-dimensional (3D) macroporous frameworks of reduced graphene oxide (RGO). These structures are intended for use as anodes in lithium-ion batteries.

The deposition of WO_3 particles on the surface of reduced graphene oxide (RGO) sheets leads to the formation of hierarchically structured, three-dimensional (3D) networks in the ensuing RGO/WO_3 frameworks. These networks are constructed by a hydrothermal process. The RGO/WO_3 hybrid frameworks, which possess a hierarchical architecture, demonstrate a discharge capacity of 487 mAhg^{-1} even after undergoing 100 cycles at a current density of 150 mAg^{-1}. Additionally, these frameworks exhibit a reversible capacity of 356 mAhg^{-1} when subjected to a high current density of 300 mAg^{-1}. Such the improved battery performances of RGO/WO_3 frameworks are attributed to uniform dispersion of discrete WO_3 particles and 3D macroporous continuity, which provides a high accessible area, easy accessibility to redox sites, short ion diffusion length, and rapid charge and mass transport[122].

1.13 Aims and Objectives

Based on the literature studied, it is need of hour to develop energy storage devices, because we are living in a world that is powered by technology and their smooth running require energy, which lead to greater energy demands. Fossil fuels which are main sources of providing energy are suffering from the problem of being depleting with time along emitting GHG, therefore focus has been made to shift energy production to green technologies such as solar and wind power, but the difficulty is their smooth integration into grids and storage off -peak periods which require batteries. Apart from that, batteries are also required for powering electric vehicles and consumer electronics. Lithium-ion batteries are the first choice to satisfy these demands.

- This work also aims to synthesize transition metal oxides based anode materials for LIBs to address the problems encountered and will be based on the following aims and objectives.

- To develop the composites of TMO with carbon nanomaterials/reduced graphene oxides and to apply suitable conducing polymer

- To increase the specific capacity of anode materials to enable high energy storage.

- To improve the cyclic stability of anode material to extend lifespan of battery

- To study the electrochemical properties of anode materials to understand its feasibility and limitations

- To study the electrochemical properties of anode materials to understand its

43

feasibility and limitations

2. EXPERIMENTAL

This chapter explain the methodologies used during the synthesis of TMOs. Furthermore, their hybrid composites with various carbon materials, including (CNTs and Graphene etc.) was also prepared. After the development of various hybrid nanostructured materials, coin cell fabrication was done to study the cycling properties of prepared anode materials, which will be discussed in next chapter.

Furthermore, detailed description about characterization techniques includes in the later portion of the chapter.

2.1 Methodology

The nanostructured materials based on transition metal oxides were synthesized using co-precipitation method. The advantage of using such techniques is that the morphology, crystal structure and dimensionality of the nanostructures can be controlled by the experimental conditions. Compared to some complex methods, coprecipitation is simpler and more cost-effective. It often requires fewer steps, basic equipment, and fewer reagents, making it more accessible for smaller-scale laboratories or industrial settings. Coprecipitation enables the simultaneous precipitation of multiple ions or compounds, resulting in homogeneous materials with controlled compositions. The procedures of coprecipitation are among of the simplest processes; they have the lowest costs and the least amount of energy usage.

The size and shape of the nanoparticles are greatly impacted by a variety of parameters, including the pH of the solution, the concentration of the starting chemicals, and the effect of heating the solution. In this technique, the solvent is used to dissolve the raw ingredients (chloride or nitrate) in order to obtain a solution that is homogeneous. After that, a base, such as sodium hydroxide or ammonium hydroxide, is added to the hydroxide solution, which causes the precipitates to develop. The formation of metal oxide nanoparticles is achieved through the use of a heating treatment following the washing of the appropriate salts as shown in the scheme below in Fig 2.1.
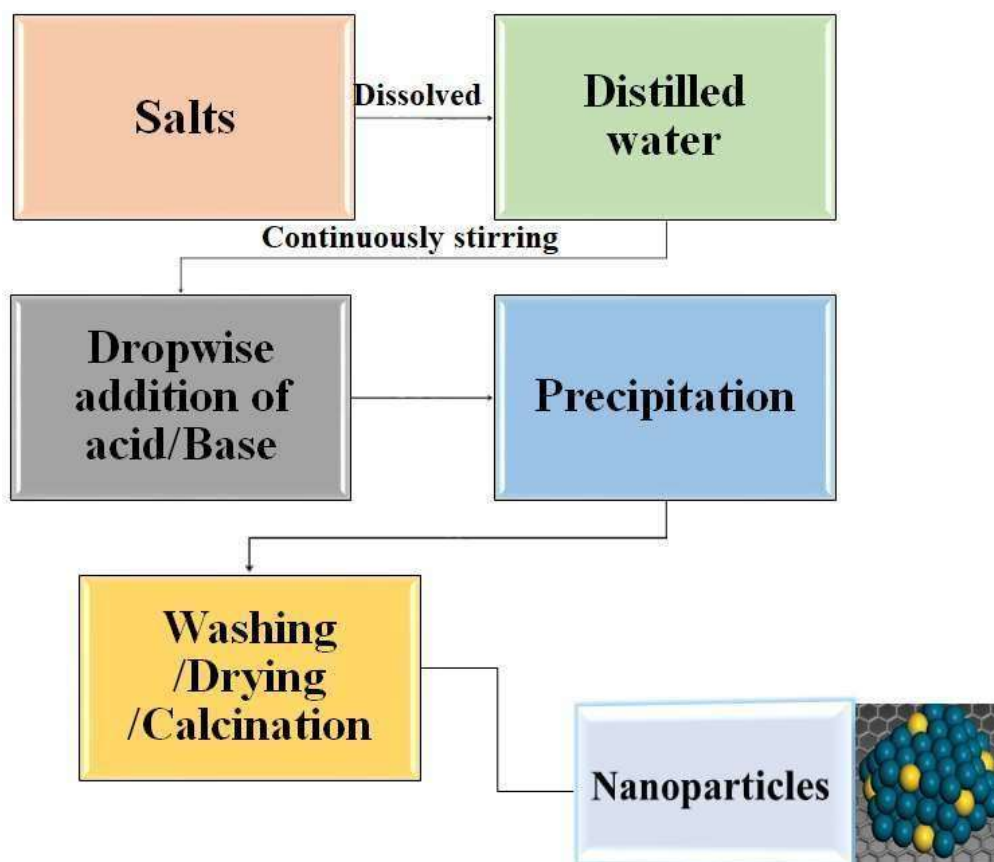
Figure 2.1 Schematic diagram of co-precipitation method.

2.1.1 Synthesis of chromium oxide Cr₂O₃ and its hybrid composites

In this work, Cr_2O_3 is active material, which is synthesized by coprecipitation method. Carbon nanomaterials (CNTs and RGO) were added to increase the conductivity of active material. Furthermore, coating of polyaniline was done to mitigate volume changes. Further details about the synthesis and properties of these materials are given in the coming section.

Analytical grade chemicals were used without any further purification. The detail of all the chemicals used are the followings: ($CrCl_3.6H_2O$, Sigma Aldrich, 98-100%), Ammonium hydroxide (NH_4OH), Aniline and ammonium per sulfate ($NH_4S_2O_8$). Cr_2O_3 nanocomposites with functionalized MWCNTs (Nanocyl® diameter < 10 nm, length 1-2 μm) and PANI were synthesized by co-precipitation method. Briefly, a calculated amount of 0.1 M $CrCl_3.6H_2O$ solution was made in 200 ml deionized water and stirred for 30 min to obtain a homogeneous mixture, then in a separate beaker

0.08 g of functionalized MWCNTs were added in 20 ml of deionized water and ultrasonicated for 1h for better dispersal of MWCNTs. Then it was added subsequently in $CrCl_3.6H_2O$ solution and 13 ml aqueous ammonia (NH_4OH) was dropwise added to the mixture under 30 min magnetic stirring to mineralize metal salt on the surface of MWCNTs until pH=11 is reached. The green color precipitates of $Cr(OH)_3$ thus formed were filtered, centrifuged, and washed many times with deionized water to remove impurities. Precipitates were dried at 50 °C in the oven overnight and calcined at 550 °C for 5 h in a furnace to get Cr_2O_3-MWCNT$_{(x\%)}$ nanocomposite [x= 0.08g (4%), 0.17g (8%), 0.26g (12%)]. The same procedure was implemented without adding MWCNTs and bare Cr_2O_3 nanoparticles were obtained.
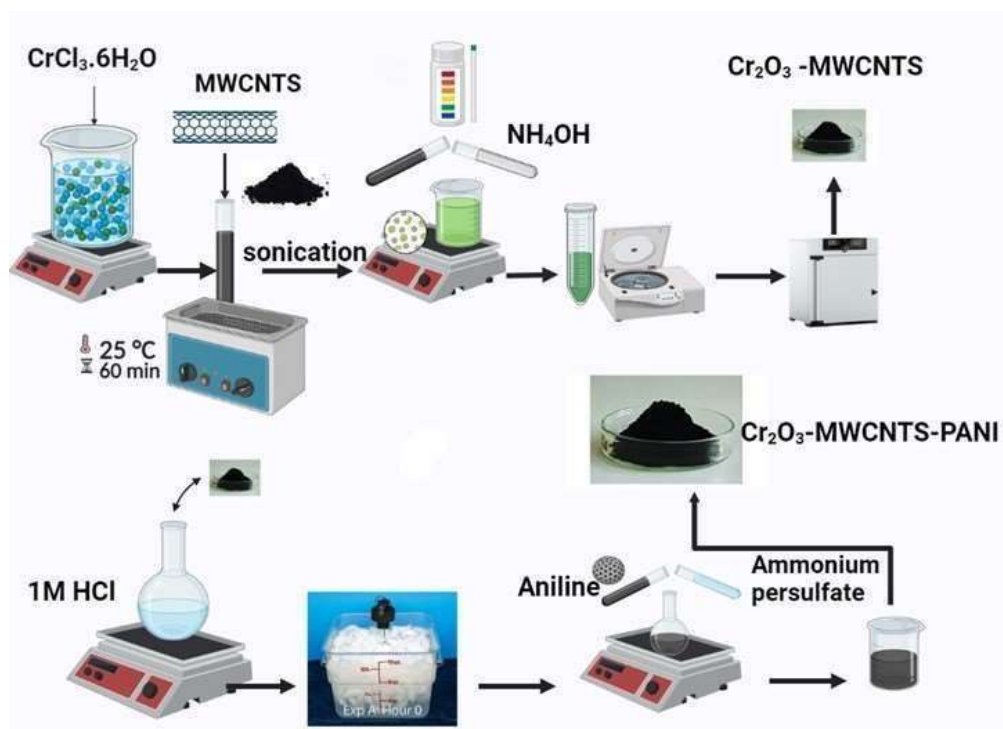
Figure 2.2 Schematic illustration of Cr_2O_3-MWCNTs$_{(x\%)}$ and Cr_2O_3-MWCNTs$_{(x\%)}$-PANI nanocomposites.

For PANI coated samples appropriate amount of synthesized material was dispersed in 1 M HCl solution in a round bottom flask by means of ultrasonication for 30 min. This was then placed in an ice bath and temperature was maintained below 4°C during whole reaction time. After stirring for 10 min, an appropriate amount of aniline monomer in order to get 10 wt. % coating over synthesized material, was added in to round bottom flask followed by stirring for 30 min. Ammonium per sulfate which acts as an oxidizing agent and initiator for the polymerization of aniline was dissolved in

a separate beaker in distilled water and was then slowly poured into round bottom flask. The reaction mixture was then stirred for 6 h followed by washing and drying of PANI coated nanoparticles as schematically represented in Fig 2.2.

Table 2.1 List of chromium-based samples

Sr. No	Samples	Composition
1	Cr_2O_3 -pure	Cr_2O_3
2	Cr_2O_3-(MWCNTS)$_{4\%}$	Cr_2O_3+4wt%CNT
3	Cr_2O_3-(MWCNTS)$_{8\%}$	Cr_2O_3+8wt%CNT
4	Cr_2O_3-(MWCNTS)$_{12\%}$	Cr_2O_3+12wt%CNT
5	Cr_2O_3-(MWCNTS)$_{4\%}$-PANI	Cr_2O_3+4wt%CNT+PANI
6	Cr_2O_3-(MWCNTS)$_{8\%}$-PANI	Cr_2O_3+8wt%CNT+PANI
7	Cr_2O_3-(MWCNTS)$_{12\%}$-PANI	Cr_2O_3+12wt%CNT+PANI
8	Cr_2O_3-PANI	Cr_2O_3-PANI
9	Cr_2O_3-(RGO)$_{12\%}$-PANI	Cr_2O_3+12wt%RGO+PANI

2.1.2 Synthesis of molybdenum oxide and its hybrid composites

To date, MoO_3 is used as a promising anode material for Li ion batteries (LIBs) owing to versatile structure, low cost, nontoxicity, natural abundance, adjustable chemical state, high thermal and chemical stability[123] , environmental friendliness and a good theoretical capacity of 1117 mAh/g [123], which is three times greater than that of commercial graphite (327 mAh/g) [124]. On the basis of crystallographic arrangement, MoO_3 has three different polymorphs, h-MoO_3 (hexagonal), metastable[88] β- MoO_3 (monoclinic) and α-MoO_3 (orthorhombic) ,of which α-MoO_3 is the most stable thermodynamically . Moreover, MoO_6 is a building block of MoO_3, and MoO_6 octahedron in the layered structure of MoO_3 provides a diffusion path for Li ions[125]. However, α-MoO_3 exhibits poor electronic and ionic conductivity and suffers from large volume changes that induce pulverization during delithiation/lithiation, unstable crystal structure, small surface area , resulting low specific capacity and poor

cycling stability[126, 127 91 128]. We successfully obtained the alpha -MoO_3 phase by incorporating carbon nanotubes (CNTs) in ratios of (4%, 8%, 12%). Additionally, we applied a PANI coating.

Analytical grade chemicals were used without any further purification. The detail of all the chemicals used are the followings: Ammonium Molybdate Tetrahydrate $(NH_4)_6MO_7O_{24}.4H_2O)$, Nitric acid ($HNO_3$), aniline and ammonium per sulfate $(NH_4S_2O_8)$.
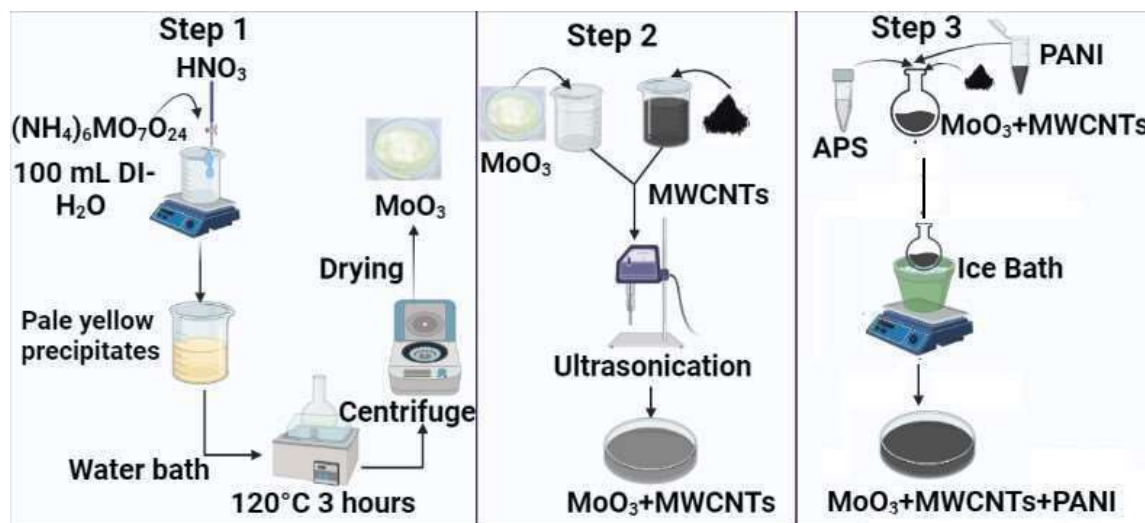
Figure 2.3 Schematic illustration of MoO_3-MWCNTs$_{(x\%)}$ and MoO_3-MWCNTs$_{(x\%)}$-PANI nanocomposites

MoO_3 nanorods were synthesized by adding 0.1 M solution of ammonium heptamolybdate tetrahydrate in 100ml deionized water and solution was stirred continuously for 30 minutes. Subsequently, 5ml concentrated Nitric acid (HNO_3) was poured slowly drop-wise. Pale –yellow-colored precipitates were observed in a reaction beaker. The beaker was then placed in water bath at 120 °C for 3 hours. The obtained precipitates were washed, centrifuged and dried for 6 hours in oven at 70 °C.

2.1.3 Synthesis of α-MoO₃-MWCNTs-PANI

Accordingly, for the preparation of MoO_3/MWCNTs (x=4%(0.15g), x=8%(0.312g) ,x=12%(0.48g) of functionalized MWCNT$_S$ were ultra-sonicated for 30 minutes in 50 ml water(solution A). 3.62g of prepared MoO_3 was also ultrasonicated for 30 minutes in 25 ml water. 25 ml of solution B was transferred to 50 ml of solution A and mixture was ultra-sonicated for one hour. Excess water was removed using a centrifuge and

remaining was dried in oven at 50°C. For preparation of MoO₃/MWCNTs/PANI appropriate amount of prepared material was added in a round bottom flask containing 1M HCl solution and ultrasonicated for half hour as shown in Fig 2.3. The solution was then placed in an ice bath so that during whole reaction time temperature could be maintained. After 10 minutes stirring 10 wt% of aniline monomer was added in a round bottom flask followed by 30 minutes stirring. A calculated amount of ammonium per sulfate (APS) was added in small amount of distilled water and poured slowly in a round bottom flask. APS act as an oxidizing agent that mainly initiate polymerization of aniline monomer. The reaction mixture was stirred in ice bath for 6 hours and temperature was maintained below 4°C. After 6 hours the mixture was washed many times and dried.

Table 2.2 List of molybdenum-based samples

Sr. No	Samples	Composition
1	MoO_3-pure	MoO_3
2	MoO_3-$(MWCNTS)_{4\%}$	MoO_3+4wt%CNT
3	MoO_3-$(MWCNTS)_{8\%}$	MoO_3+8wt%CNT
4	MoO_3-$(MWCNTS)_{12\%}$	MoO_3+12wt%CNT
5	MoO_3-PANI	MoO_3-PANI
6	MoO_3-$(MWCNTS)_{4\%}$-PANI	MoO_3+4wt%CNT+PANI
7	MoO_3-$(MWCNTS)_{8\%}$-PANI	MoO_3+8wt%CNT+PANI
8	MoO_3-$(MWCNTS)_{12\%}$-PANI	MoO_3+12wt%CNT+PANI
9	MoO_3-$(RGO)_{12\%}$-PANI	MoO_3+12wt%+RGO+PANI

2.1.4 Synthesis of tungsten oxides (WO₃) and its hybrid composites

WO₃ has various polymorphs. The monoclinic structure of WO₃ has gained interest for its potential application as anode materials in LIBs because of its favorable crystal structure and the suitable oxidation state of tungsten. Despite its limited electrical conductivity and slow the kinetics of lithium intercalation and de-intercalation, as well

as the large volume changes and repetitive cycles, which cause expansion or contraction, leading to a decreased capacity. So Monoclinic phase was prepared and its composites were prepared with CNTs and RGO, furthermore PANI coating was also done.
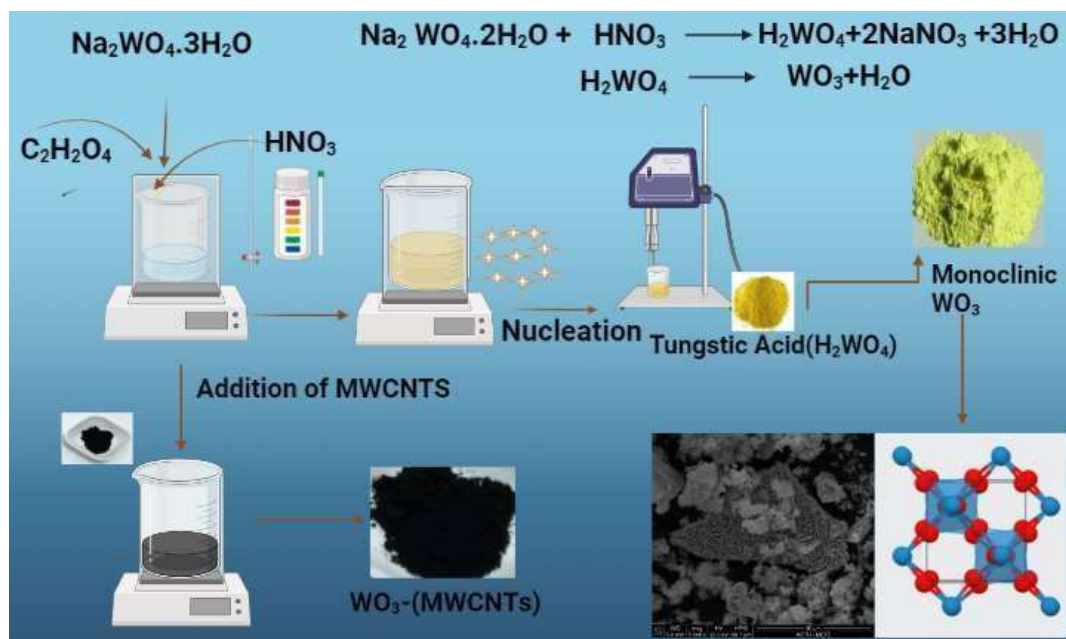
Figure 2.4 Schematic illustration of WO_3-$MWCNT_S$ nanocomposites.

Analytical grade chemicals were used without any further purification. The detail of all the chemicals used are the followings sodium tungstate di-hydrate**,** Nitric acid (HNO_3), Aniline and ammonium per sulfate ($NH_4S_2O_8$).

1.0 Molar sodium tungstate di-hydrate ($Na_2WO_4.2H_2O$) and 0.1 molar oxalic acid ($C_2H_2O_4$) were dissolved in 100 ml of deionized water. The oxalic acid acts as a chelating agent, then in a separate beaker functionalized 0.2g MWCNTs were added in 20 ml of deionized water and ultrasonicated for 1 h for better dispersal. Then it was added in to above solution and HNO_3 was added to change pH from 5 to 1. The solution was then stirred for few hours to obtain the yellow color of solution, which indicate formation of tungstic acid (H_2WO_4). The solution was ultrasonicated for 30 min and dried for whole day. The resulting yellow precipitates were filtered, dried, washed with ethanol to remove the extra impurities.

For preparation of PANI coated samples, some amount of prepared material was dispersed in 1 M HCl solution in a round bottom flask followed by ultrasonication for 30 min. The temperature of mixture solution was maintained below 4 °C in an ice bath during whole reaction and stirred for 10 minutes. After that 10 wt. % aniline monomer

was added over mixture solution and stirred for 30 minutes. The oxidizing agent ammonium per sulfate (APS) was slowly poured to the solution, which act as initiator for polymerization of aniline. The solution mixture was then stirred for 6 h followed by washing and drying of PANI coated nanoparticles. Fig 2.4 provides a schematic description of the synthesis strategy of the hierarchical WO_3.

Table 2.3 List of Tungsten based samples

Sr. No	Samples	Composition
1	WO_3-pure	Pure WO_3
2	WO_3-$(MWCNTS)_{4\%}$	WO_3 + 4wt% CNT
3	WO_3-$(MWCNTS)_{8\%}$	WO_3+8wt%CNT
4	WO_3-$(MWCNTS)_{12\%}$	WO_3+4wt%CNT
5	WO_3-PANI	WO_3-PANI
6	WO_3-$(MWCNTS)_{4\%}$-PANI	WO_3+4wt%CNT+PANI
7	WO_3-$(MWCNTS)_{8\%}$-PANI	WO_3+8wt%CNT+PANI
8	WO_3-$(MWCNTS)_{12\%}$-PANI	WO_3+12wt%CNT+PANI
9	WO_3-$(RGO)_{12\%}$-PANI	WO_3+12wt%RGO+PANI

2.2 Physicochemical Characterizations

The as prepared samples were first characterized to study their physicochemical properties. Initially, the samples were characterized by X-ray diffractometer (XRD, Bruker D8) for structural analysis. Field emission scanning electron microscopy (FESEM Sigma 500 VP) was used to get information regarding morphology and size distribution at nanoscale. BET (Brunauer-Emmett-Teller) and BJH (Barrett-Joyner-Halenda) were recorded from nitrogen adsorption desorption isotherms to calculate active surface area and pore size distribution. Thermogravimetric analysis (TGA) (Schimadzu DTG-60) was done to measure weight changes in a material as a function of temperature. Fourier transform-infrared (FTIR) analysis was performed using

(JASCU 6600) spectrometer in a transmittance mode in the range of 500 to 4000 cm⁻¹ to investigate different functional groups. Diffuse reflectance spectroscopy (DRS) (Perken Elmer lambda 950) was used to obtain information regarding band gap and conductive nature of synthesized materials. The chemical binding and surface composition of the materials were evaluated by X-ray photoelectron spectroscopy (XPS) (Seienta Omicron).

2.2.1 X-ray Diffraction (XRD)

It is non – destructive, most frequently and extensively employed technique to get information about srystal structure, lattice parameters , crystallite size, inter planar distance , strain and growth orientation etc. The powder diffraction data of nearly 150,000 organics, inorganic organometallic, and mineral samples has been assembled in single database named as joint Committee on powder diffraction standards (JCPDS). In crystalline solids, powder patterns aare determined by two distinguished features,(i) size and shape of the crystal, (ii) atomic number and position of specific atoms in a unit cell. For that reason, two materials with same structure possess different X-ray diffraction pattern, which act as finger print for identification.

2.2.1.1 Basic principle of XRD

It is based on the constructive interference of monochromatic X-rays and crystalline sample, when condition satisfy Bragg's law. Bragg's law correlates the wavelength of electromagnetic radiations with inter-planar distance, and diffraction angle of crystalline sample.

$$n\lambda = 2d\sin\theta$$

Where, n=an integer, λ = wavelength of X-rays, d= inter -planar distance between atomic layers in the unit cell, and θ = diffraction angle.

The crystallite size was calculated by Bebye-Scherrer equation which is given as

$$D = \frac{K\lambda}{\beta\cos\theta}$$

Where K= shape factor= 0.89 , λ = wavelength of X-rays, β = line broading at full width half maxima in radian, and θ = diffraction angel .Lattice parameters were calculated using formula given below.

$$\frac{1}{d2} = \frac{h2 + K2}{a2} + \frac{l2}{c2}$$

Where d= interplanar disctance between atomic layers in the unit cell, "a" and "c" are lattice parameters and h ,k and l are miller indices.

XRD (Phillips PW 304/60 Xpert pro) powder Diffractometer with Cu Kα radiation (λ= 0.154 nm)[129]. X-ray diffractometer consist of three basic elements, an X-ray tube, a sample holder, and an X-ray detector as shown in Fig 2.5. Electron beam is produced by heating filament, which is then accelerated and bombarded on target material. As a result, X-rays are generated in Cathode ray tube are collimated and directed to the sample. The samples is rotated in the path of collimated X-ray at angle (θ) while detector is mounted on an arm to record diffracted ray at angle (2θ). An intense peak of constructive interference occurs when the geometry of incident ray impinging the sample satisfied Bragg's equation. A detector then records the signal and convert into count rate. A goniometer used to rotate sample and maintain angle[130].
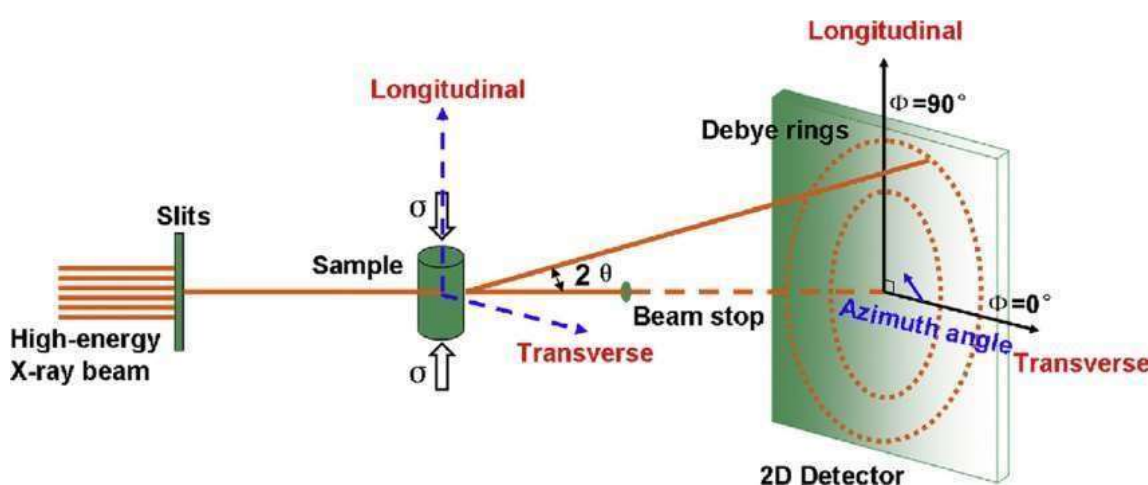
Figure 2.5 : Schematic illustration of X-ray diffractometer

2.2.2 Fourier Transform Infrared (FTIR) spectroscopy

It is used for determination of quantitative and qualitative features of materials, which are IR active molecules and commonly employed for measuring infrared spectrum of absorption or emission of a solid, liquid and gas. It is fast and economical technique also work for films and crystalline or amorphous solids. The basic principle of vibrational spectroscopy involve change in dipole moment through interaction between frequency of electric field of electromagnetic radiations of Range 700nm - 1mm and vibrational frequency of bond. When IR radiations interact with matter some of the radiations get absorbed, while others are transmitted. Only those radiations get absorbed whose frequency matches with vibrational frequency of bond. The

vibrational frequency is affected by strength and masses of bonded atoms. Those vibrations which bring dipole change either perpendicular or parallel to bond axis are IR active. The simple types of IR active vibrational mods which give rise to absorption modes are IR active too. Vibrations are also named as symmetric and asymmetric depending on how they change the symmetry of molecules. The two of the same type of bond in different molecules possess slightly different environments , which means each bond in a molecule have different characteristic frequency[131].

2.2.3 Scanning Electron Microscopy (SEM)

Scanning Electron Microscopy is also utilized to investigate the material's properties. To generate a picture, a focused beam of electrons on the surface of the object is utilized in scanning electron microscopy. Schematic diagram of SEM is shown in Fig 2.6.
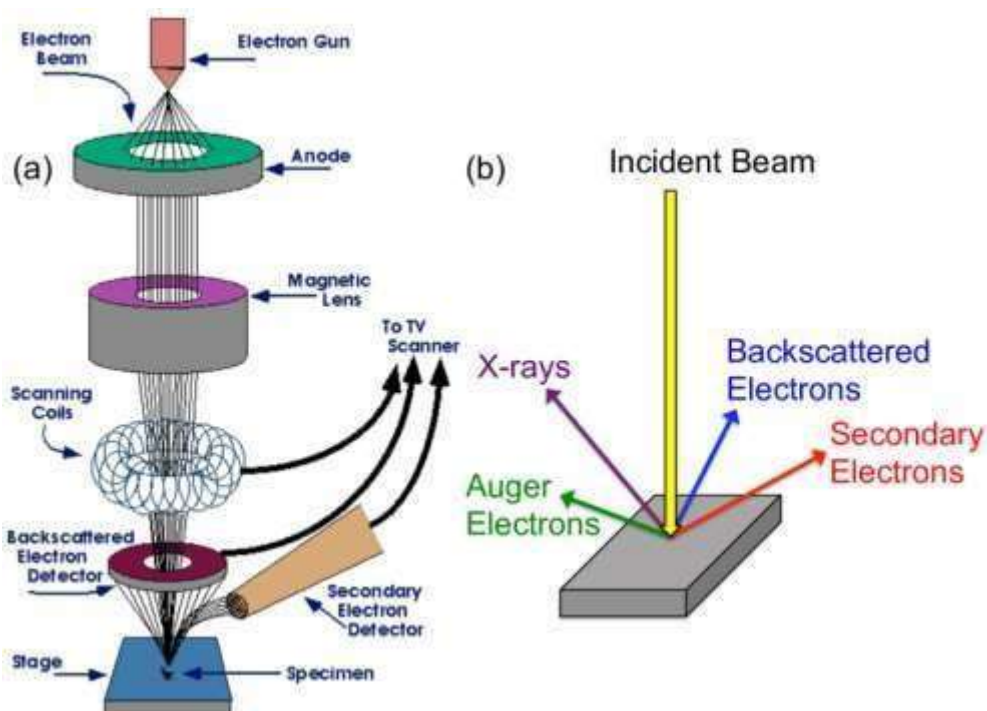
Figure 2.6 Schematic diagram of SEM

Whenever electrons collide with the material surface, they emit a variety of signals that aid in obtaining information about the surface topography. When the wavelength became the limiting element in light microscopes, the SEM was created. It has a higher resolution because of the considerably shorter wavelength. The electron gun, which is situated at the top, fires a tremendous electron beam. There are two types of electron

guns: one that generates a high electric field and the other that heats the filament till the electrons flow away.

When an electron beam collides with a material, it releases three types of electrons: primary or back scattered electrons, auger electrons, and secondary electrons. For image information, scanning electron microscopy (SEM) employs all three kinds of electrons. SEM comprises of an electron source (electron gun), an anode that invent the electron beam, a magnetic lens (which is used for electron beam condensation), and a focusing lens that is used to concentrate the electron beam directly on the target.

There are several detectors present, which are employed to detect all varieties of electrons. Several electrons are detected by the secondary electron detector, while others are identified by the backscattered electron detector. SEM doesn't really reveal the color of the material; rather, it reveals its shape and surface. SEM (Sigma 500 VP) is shown in Fig 2.6.

2.2.4 Energy Dispersive X-Ray Spectroscopy (EDX)

Energy dispersive X-ray spectroscopy was carried out in order to assess the elemental composition and characterizing purity of synthesized samples.

2.2.5 Thermal Gravimetric Analysis (TGA)

Thermal Gravimetric analysis measures weight changes in a material as a function of temperature, which i raised in controlled manner under a particular atmosphere. It gives information about the physical phenomena such as adsorption, absorption, sublimation and vaporization. TGA is used to access the weight content of various fillers and polymers coating used in synthesizing composites. TGA analysis was performed on Mettler -Toledo Thermogravimetric Analyzer TGA/DSC-1 from room temperature to 900°C at a heating rate of 10°C /min under air atmosphere.

2.2.6 Diffuse Reflectance Spectroscopy (DRS)

The electronic absorption spectrum measurements is necessary for the investigation of optical features of nanomaterials. Diffuse Reflectance Spectroscopy is an analytical technique, which is used to obtain information regarding band gap and conducive nature of synthesized materials. The high sensitivity of optical properties of nanomaterials towards shape, dimensions, quantity, state of accumulation and refractive index makes these spectroscopic techniques useful for examining these

materials. The DRS spectrum for various was recorded using UV-VIS-NIR (lambda 950) PerkinElmer spectrophotometer in wavelength range of 380-800nm.

2.2.7 N$_2$ adsorption–desorption isotherms (BET and BJH methods)

The technique of gas adsorption holds significant importance in the characterization of porous materials. The BET approach, as proposed by reference[132] , utilizes the adsorption of nitrogen (N$_2$) in its liquid phase at a temperature of 77 K. During this process, the gas is adsorbed onto the particles of the adsorbent material using physical forces. The adsorption of N$_2$ at various pressure intervals results in a modification of the detected output composition. Upon the application of heat, the nitrogen molecules undergo desorption from the sample. Subsequently, it becomes feasible to quantify the surface area of the adsorbent and determine the distribution of pore sizes without causing any damage to the sample[133] as evidenced by the observation of peak regions that correspond to the desorbed mass.

The phenomenon of gas adsorption at elevated pressures can lead to the formation of several layers of adsorbed molecules. An illustration of this phenomenon is non-polar molecules that become adsorbed onto the surface of an adsorbent material. This adsorption process leads to the creation of dipoles within the initial layer of molecules, subsequently inducing the formation of dipoles in the subsequent layers, and so forth. Nevertheless, the adsorption originating from the subsequent layer is virtually negligible. Hence, the vertical interaction between molecules has been observed [132].

According to the BET hypothesis, adsorption takes place on a surface that is completely uniform, and each site possesses the same amount of adsorption energy. Adsorption happens on the exterior surface of the adsorbent particle and on the micropores, which are more energetic places, when the pressure is low (p/p^0 0.0–0.2). The creation of the second and third adsorption layers takes place when the pressure (p/p^0 0.4–0.95) increases. Condensation takes place in the mesopores (p/p^0 > 0.95) and in the macropores (p/p^0 > 0.95). As the pressure rises, there is a greater chance that another molecule may become attached to one that is currently occupied by another molecule. Because of this, the construction of the second layer begins prior to the completion of the formation of the first layer[134].

2.2.8 X-ray photoelectron spectroscopy (XPS)

In X-ray photoelectron spectroscopy (XPS), the specimen is exposed to mild X-rays with energies below approximately 6 keV, and the resulting released electrons' kinetic energy is examined. The photoelectron that is emitted is a consequence of the total transfer of energy from an x-ray to an electron in a core level. The statement asserts that the energy of an x-ray, denoted as hvv, can be expressed as the sum of the binding energy (BE) of the electron, which signifies the strength of its attachment to the atom or orbital, the kinetic energy (KE) of the emitted electron, and the work function (Φspec) of the spectrometer.
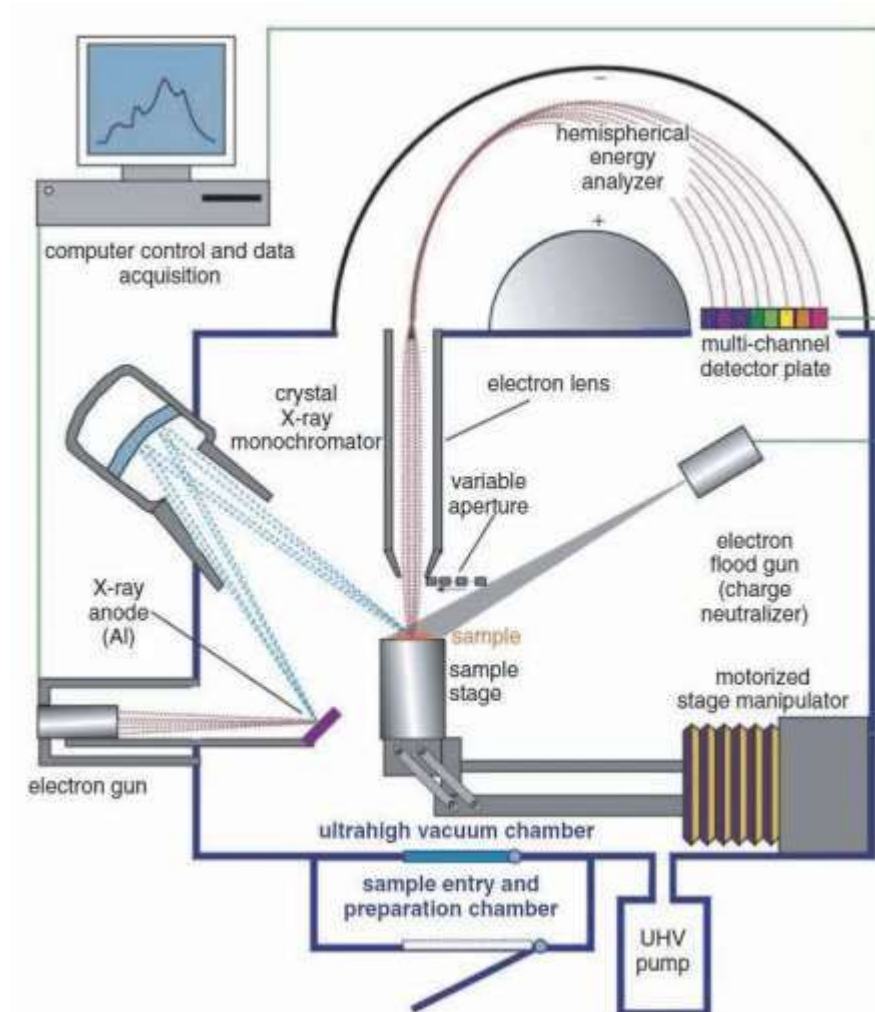
Figure 2.7 Schematic diagram of X-ray photoelectron spectroscopy (XPS)

This equation is represented as $h\nu = BE + KE + \Phi$spec, where $h\nu$ represents the energy of the x-ray. In this study, we aim to investigate the effects of climate change on biodiversity in tropical rain in order to calculate the binding energy of an electron, one can use Equation (1) to derive Equation (2), wherein the variables on the right-hand

side are either established (hν and Φspec) or obtained through measurement in the XPS experiment (KE). Thus, the equation can be expressed as BE = hν - KE + Φspec. The diagrammatic representation of this topic is also illustrated in Fig 2.7. It should be noted that the measurement of photoelectron binding energy is conducted relative to the Fermi level of the sample, rather than the vacuum level. This is the rationale behind the inclusion of Φspec.

The identification of photoelectron peaks is denoted by specifying the corresponding element and orbital from which they were emitted. As an illustration, the term "O1s" denotes electrons that are discharged from the 1s orbital of an oxygen atom. In order to effectively utilize the X-ray photoelectron spectroscopy (XPS) technique, it is necessary to focus on the emission and observation of electrons from the sample that possess a binding energy lower than the energy of the X-ray source. When doing studies using various x-ray sources, it is shown that the binding energy of photoelectrons remains constant. [135-138].

2.2.9 Coin cell fabrication

The galvanostatic charge discharge measurements were done using coin cells in which working electrode was prepared by making slurry of active material, PVDF (polyvinylidene fluoride) binder and carbon black in a weight ratio of 75:15:10 in NMP (N-methylpyrrolidinone) solvent. After mixing, slurry was coated on Cu-foil and 18 mm cut disks were dried at 120 °C. The assembling process of coin cells were completed in the glovebox using Li-foil as a counter electrode and glass microfiber paper separator. Galvanostatic cycling was performed using Biologic MPG-2 instrument at a current rate of 50, 100, 200 and 400 mA g^{-1}. The cyclic voltammetry was conducted in 0.01-3.0 V potential window at a scan rate of 0.5 mV s^{-1}. All experiments were done at 25 °C.

Figure 2.8 Schematic representation of coin cell fabrication

2.3 Electrochemical Characterization

The technique used to assess the suitability of the synthesized material as anode for LIBS was galvanostatic charge and discharge. Galvanostatic measurements give qualitative information regarding the process, rate capability and cyclic stability of the anode material.

2.3.1 Galvanostatic Charge Discharge (GCD) measurements

Galvanostatic measurements were done at a current density of 50 mAg^{-1}, 100 mAg^{-1}, 200mAg^{-1}, 400mAg^{-1} between a voltage range of 0.01 -3.0V vs Li/Li$^+$. Data was recorded for 35 cycles in order to evaluate the stability of the materials using biologic MPG2 instrument.

During the process of galvanostatic cycling, the charge and discharge current of batteries are frequently expressed as a C-rate. This C-rate is determined based on the nominal capacity of the battery, which is the capacity value that the battery possesses when it is fully charged. The C-rate is a measurement that determines the pace at which a battery is entirely charged or drained in comparison to its nominal capacity. For instance, a C-rate of 1C indicates that the amount of current required to completely charge or discharge the battery in one hour is applied. Additionally, C-rate multiples of 1C are utilized. It is typical practice in the field of battery research to utilize a C-rate of 0.1C in order to charge and discharge a battery in a period of ten hours. The amount of current, denoted by the symbol i (A), that is required to charge or discharge a battery is determined by multiplying the C-rate by the ratio of the nominal capacity of the battery, denoted by $Cmax$ (Ah), to the time, denoted by the symbol h.

2.3.2 Cyclic voltammetry (CV)

The cyclic voltammetry was conducted in 0.01–3.0 V potential window at a scan rate of 0.5 mV s^{-1}. All experiments were done at 25 °C. A cyclic voltammogram can be created by applying a linear potential sweep to the working electrode. A linear potential sweep is a potential that increases or drops linearly with time. Because of the oxidation or reduction of an analyte, current flows through the electrode whenever potential is applied below or above the formal potential, E°, of an analyte. This occurs as a result of the potential being applied. Because the amount of this current is proportional to the concentration of the analyte in solution, cyclic voltammetry can be utilized in the process of analytically determining the concentration of the analyte. In the context of process cyclic voltammetry, the instrumentation consists of a three-electrode assembly that includes a working electrode, a reference electrode, and an auxiliary electrode that is submerged in a calibration solution. In addition to applying and maintaining the voltage between the working electrode and the reference electrode, the potentiostat also measures the current that flows through the working electrode as a result of the flow of charge between the auxiliary electrode and the working electrode on the working electrode. The resulting cyclic voltammogram, which is a plot of current versus potential, can be recorded using either a plotter or a computer. Each of these devices functions as a recording device.

2.3.3 Electrochemical impedance spectroscopy (EIS)

EIS (electrochemical impedance spectroscopy) was performed at room temperature between the frequency range of 100 kHz and 10 MHz and an amplitude of 10 mV.

EIS is based on the premise of applying a small amplitude alternating current (AC) signal across a system or device across a variety of frequencies and then analyzing the voltage response that is produced as a result of this application. An alternating current (AC) signal with a known amplitude, which is often quite low, is applied to the electrochemical system within a frequency range that typically ranges from millihertz to megahertz respectively. At each frequency, the response of the system to this alternating current signal is measured in terms of the voltage changes that occur in relation to the current that is being applied. By regularly altering the frequency of the alternating current (AC) signal, it is possible to observe how the impedance of the system shifts in response to variations in frequency. Both a Nyquist plot and a Bode plot are typically used to plot the impedance data that is obtained as a result.

3. RESULTS AND DISCUSSIONS

This chapter comprises the explanation about the structural analysis of transition metal oxides-based nanocomposites, which were synthesized by co-precipitation method. and evaluate their performance as anode materials for rechargeable lithium-ion batteries.

All nanomaterials were characterized by XRD, SEM, FTIR ,DRS , TGA , BET ,CV, EIS and GCPL to study physical and chemical properties.

3.1 Chromium Oxides as anode materials for LIBs

As an anode material for lithium-ion batteries (LIBs), chromium (III) oxide (Cr_2O_3) has been reported to have a theoretical capacity of 1058 milliampere-hours per meter as well as a comparatively low EMF value of 1.085 volts. A mechanism that is comparable to that of other transition metal oxides is followed by Cr_2O_3, which is as follows: $6Li^+ + Cr_2O_3 + 6e \rightarrow 3Li_2O + 2Cr$. However, just like other pure metal oxide anodes, Cr_2O_3 has a number of obstacles or disadvantages. These includes fast capacity fading and low-rate performance as a result of its extreme volume expansion and contraction, as well as severe structural degradation during discharge and charge processes[119].

3.2 Physiochemical Characterizations

The crystal structure of the sample was investigated by XRD (X-ray diffraction) with Cu kα radiation ($\lambda = 0.154$ nm) recorded by Bruker D8 diffractometer. FESEM (field emission scanning electron microscopy) (FEI 430 Nano Scanning Electron Microscope) was used to confirm surface morphology. EDX (Energy-dispersive X-ray spectroscopy was used for elemental mapping. The pore size distribution and specific surface area were analyzed by N_2 adsorption-desorption isotherm. FTIR (JASCU 6600) analysis was done to identify functional groups of MoO_3. The galvanostatic charge discharge measurements were accomplished using coin cells in which working electrode was prepared by making slurry of the active material, PVDF (polyvinylidene fluoride) binder and carbon black in a weight ratio of 75:15:10 in NMP (N- methylpyrrolidinone) solvent. The slurry was casted on Cu- foil (current collector) and was dried at 120 °C in vaccume oven and further cut in to 18mm discs prior assembling of the cell. The cell was assembled in Argon filled glove box where content of oxygen

and moisture was kept to less than 0.5 ppm. The anode and cathode was separated by glass microfiber separator. Galvanostatic cycling was performed using Biologic MPG-2 instrument at a current rate of 50, 100, 200 and 400 mA g^{-1}. The cyclic voltammetry was conducted in 0.01-3.0 V potential window at a scan rate of 0.5 mV s^{-1}. All experiments were done at 25 °C.

3.2.1 Structural analysis

The XRD patterns of pure Cr_2O_3, Cr_2O_3-MWCNTs $_{(12\%)}$ and Cr_2O_3-MWCNT$_{(12\%)}$-PANI are shown in Fig 3.1. The characteristics XRD patterns of all samples show good agreement with (JCPDS No 01-082-1484) indicating well crystallized rhombohedral geometry having the cell parameters: a = b = 4.9570 Å, c = -13.5923 Å and α = β = 90◦, γ = 120° with a space group of R-3C.
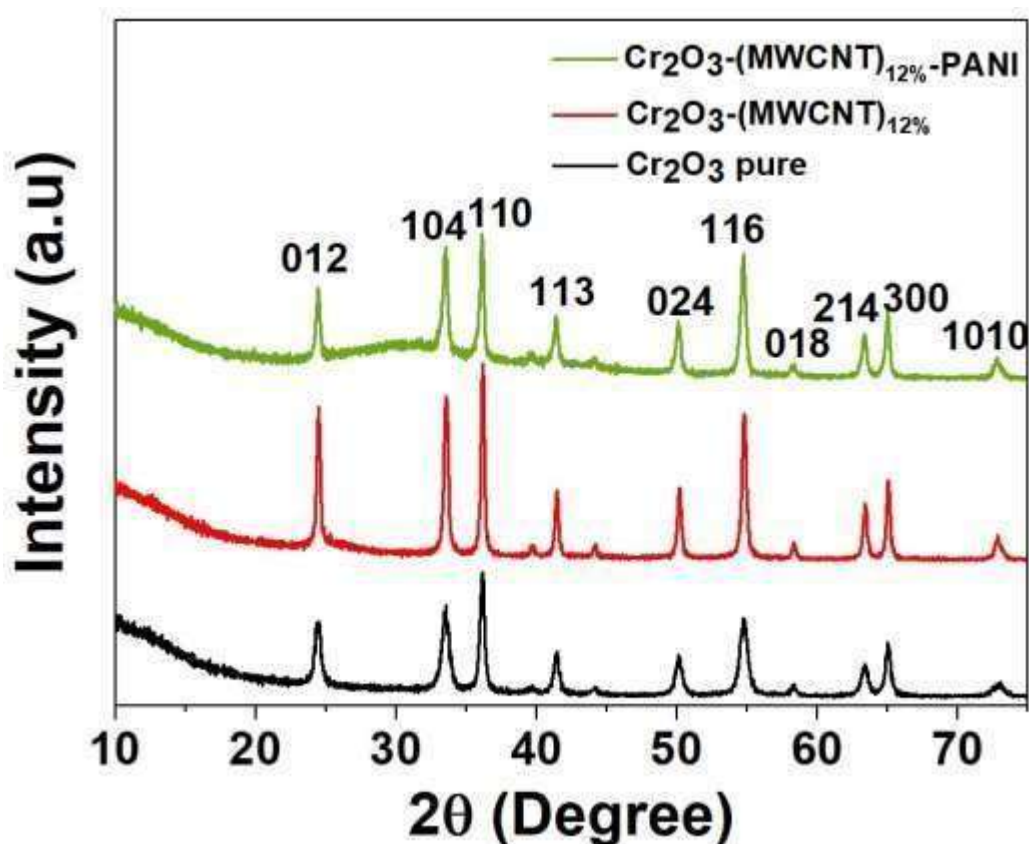
Figure 3.1 XRD spectra of Cr_2O_3, Cr_2O_3-MWCNTs$_{(12\ \%)}$ and Cr_2O_3-MWCNT$_{(12\%)}$-PANI.

No extra peaks were observed in the XRD pattern. Crystallite size (d_{crys}) was calculated according to Scherrer's formula $D = k\lambda/\beta\cos\theta$ where ($\lambda = 0.15406$ nm) is a wavelength for X-ray source, D is average crystallite size in nm, K is Scherrer constant and K = 0.89, β is the full width at half maximum and θ is Bragg angle in degrees.

Scherrer analysis show very small difference among crystallite size of samples. The crystallite size of Cr_2O_3, Cr_2O_3-MWCNTs$_{(12\%)}$ and Cr_2O_3-MWCNTs$_{(12\%)}$-PANI is found to be 23, 24.1 and 29.4 nm, respectively. All information about remaining samples is given in Fig 3.2.
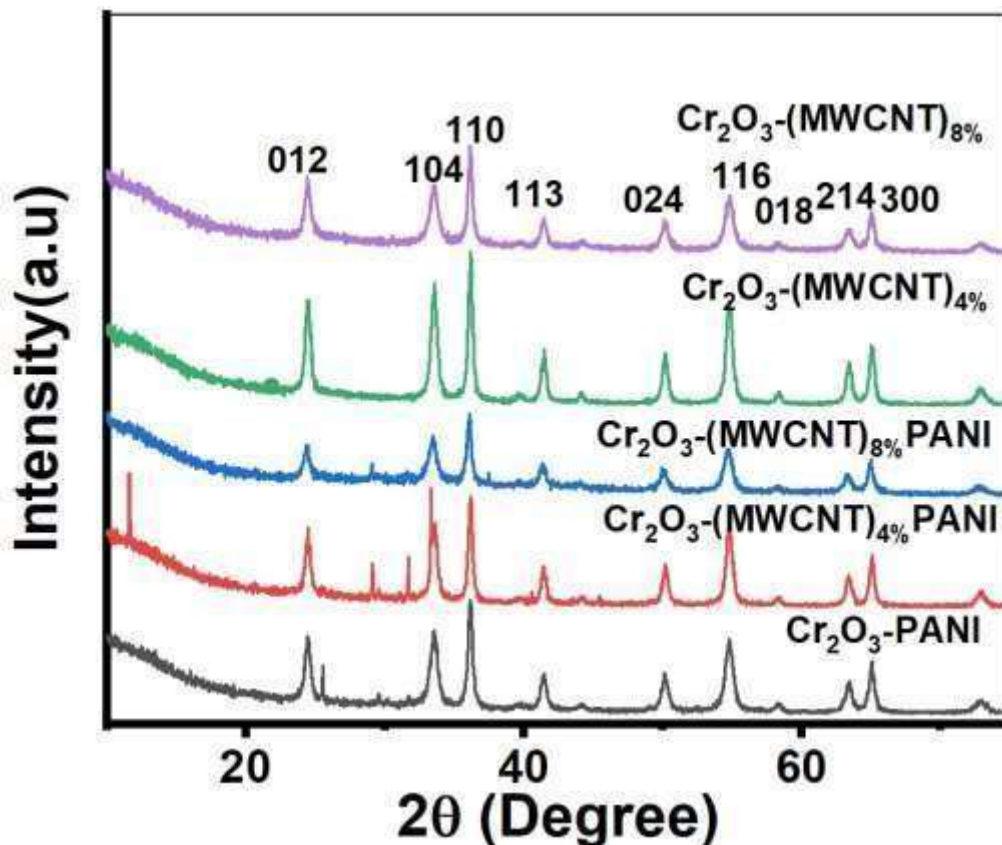
Figure 3.2 XRD spectra of nanocomposites

3.2.2 Morphological analysis

FESEM was used to describe the structure and morphology of pure Cr_2O_3, Cr_2O_3-MWCNTs$_{(12\%)}$ and Cr_2O_3-MWCNTs$_{(12\%)}$-PANI at low and high magnification as shown in Fig 3.3. FESEM images reveal that the nanoparticles acquire homogeneous quasi spherical shape displaying agglomeration between fine particles. FESEM image of Cr_2O_3-PANI sample is also represented in Fig 3.3. It can be observed that the Cr_2O_3 particles are uniformly distributed in PANI matrix as shown in Fig 3.3c. The EDX analysis, spectra reveal the presence of Cr, O and N. The average particle size is found to be around 50 nm. It is obvious from images that PANI forms a good coating on the surface of Cr_2O_3 nanoparticles. It shows stabilized interaction among metal oxide nanoparticles and quinoid ring of PANI exhibiting uniform adsorption of PANI. In 12%

MWCNTs content, the tubular network was observed with Cr_2O_3 nanoparticles showing that the nanoparticles are well dispersed around MWCNTs.
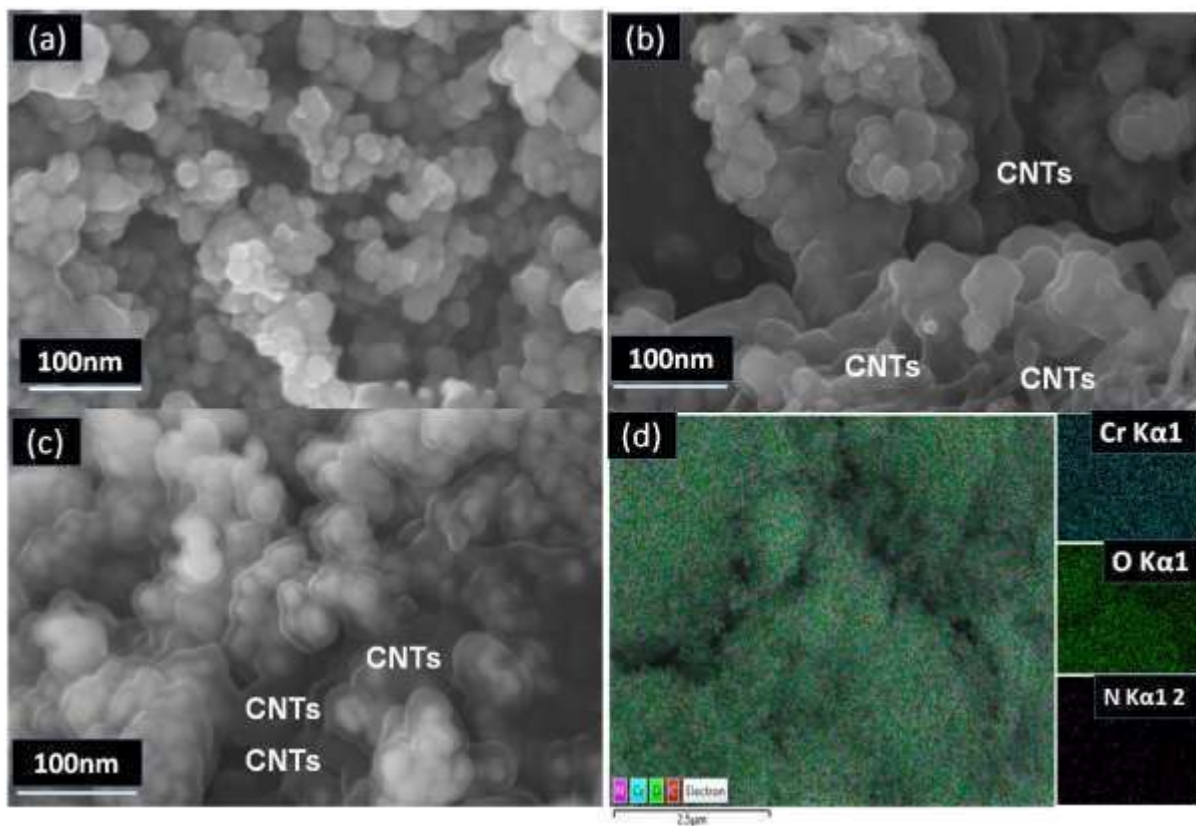
Figure 3.3 FESEM images of (a) pure Cr_2O_3 (b) Cr_2O_3-MWCNTs$_{(12\%)}$, (c) Cr_2O_3-MWCNT$_{(12\%)}$-PANI composite samples, d) EDX mapping of Cr_2O_3-MWCNT$_{(12\%)}$-PANI

In addition, elemental distribution map reveals that all elements are homogenously distributed over the Cr_2O_3 nanocomposite. Due to smaller particles size, the contact among nanoparticles is larger in a unit volume, so they can form agglomerates very easily.
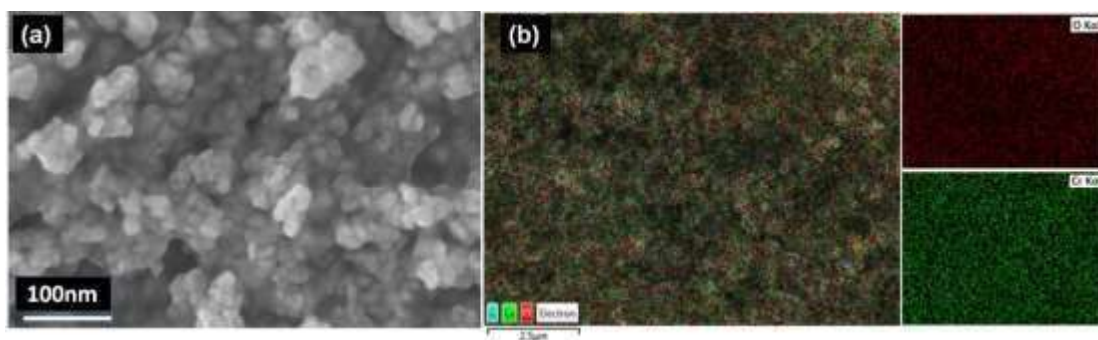
Figure 3.4 SEM image and EDS mapping of Cr_2O_3-(MWCNTS)$_{8\%}$ nanocomposite.

3.2.3 XPS analysis

XPS analysis was done to investigate binding configuration of Cr_2O_3-MWCNT$_{S(12\%)}$-PANI and Cr_2O_3-MWCNT$_{S(12\%)}$ as shown in Fig 3.5. The survey spectrum of Cr_2O_3-MWCNTs $_{(12\%)}$-PANI indicates presence of principle C1s, O1s, N1s and Cr2p with no impurities. In case of C_{1S} the deconvoluted peaks appears at binding energy of 284.6, 286.6 and 288.2 eV which corresponds to C=C, C=O and O-C=O bondings, respectively[119]. The peak signals in case of Cr2p were resolved into two spin orbit pairs at 576.9 eV for Cr $2p^{3/2}$ and 586.6 eV for Cr $2p^{1/2}$, respectively. The spin-obit coupling value for Cr2p was found to be 9.7 eV which confirms the Cr^{3+} oxidation state[21, 139]. The deconvolution of O1s exhibits two prominent peaks centered at 530 and 532 eV which can be attributed to C=O/C≡O and C=O-H/C-O-C[140]. Furthermore, the N1s peak could be deconvoluted into two peaks located at 399 and 411 eV which correspond to the formation of -NO and –NH in the carbon sheets. According to the literature N doped nanocomposites show better electrochemical performance. All these values are showing good agreement with the literature.
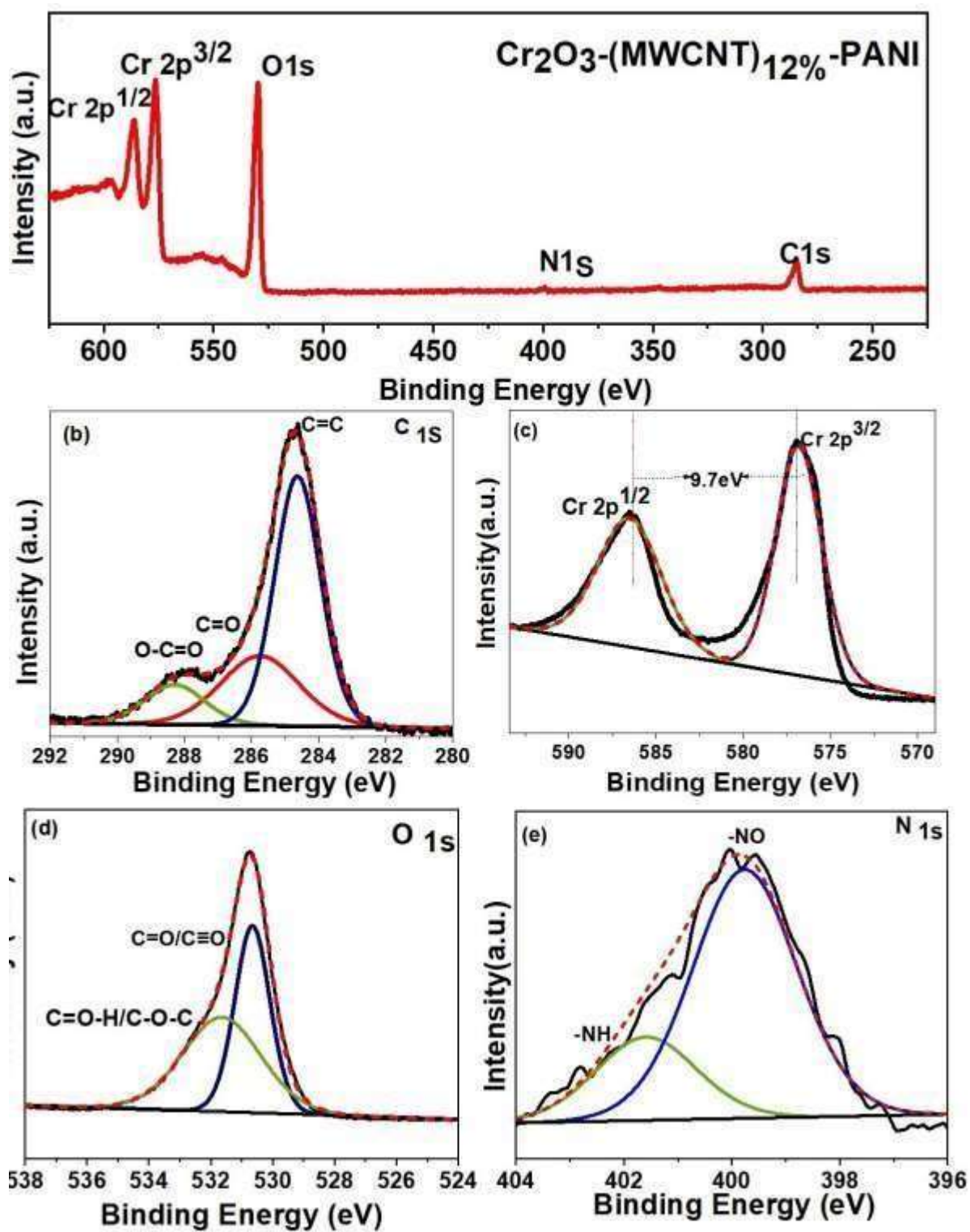
Figure 3.5 (a) XPS full survey scan of Cr_2O_3–$MWCNTs_{(12\%)}$-PANI, (b) HR spectra of C1s, (c) Cr2p, (d) O1s (e) N1s
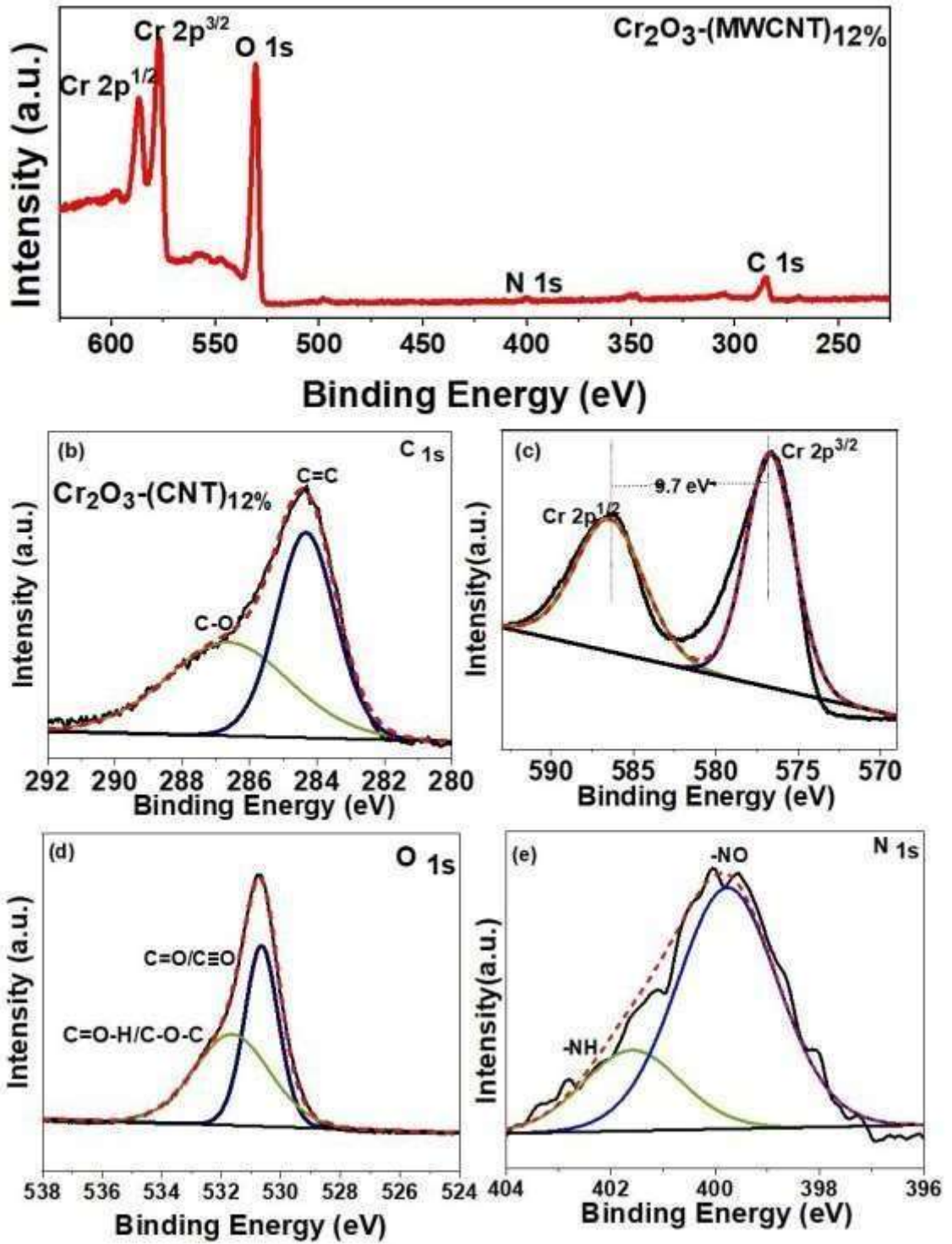
Figure 3.6 XPS of Cr_2O_3-(CNT)$_{12\%}$ nanocomposite

3.2.4 Band gap analysis

DRS analysis was carried out to evaluate the effect of MWCNTs and PANI coating on band gap of Cr_2O_3 nanoparticles. The optical band gap was determined by using Tauc's relation.

$$(\alpha h\nu) = A(h\nu - E_g)^n \quad (1)$$

Where, α is the absorption coefficient, n=1/2 for indirect band gap transition, hν is energy of photon and E_g is band gap. Band gap was calculated by extrapolating linear portion of curve[141, 142]. Samples containing MWCNT$_S$ show lower band gap energy because it increases the conductivity. The MWCNT$_S$ act as a good electron acceptor which accepts electrons from light and provide porous support that facilitate electron transport process[143]. MWCNTs possess good light absorbing properties, as the amount of MWCNTs increased absorption increased[144]. PANI also increases the absorption of nanocomposites to visible region as far as 800 nm. PANI containing samples give rise to more intense absorption resulting in decreased band gap[145]. The band gap of PANI coated samples is almost similar to MWCNTs containing samples which may be due to the fact that all these materials are conductive agents and therefore almost show similar effect. PANI also possesses band gap near 1.5 eV for the highest conductive emeralidine state and therefore these coated samples also show band gaps near to polyaniline emeralidine state. Such behavior is observed because electrons always prefer to jump to lower energy level which are situated for PANI and not for pure Cr_2O_3. Fig 3.7a shows the band gap near 1.6 eV which is lower than the reported[146]. Lowest band gap is associated with MWCNTs containing samples which is possibly due to the presence of additional electronic states created in the structure of Cr_2O_3 by adding MWCNTs, which are situated between the valence and conduction band as a result lower energy is required by electrons to jump from valence to the conduction band and freely move to impart conductance to whole system.

3.2.5 Thermogravimetric analysis

TGA of pure Cr_2O_3, Cr_2O_3-MWCNT$_{S(12\%)}$ and Cr_2O_3-MWCNT$_{S(12\%)}$-PANI was conducted to observe the thermal stability. Samples were heated to find relation between temperature and mass of samples from 25-800 °C in air atmosphere. No noticeable change was observed in case of pure Cr_2O_3 exhibiting great thermal stability. In case of Cr_2O_3-MWCNT$_{S(12\%)}$ mass losses leading to prominent dip starts at around 380°C and continues till 490 °C showing 8% loss, while in case of Cr_2O_3- MWCNT$_{S(12\%)}$-PANI dip starts at around 230 °C and ends at 480 °C showing 21% loss. After that these samples remain stable up to 800 °C as shown in Fig. 3.7b.

3.2.6 Functional group analysis

Fig. 3.7c shows FTIR spectra of pure Cr_2O_3, Cr_2O_3-MWCNTs$_{(12\%)}$ and Cr_2O_3-MWCNTs$_{(12\%)}$-PANI coated samples. The FTIR of MWCNTs containing samples are showing three bands having oxygen containing functional groups at 1730 cm^{-1} (C=O), 1352 cm^{-1} (C-OH), which confirm acid functionalization, while two peaks at 532 and 620 cm^{-1} correspond to symmetric and asymmetric vibrations of Cr-O providing clear evidence of crystalline Cr_2O_3 . The peaks at 1220 and 1483 cm^{-1} are attributed to stretching vibration of C=C and C-N of quinoid in PANI[147, 148].
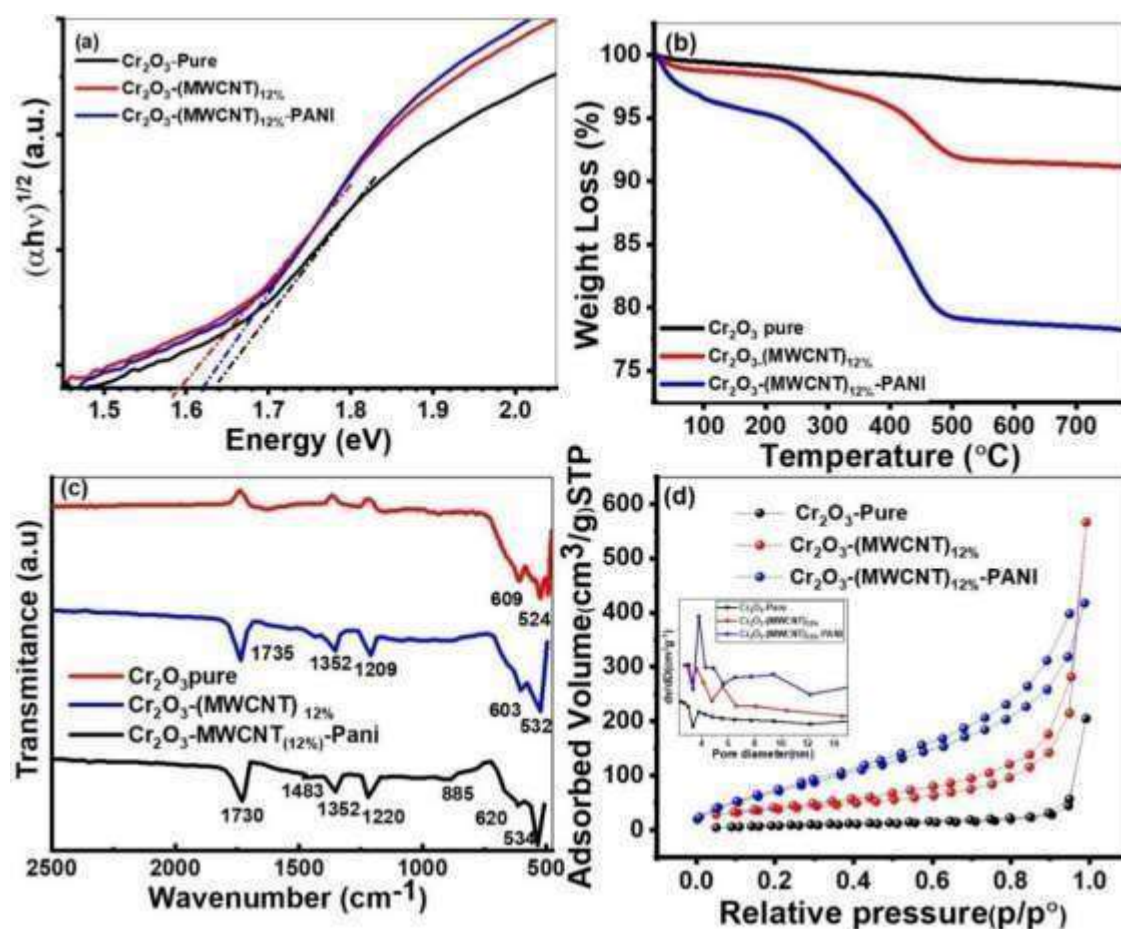
Figure 3.7 (a) Tauc plots, (b) TGA curves, (c) FTIR spectra of nanocomposites d) N$_2$ adsorption-desorption isotherms of pure Cr_2O_3, Cr_2O_3-MWCNTs$_{(12\%)}$ and Cr_2O_3-MWCNT$_{(12\%)}$-PANI

3.2.7 Surface area analysis

Nitrogen adsorption-desorption isotherm was used to evaluate the BJH pore size distribution and BET surface area. According to IUPAC, hysteresis feature is close to type-IV isotherm indicating mesoporous nature of the material. The BET surface area of Cr_2O_3, Cr_2O_3-MWCNTs$_{(12\%)}$, Cr_2O_3-MWCNTs$_{(12\%)}$-PANI is 27.2, 134 and 258 m^2 g$^-$

[1],respectively indicating that MWCNT$_S$ are helpful to achieve high active surface area. The pore volume of Cr$_2$O$_3$ and Cr$_2$O$_3$ -MWCNTs$_{(12\%)}$ and is 0.09 and 0.87, 0.901 cm^3 g^{-1}, respectively. The high pore volume and large surface area is associated with Cr$_2$O$_3$-MWCNTs$_{(12\%)}$ as shown in Fig 3.7d. Highly porous nature of material can be seen from large hysteresis loop between desorption and adsorption isotherm[1].

3.3 Electrochemical Measurements

The cyclic voltammetry was conducted in 0.01–3.0 V potential window at a scan rate of 0.5 mV s^{-1}. All experiments were done at 25 °C.

3.3.1 Cyclic voltammetry (CV)

The CV profile of all Cr$_2$O$_3$ electrodes with MWCNT$_S$ and PANI for two cycles are shown in Fig 3.8(a-c). Two cathodic peaks were observed in the first negative scan, one small peak appeared at 0.45 V as well as a sharp peak was observed at 0.01 V. One small reduction peak at 0.45 V corresponds to unstable solid electrolyte interface (SEI) that forms at the surface of the electrode owing to decomposition of electrolyte[21]. This peak completely disappeared in the 2nd cycle because SEI layer was unstable due to volume change in first conversion/deconversion cycle[1].
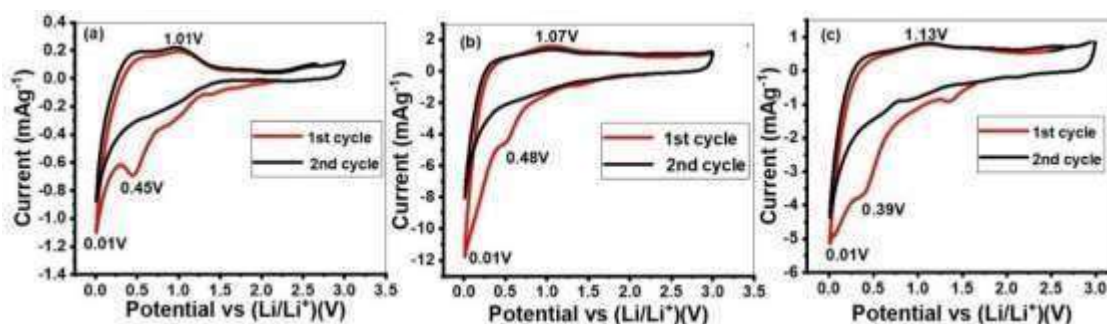
Figure 3.8 CV profiles for (a) Cr$_2$O$_3$ b) Cr$_2$O$_3$–MWCNTs$_{(12\%)}$ c) Cr$_2$O$_3$-MWCNTs$_{(12\%)}$-PANI nanocomposite.

However, in next cycles the cathodic peak remains stable, confirming high coulombic efficiency and good reversibility of all the samples. Another sharp peak at 0.01 V is assigned to conversion reaction of Cr$_2$O$_3$ with Li$^+$. The peak appeared at 0.01 V persisting in next cycles for all the nanocomposites. Meanwhile anodic peak was observed at 1.01 V corresponding for deconversion reaction of Cr$^\circ$ to Cr^{3+}. Clearly, for all nanocomposites the first cycle is significantly different from the next cycle[21, 149].
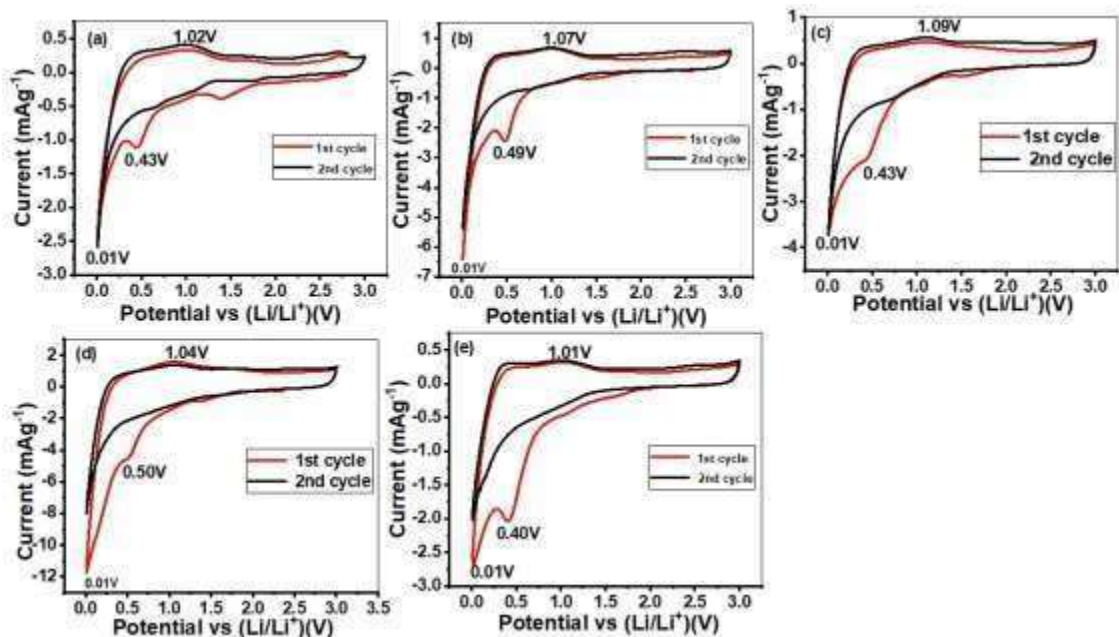
Figure 3.9 CV profiles for Cr_2O_3 nanocomposite.

Fig 3.9 indicates CV of pure Cr_2O_3 and its composite with RGO. Two prominent oxidation and reduction peaks were observed in both cases.
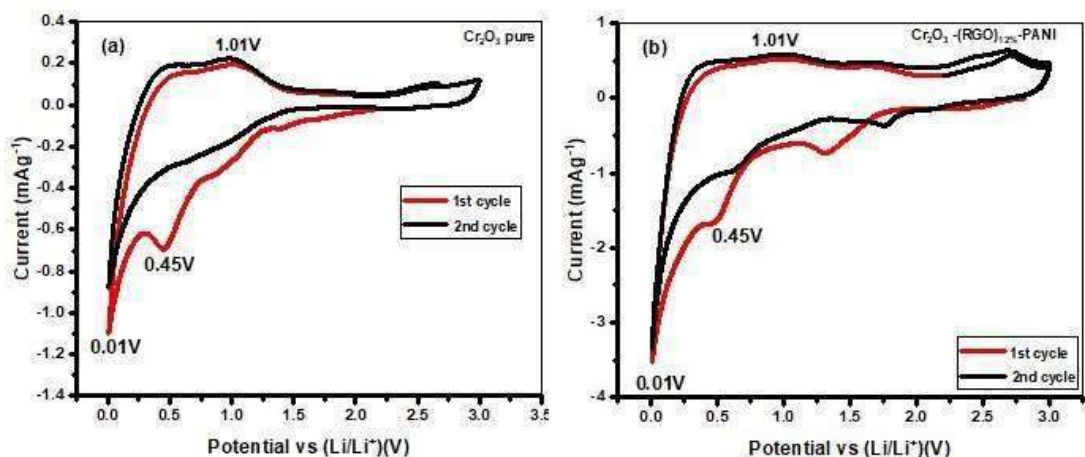
Figure 3.10 Cv of Cr_2O_3 pure, Cr_2O_3-RGO $_{(12\%)}$-PANI

3.3.2 Galvanostatic charge discharge measurements (GCPL)

Fig. 3.11(a-c) shows voltage-capacity profiles for pure Cr_2O_3, Cr_2O_3-MWCNTs$_{(12\%)}$, Cr_2O_3-MWCNTs $_{(12\%)}$-PANI based electrodes for 1st, 2nd and 10th cycle at a current density of 100 mA g^{-1} in the voltage range of 0.01-3.00 V.
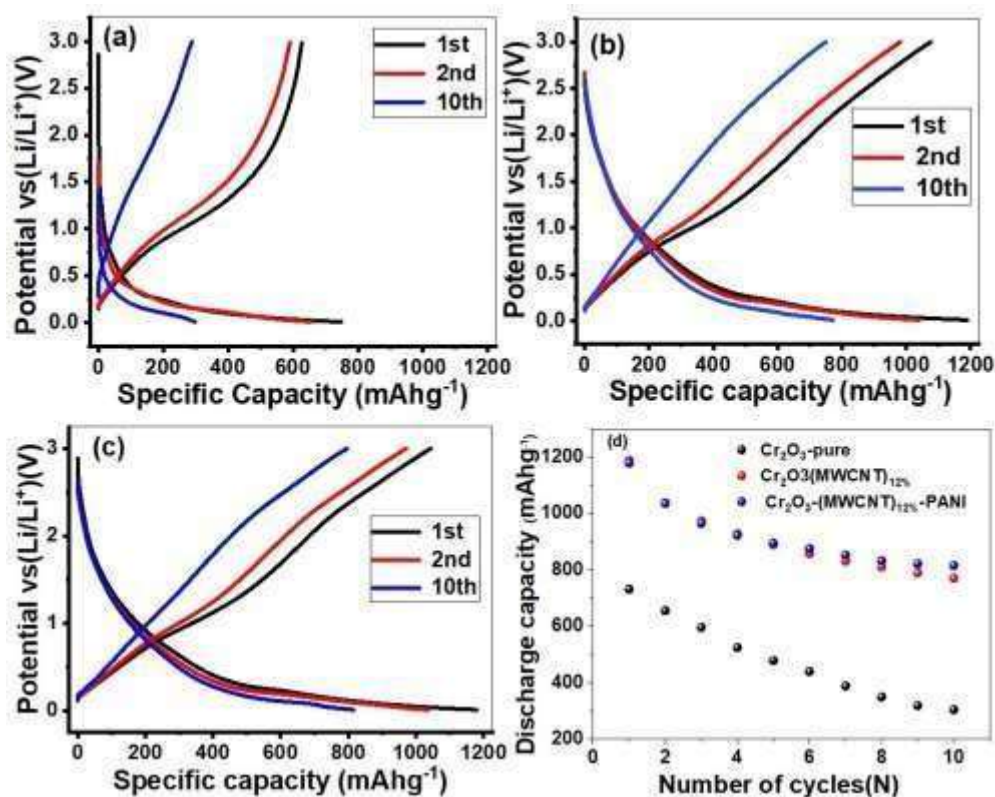
Figure 3.11 Charge/discharge profiles for (a) Cr_2O_3 b) Cr_2O_3–MWCNT$_{S(12\%)}$ c) Cr_2O_3–MWCNT$_{S\ (12\%)}$-PANI nanocomposites d) Cyclic performance of electrodes materials

A sharp difference in discharge capacities were observed for all samples in first two cycles owing to extra charge stored in the first cycle[149] or unstable SEI film which result in irreversible lithium loss from incomplete conversion reaction [150]. It was observed that by raising amount of MWCNTs from 4% to 8% the specific capacity is also increased from 868 to 924 mAh g^{-1} (Fig 3.12), however when 12% MWCNT$_S$ were added to form Cr_2O_3-MWCNT$_{S(12\%)}$ nanocomposite, the capacity increased considerably and 1188 mAh g^{-1} was achieved. Thus, it was confirmed that amount of MWCNTs with Cr_2O_3 has considerable effect on the specific capacity[151]. Among all these samples, Cr_2O_3–MWCNTs$_{(12\%)}$-PANI demonstrate good capacity retention and reversible charge/discharge capacity of 1178/815 mAh g^{-1} at the end of 10th cycle. Although, initial discharge capacity is less than Cr_2O_3-MWCNT$_{(12\%)}$ but it shows good stability because of PANI coating while bare Cr_2O_3 and Cr_2O_3-PANI deliver low reversible capacity of 731/304 and 692/370 mAh g^{-1}, respectively.
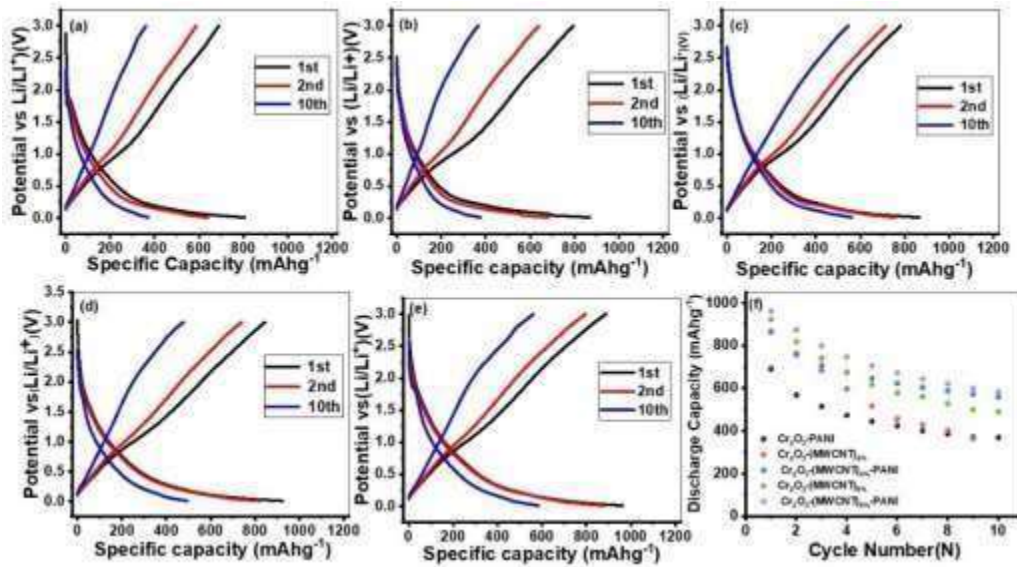
Figure 3.12 Charge/discharge profiles for Cr_2O_3 nanocomposites d) Cyclic performance of electrodes materials

More importantly, Cr_2O_3-MWCNTs$_{(12\%)}$-PANI shows 88% initial coulombic efficiency and 97.01% coulombic efficiency at the end of 10th cycle. The improved coulombic efficiency could be mainly attributed to PANI coating which not only enhance electrical conductivity of nanocomposites but also provide enough free space for volume change that occur during charging/discharging process resulting in excellent stability[21]. From these studies, it can be concluded that Cr_2O_3-MWCNTs$_{(12\%)}$-PANI shows the best cycling performance. It was observed that MWCNTs help to maintain capacity and potentially stabilize the electrode after multiple cycles while, MWCNTs with polymer act as a buffering mixture and avoid many problems related to volume changes and poor connection between active electrode material and current collector. Cr_2O_3-$(RGO)_{12\%}$-PANI exhibited discharge capacity of 891.81mAhg^{-1} at 100mAg^{-1} .
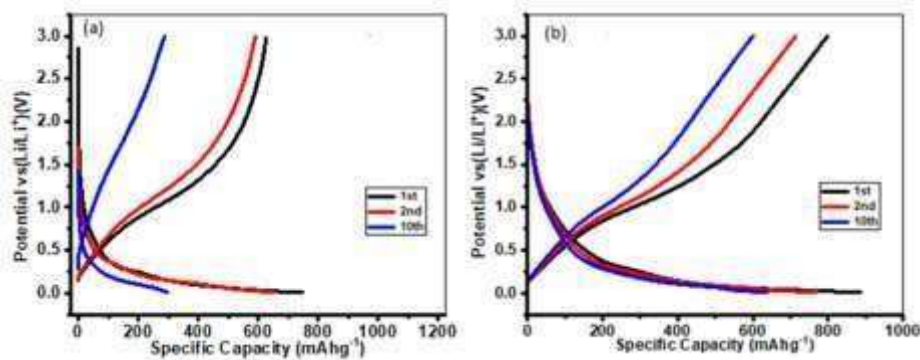
Figure 3.13 Galvanostatic Charge/discharge profiles for (a) Cr_2O_3 b) Cr_2O_3-$(RGO)_{12\%}$-PANI.

3.3.3 Rate capability

Figure 3.14 (a-c) shows variation in the rate capability of Cr_2O_3-MWCNTs $_{(12\%)}$, Cr_2O_3-MWCNTs $_{(12\%)}$-PANI and bare Cr_2O_3 at different current densities of 100, 200 and 400 mA g^{-1} for 10 cycles each between cut-off voltages of 0.01-3.0V. Much better electrochemical performance is associated with Cr_2O_3-MWCNTs$_{(12\%)}$ and Cr_2O_3-MWCNTs$_{(12\%)}$-PANI showing capacities of 1188, 656, 483 and 1178, 756, 544 mAh g^{-1} at 100, 200 and 400 mA g^{-1}, respectively. The values of capacities are better than the theoretical capacity of graphite electrode (372 mAhg^{-1}). After 30 cycles at higher current rates, galvanostatic cycling of samples was continued at 100 mAh g^{-1} for 5 more cycles. A relatively high capacity of 584 and 719 mAhg^{-1} were observed showing that the structure of nanocomposites was not disrupted at higher current rates. Whereas the capacity of bare Cr_2O_3 drop quickly with increase of cycle number. At higher current rates after 30 cycles, specific capacity of bare Cr_2O_3 is only 138 mAhg^{-1} showing capacity retention of only 21.06%. The poor performance of bare Cr_2O_3 could be due to high resistance[21] , volume variation[120] , aggregation of pulverized particles during charge/discharge process [119], structural rearrangements at a higher current rates or may be due to weak electrical contact between electrode material and current collector[151] . After 30 cycles, when the current is brought back to 100 mA g^{-1} for 5 more cycles then low reversible capacity of 199 mAh g^{-1} achieved. However, Cr_2O_3–PANI shows capacity of 176.13 mAh g^{-1} on 30 cycles show capacity retention of 25% at 400 mA g^{-1}(Fig 3.14). These results further confirm the significance of MWCNTs to attain the high-rate capability. MWCNTs maintain structural stability, reduce particle agglomeration and increase inter and intraparticle interaction. Cr_2O_3-MWCNTs$_{(12\%)}$-PANI shows excellent stability and reversibility. The improved reversible capacity, stability of Cr_2O_3-MWCNTs-PANI nanocomposite is attributed to the conductive path for electron transportation, good electric conductivity of nanotubes and polymer coating. Polymer coating not only significantly enhance initial capacity but also increases the stability[147]. Moreover, MWCNTs provide robustness and structural decency of electrode through volume change suppression during cycling process. After polymer coating, Cr_2O_3 nanocomposites show better cycling stability and good coulombic efficiency. This means that polymer coating plays vital role in improvement of cycling performance of Cr_2O_3-MWCNTs$_{(12\%)}$-PANI anode materials. Nevertheless,

the high capacity and good cycling performance of Cr_2O_3-MWCNTs$_{(12\%)}$-PANI make it good candidate as anode for lithium ion battery application.
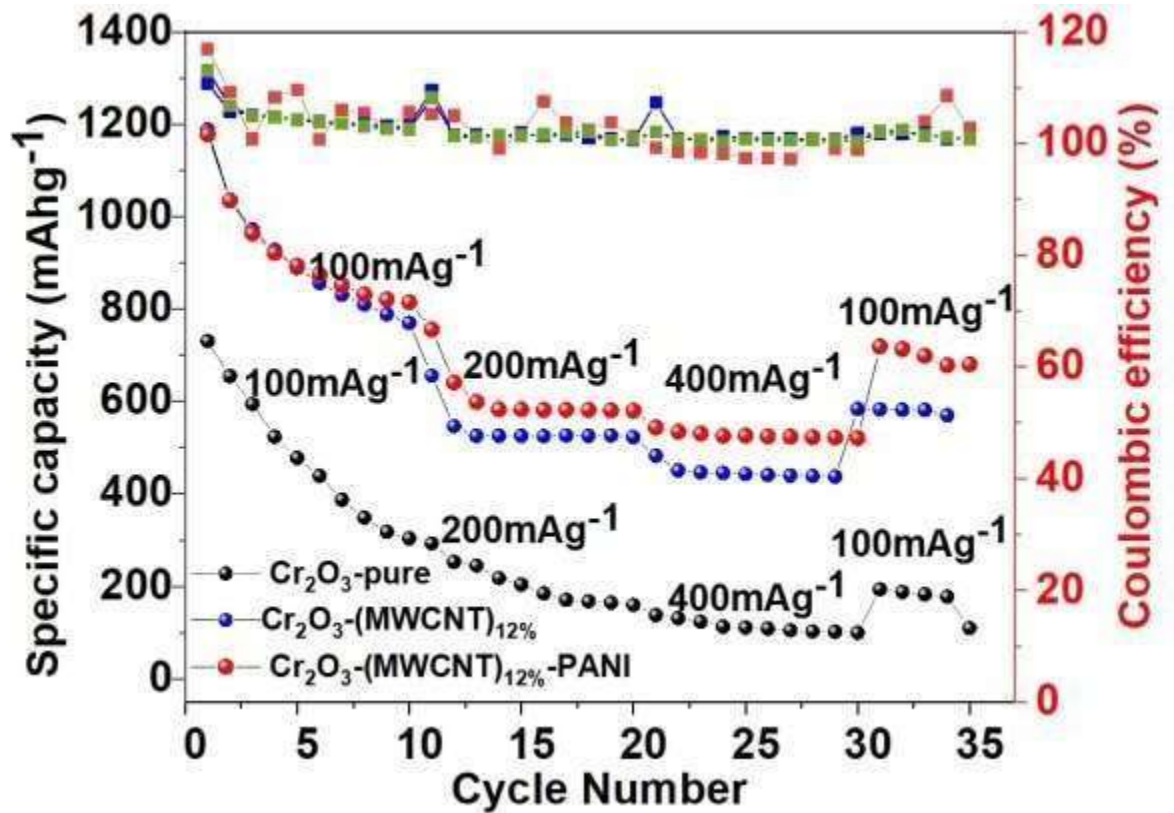
Figure 3.14 Rate capability of (a) Cr_2O_3 (b) Cr_2O_3–MWCNT$_{S(12\%)}$ (c) Cr_2O_3–MWCNT$_{S(12\%)}$-PANI nanocomposites.
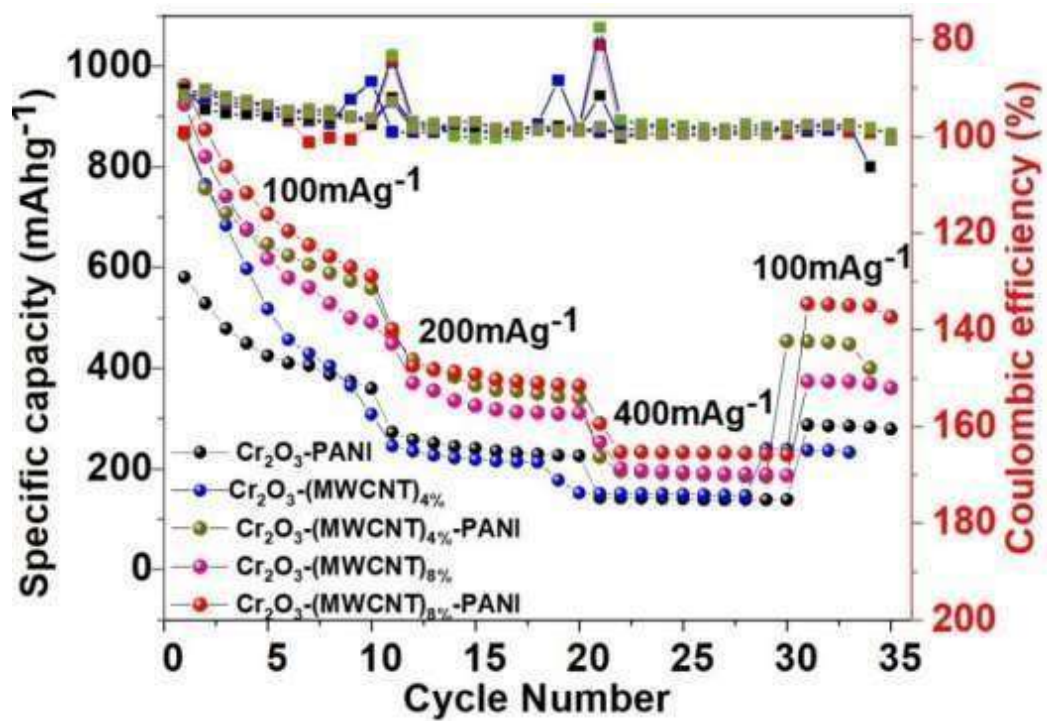
Figure 3.15 Rate capability of (a) Cr_2O_3 (b) Cr_2O_3–$MWCNT_{S(12\%)}$ (c) Cr_2O_3–$MWCNT_{S(12\%)}$-PANI nanocomposite
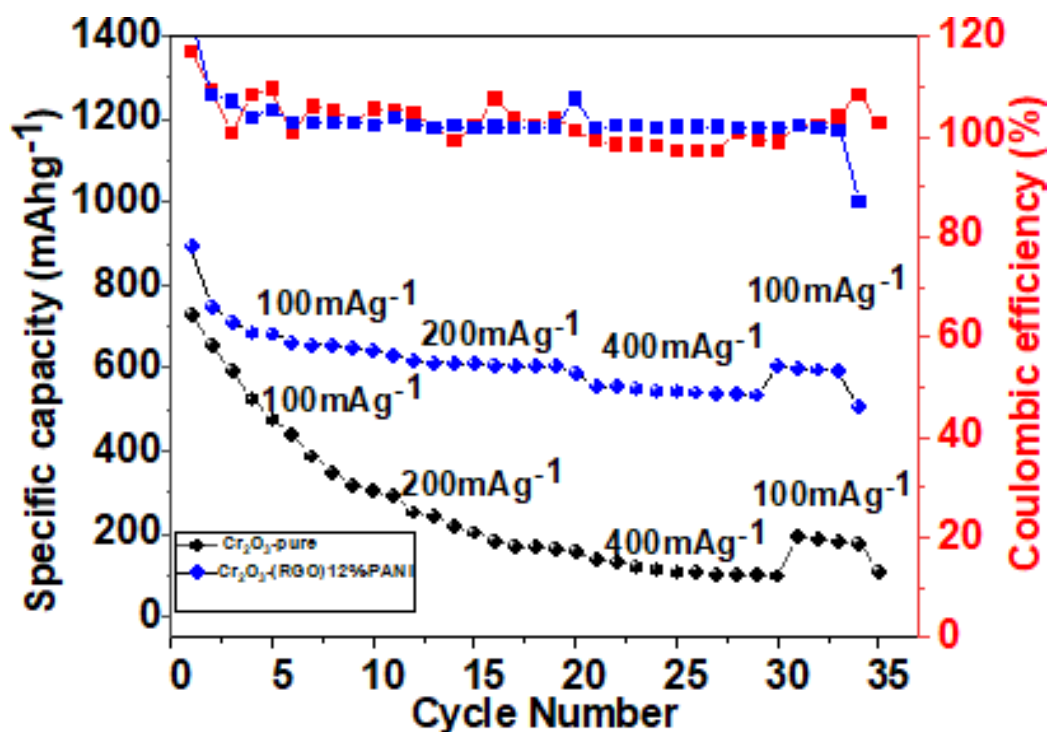
Figure 3.16 Rate capability of (a) Cr_2O_3 pure (b) Cr_2O_3–$RGO_{(12\%)}$-PANI

Cr_2O_3-$(RGO)_{12\%}$-PANI exhibited discharge capacity of $891.81 mAhg^{-1}$ at $100 mAg^{-1}$ and $535.8 mAhg^{-1}$ at $400 mAg^{-1}$ after 30 cycles as shown in Fig 3.15.

3.3.4 Electrochemical impedance spectroscopy (EIS)

EIS measurements were performed on all nanocomposites as displayed in Fig 3.17(a-b). The Nyquist plot shows two types of semicircles one in medium frequency range and other in high frequency range. Semicircles that appear in the high frequency region provide information about contact resistance and SEI, while semicircles in medium frequency region give information about charge transfer resistance of electrode electrolyte interface[152]. Anyhow, cell impedance is measured in medium frequency region of semicircle. Cr_2O_3 -$MWCNTs_{(12\%)}$-PANI have smaller semicircle diameter showing lowest charge transfer resistance of 23.5Ω. Thus, it signifies the high discharge capacity, while bare Cr_2O_3 show the highest impedance of about 1044Ω as shown in Fig. 3.17(a). The EIS data is simulated according to the circuit shown as inset of Fig. 9 with R_1, R_2 and R_3 representing solution (R_S), surface film (R_{SF}) and charge transfer R_{CT} resistance. Therefore, it can be concluded that $MWCNT_S$ and PANI play significant role in increasing electronic conductivity and reducing charge transfer

resistance. MWCNTs also act as a shock absorber that resist variations of pore size of nanoparticles, resulting in good electrochemical performance for LIBs. All values of other samples are provided in the supporting information (Table 3.1).
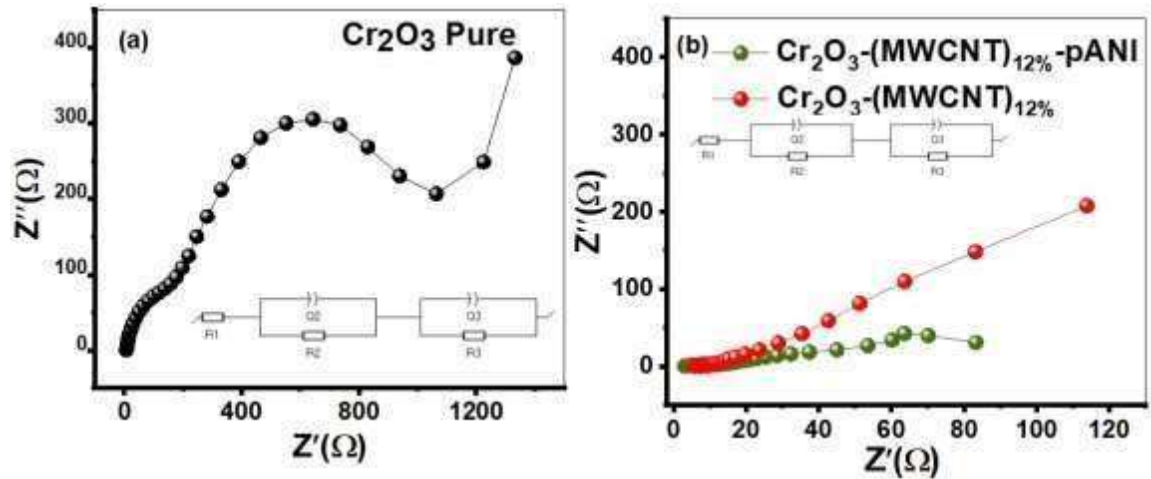
Figure 3.17 (a) The equivalent circuit and Nyquist plots of Cr_2O_3 (b) Cr_2O_3-MWCNTs$_{(12\ \%)}$ and Cr_2O_3-MWCNTs$_{(12\%)}$-PANI nanocomposite samples.
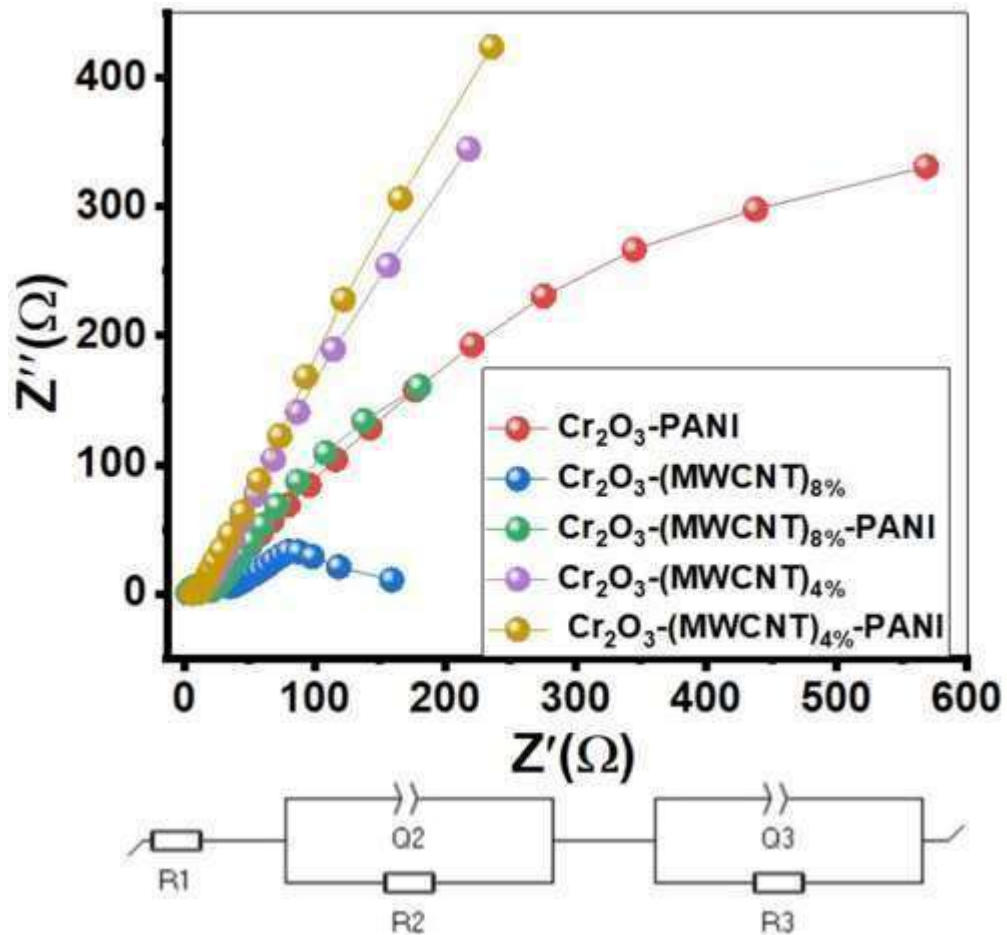
Figure 3.18 EIS simulation of all the synthesized samples

Table 3.1 EIS simulation data for all the samples

Sample	R_S (Ω)	R_{CT} (Ω)	R_{SF} (Ω)
Cr_2O_3	3.963	1044	383.5
Cr_2O_3-PANI	2.764	235	323.5
Cr_2O_3-MWCNT (4%)	2.451	27.07	178.8
Cr_2O_3-MWCNT(4%)-PANI	3.707	11.95	219.2
Cr_2O_3-MWCNT (8%)	2.357	33.7	125
Cr_2O_3-MWCNT(8%)-PANI	1.469	25.47	164.2
Cr_2O_3-MWCNT (12%)	2.741	24.5	95.42
Cr_2O_3-MWCNT(12%)-PANI	2.952	23.5	68.9

3.4 MoO_3 as anode materials for LIBs

Molybdenum oxides (MoO_3) have recently garnered significant attention due to their exceptional chemical stability, substantial theoretical capacity of 1117, and environmentally friendly nature [8–10]. Nevertheless, molybdenum oxides exhibit limited electrical conductivity and experience significant volume fluctuations (approximately 104%) during the insertion and extraction of lithium ions in their coarse state. These factors contribute to sluggish electrode reaction kinetics, poor cycling performance, and ultimately impede their practical use in lithium-ion batteries (LIBs). Diverse methodologies were employed to address these issues, such as diminishing particle size, fabricating composites containing exceptionally conductive substances like carbon nanotubes (CNTs) and reduced graphene oxide (RGO).Furthermore, PANI coating can also be employed[153].

3.5 Physicochemical Characterization

Physiochemical characterizations were performed through XRD, SEM , XPS analysis to evaluate crystal structures , morphological analysis.

3.5.1 Structural analysis

Fig 3.19 depicts XRD patterns for MoO_3 pure and its nanocomposites, indicating orthorhombic MoO_3 phase for all samples with no diffraction peaks for other

impurities with the lattice parameters (a=3.962 Å, b=13.85 Å, c =3.6970) which are well consistent with JCPDS card no 05-058[70, 154-156].The three sharp peaks at 23.46, 25.82 and 27.46 can be perfectly indexed to crystalline orthorhombic phase however, other minor peaks are also showing best match with the JCPDS card. This observation shows that PANI coating does not affect the crystal lattice of MoO_3 and structure is preserved.
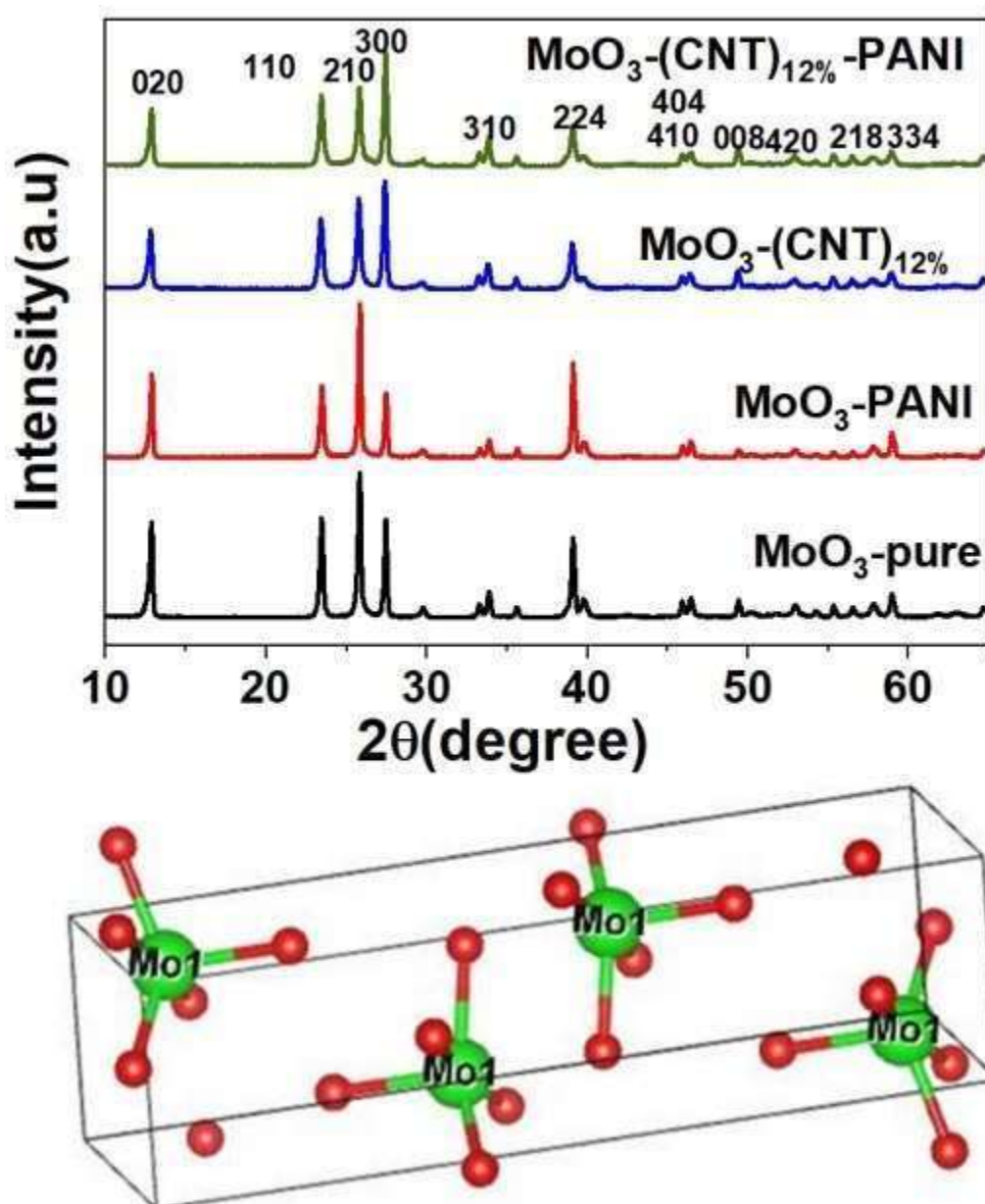
Figure 3.19 XRD patterns of samples and orthorhombic crystal structure of MoO_3.

The crystallite size for various synthesized samples was calculated using Debye-Scherrer equation as represented: λ is incident   wavelength of x-rays which is

1.5406nm, β is the full width at half maximum of the selected peak in radians and θ is diffraction angle(Bragg's angle) at which peak arises and is also taken in radians[157]. The crystallite size of the materials are as follows MoO_3(48.6), MoO_3-PANI(41.43nm), MoO_3-$(CNT)_{12\%}$(39.7nm) and MoO_3-$(CNT)_{12\%}$-PANI is 47nm, respectively as shown in Fi3.20.

$$D= k\lambda/\beta\cos\theta$$

Where D represents crystallite size, K represents constant usually taken as 0.9.
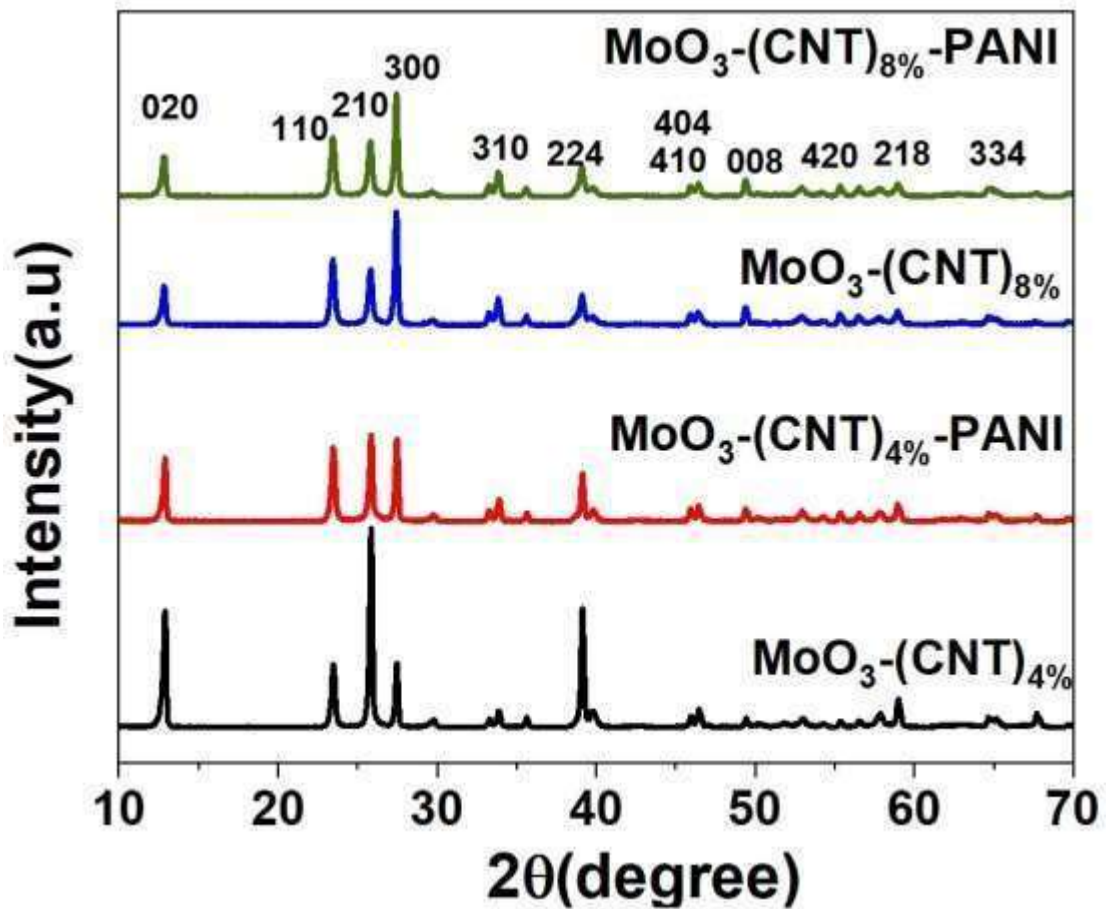
Figure 3.20 XRD patterns of samples and orthorhombic crystal structure of MoO_3.

3.5.2 Morphological analysis

The surface morphologies of the MoO_3 pure and their nanocomposites were investigated by SEM. Pure α-MoO_3 presents uniform plate like structure that appears like clusters of nanoflowers at low magnifications as shown in Fig 3.21. At high magnification it is showing flat smooth surface with semicircular tip. These plates[158]

combine layer by layer to form well oriented microbelts showing perfect morphology and well crystallinity.
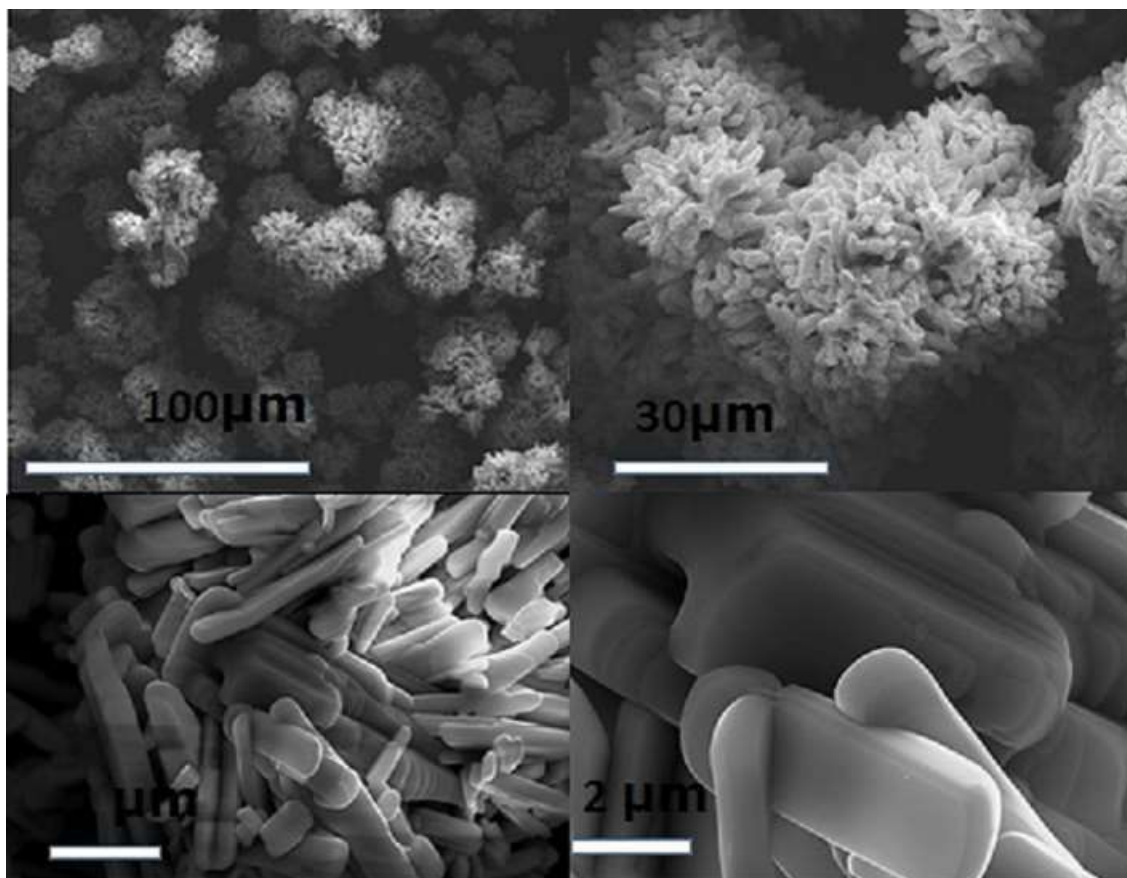
Figure 3.21 FESEM images of MoO_3-pure.

MoO_3 maintains plate like morphology after addition of CNTs, but with small size, unsmooth particle surface and little disorder as shown in Fig 3.22. It was also observed that CNTs are well dispersed around MoO_3 nanoparticles. EDX analysis was also done to determine relative abundance and elemental composition. The corresponding EDS mapping exhibits existence of Mo, O and C.
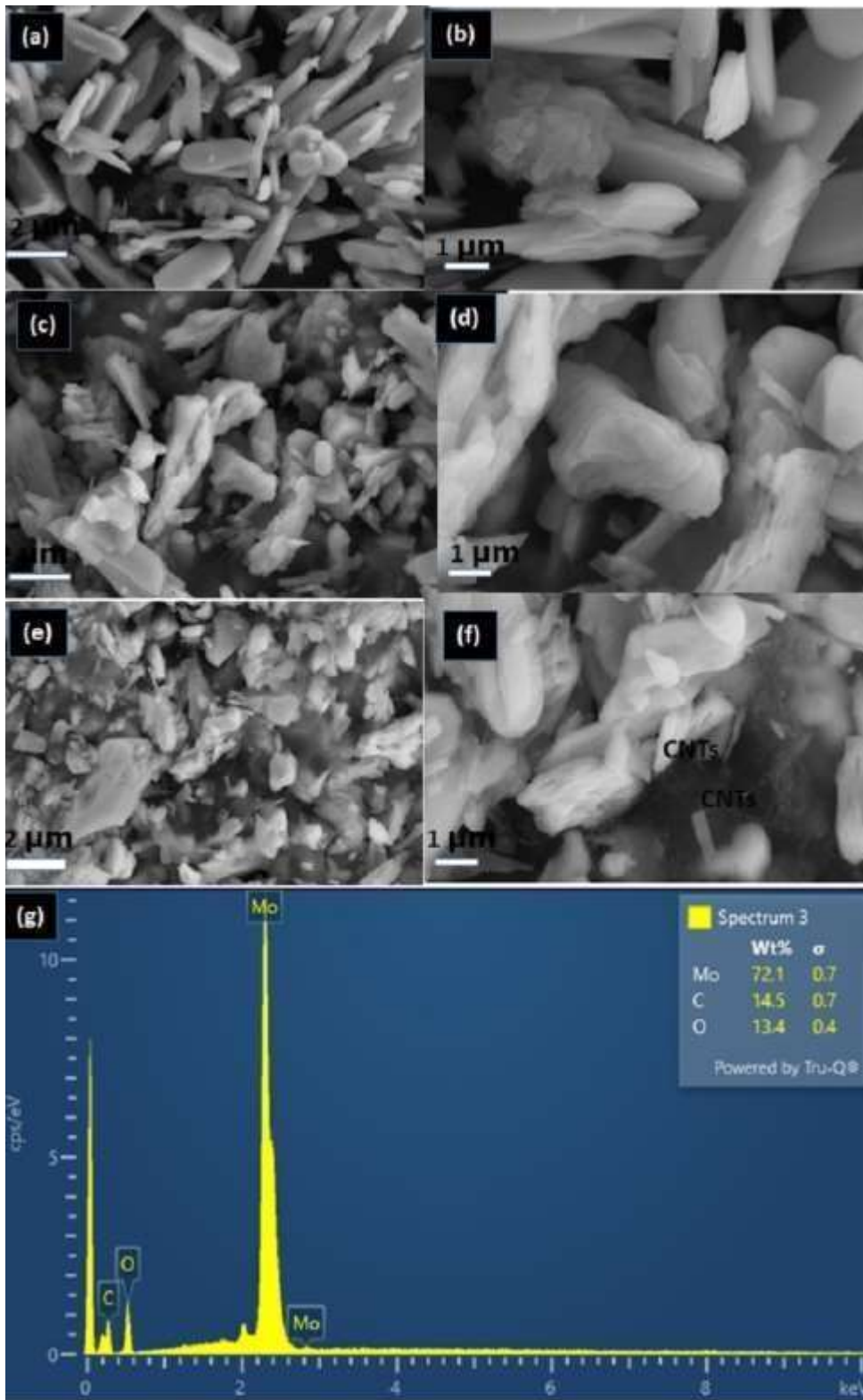
Figure 3.22 FESEM images of sample (a-b) MoO$_3$-PANI, (c-d) MoO$_3$-(CNT)$_{12\%}$,(e-f) MoO$_3$-(CNT)$_{12\%}$-PANI (g) EDX spectrum of MoO$_3$.

3.5.3 Functional group analysis

FTIR (Fourier transform infrared) spectroscopy was employed to investigate the bonding and functional groups of MoO_3. FTIR analysis was carried out in a transmittance mode for structure elucidation as well as to assess bonding present between various components as shown in Fig 3.23. Two peaks were observed at $565cm^{-1}$ and $678cm^{-1}$ displaying bending and stretching vibration of MoO[159]. The peaks at $852cm^{-1}$ and $980cm^{-1}$ are assigned to stretching vibration of O-Mo-O bond, stretching vibration of oxygen in Mo-O-Mo. The small peaks observed at $1471cm^{-1}$ and $1644cm^{-1}$ corresponds to bending vibrations of H–O–H. It also show presence of water of crystallization in MoO_3.
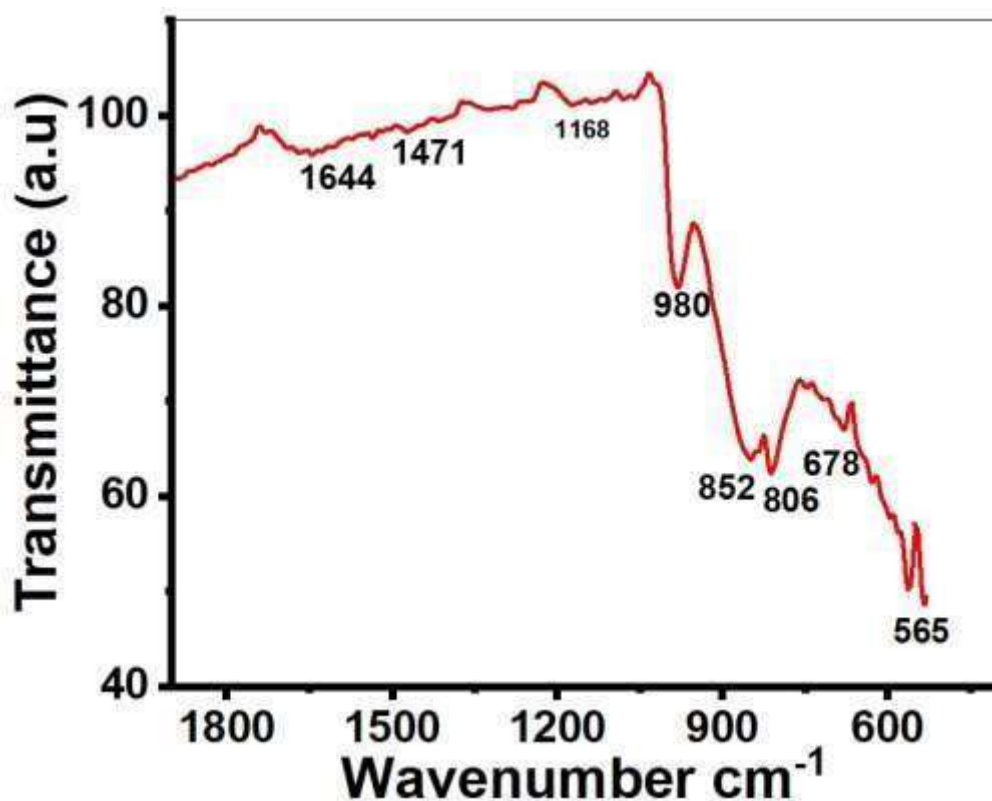
Figure 3.23 FTIR spectrum of the calcined MoO_3.

3.5.4 Surface area analysis

Pore-size distributions and the nitrogen adsorption-desorption isotherms of MoO_3 pure, MoO_3-PANI, MoO_3-(CNT)$_{12\%}$ and MoO_3-(CNT)$_{12\%}$-PANI composites are shown in Fig 3.24. MoO_3 show almost no adsorption at relative pressure less than 0.9, while it start showing small adsorption when relative pressure approaches 1.0. On the contrary, in case of MoO_3-CNTs $_{(12\%)}$-PANI with the increase of relative pressure adsorption

quantity increases gradually. In addition, in the 0.9-1.0 relative pressure range hysteresis loop was observed. The BET surface areas of MoO_3, MoO_3-PANI, MoO_3-$(CNT)_{12\%}$ and MoO_3-$(CNT)_{12\%}$-PANI are 0.849 and 4.017 m²/g, 19.8 m²/g and 41.3 m²/g respectively and the BJH (Barrett−Joyner−Halenda) pore volumes are 0.0018, 0.008 cm^3g^{-1},0.072 cm^3g^{-1} and 0.143 cm^3g^{-1}, respectively. MoO_3-$(CNTs)_{12\%}$-PANI displays broad pore-size distribution in of 5−150 nm pore diameter range. The porous structure with large surface area make charge transfer easier at electrode/electrolyte interface due to additional access points to electrolyte.
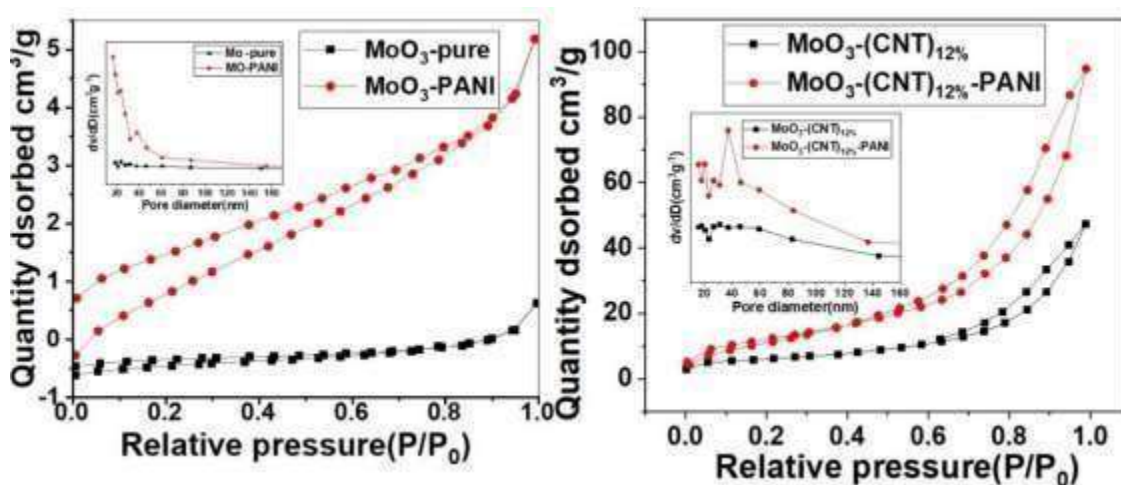
Figure 3.24 N_2 adsorption/desorption isotherm of MoO_3 at 77 K and pore size distribution curve in the inset of fig.

3.6 Electrochemical Measurements

CV of all the MoO_3 based electrodes at scan rate of 0.5 mVs^{-1} over a potential range of 0.01–3.0 V.

3.6.1 Cyclic voltammetry (CV)

Fig 3.25 Shows CV of all the MoO_3 based electrodes for the first two cycles. Three broad peaks can be seen at 2.11V, 2.57V and 0.01V vs. Li$^+$/Li in first cycle of the cathodic polarization process, corresponds to lithium intercalation processes, while current anodic peak at 1.25V was seen in anodic polarization corresponds to lithium extraction processes.
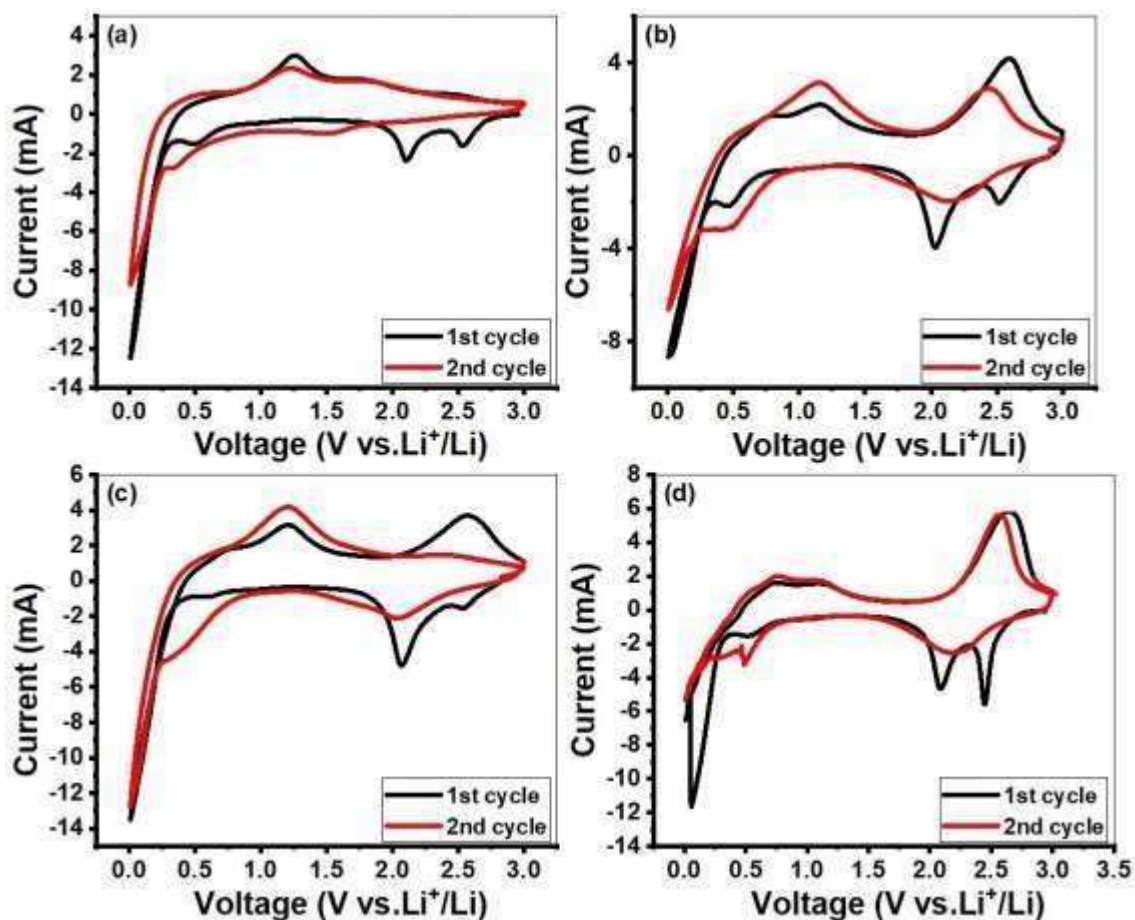
Figure 3.25 Cyclic voltammograms curves of all nanocomposites a) MoO_3 b) MoO_3-PANI c) MoO_3– CNTs $_{(12\%)}$ d) MoO_3-CNTs$_{(12\%)}$-PANI nanocomposite.

More specifically, these types of anodic and cathodic peaks at these potentials represent lithium insertion/de insertion in different structural sites of MoO_3 to form Li_xMoO_3. The strong peak at 0.01V appears due to lithiation of MoO_3. The area of peak in first cycle is more than the second cycle, which may be attributed to irreversible conversion reaction[160].
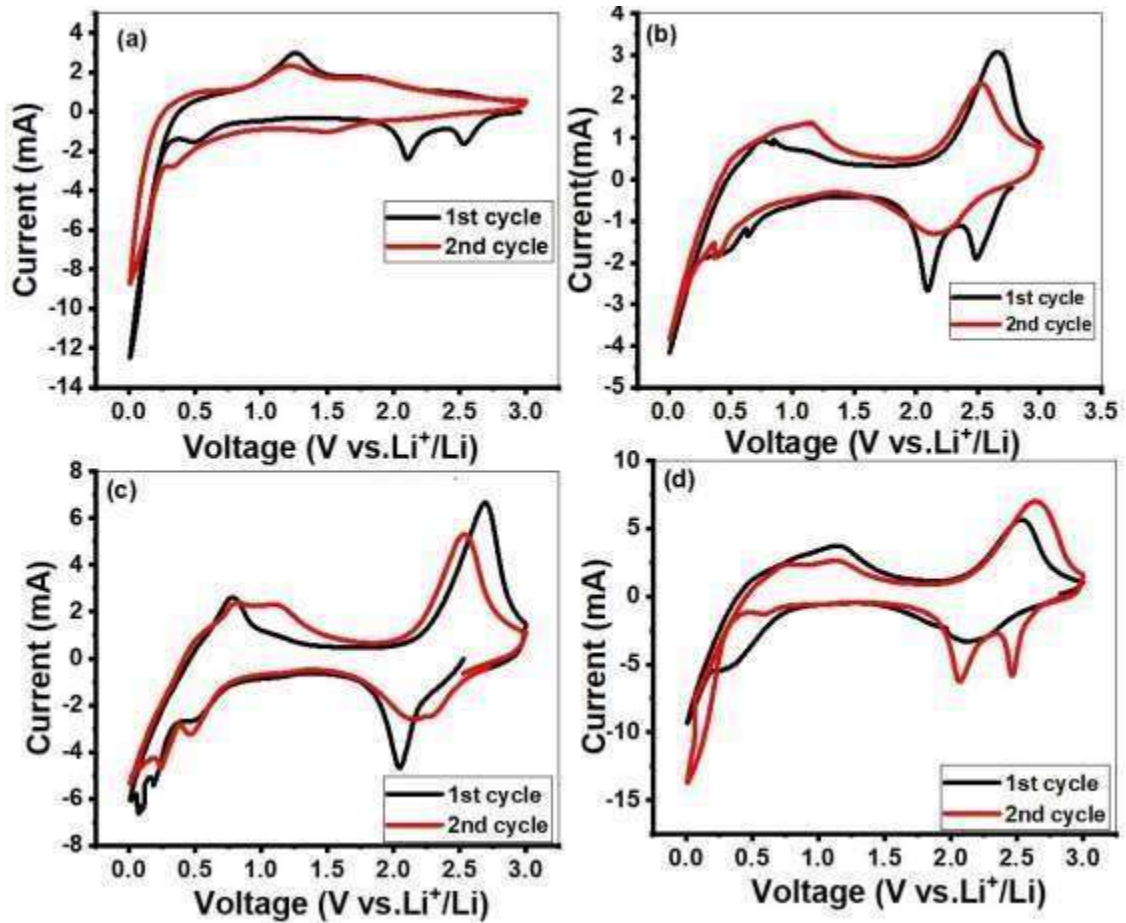
Figure 3.26 Cyclic voltammograms curves of all nanocomposites

The change in shape of cathodic peak in the second cycle corresponds to structural change of material. When Lithium cation enters in structure it increases interlayer spacing, the repulsive forces of cation leads to cracking of MoO_3 and thus decrease the particle size. That's why peaks of MoO_3 changes in next cycles[67]. The overall discharge and charge process could be summarized by the Eqs. (1) and (2)[161].

Intercalation: $MoO_3 + xLi^+ + xe^- \rightarrow Li_xMoO_3$ (1)

Conversion: $LixMoO_3 + (6 - x) Li^+ + (6 - x) e^- \leftrightarrow Mo + 3Li_2O$ (2)
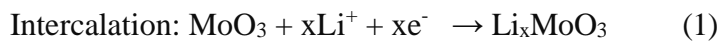
3.6.2 Galvanostatic charge/discharge measurements

Galvanostatic charge/discharge measurements were performed between a voltage window of 0.01-3V at a current density of $100mAg^{-1}$ as shown in Fig 3.27.
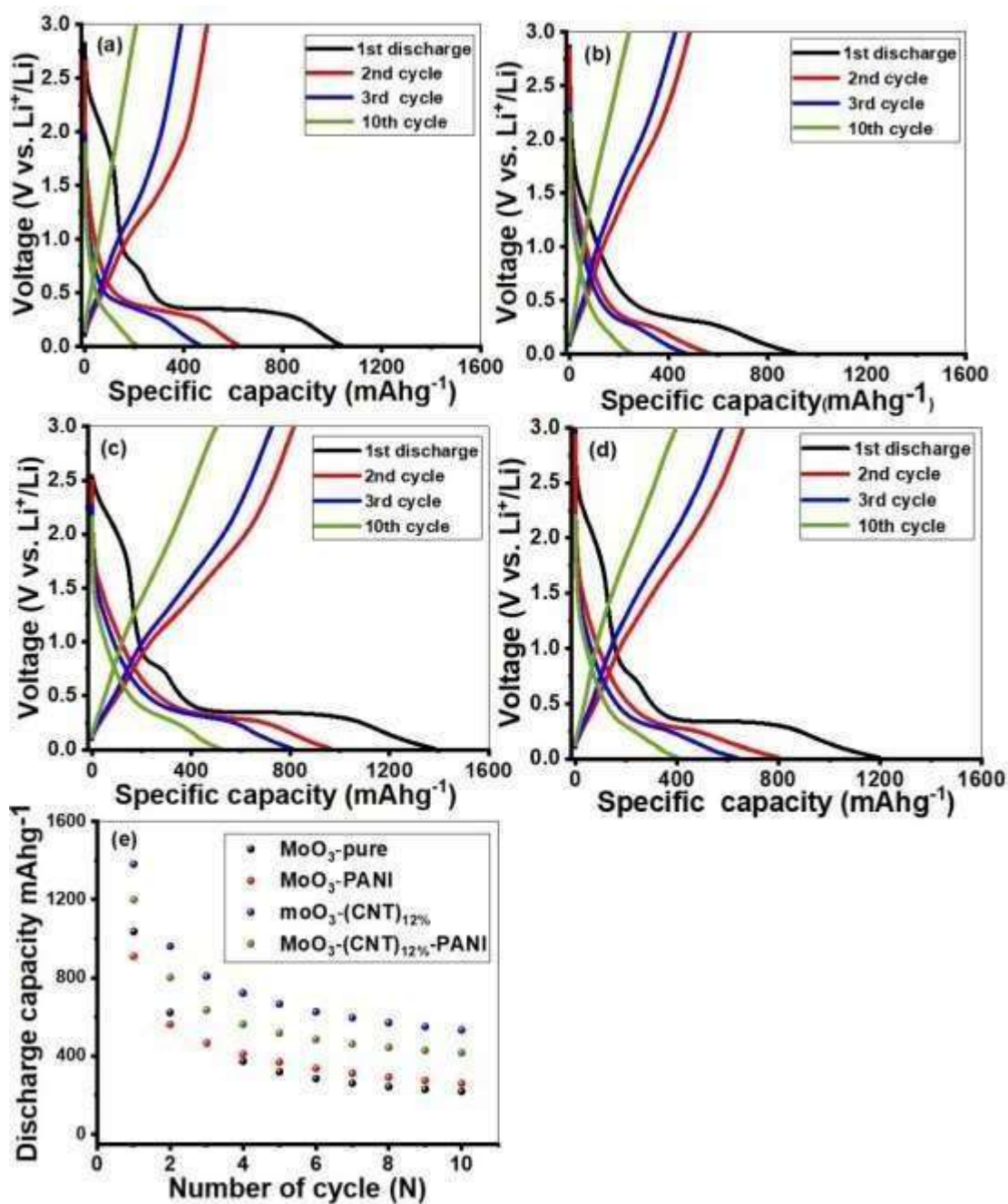
Figure 3.27 The charge/ discharge curves of (a) MoO_3 b) MoO_3-PANI c) MoO_3–
$(CNT_S)_{12\%}$ d) MoO_3-$(CNTs)_{12\%}$-PANI nanocomposite e) Cyclic performance of
all electrode all nanocomposites electrodes in the initial 10 cycles as a function
of capacity.
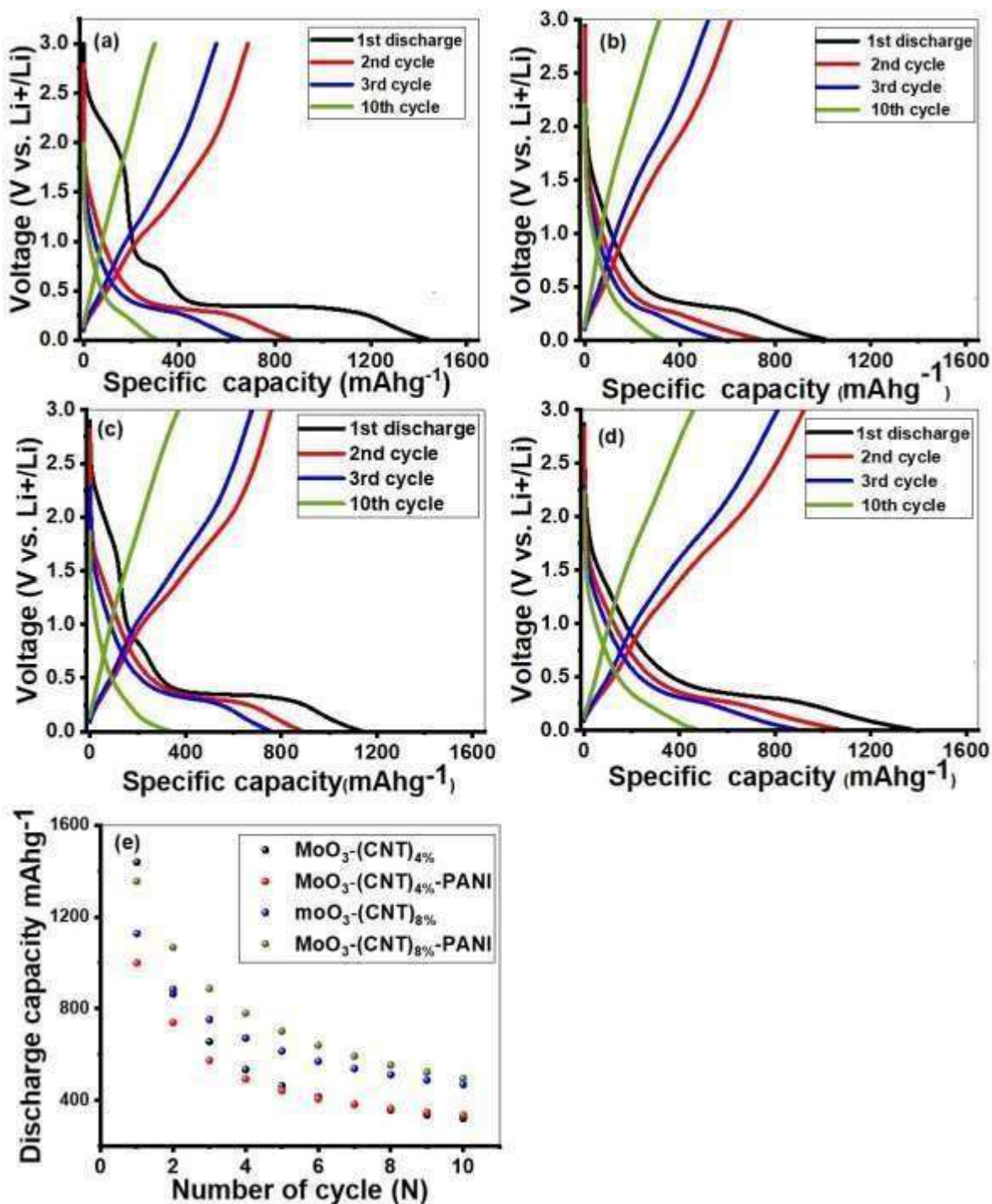
Figure 3.28 The charge/ discharge curves of nanocomposite.

The initial discharge capacities of MoO_3 pure, MoO_3 PANI, MoO_3-$(CNT)_{12\%}$ and MoO_3-$(CNT)_{12\%}$-PANI at 100 mAhg^{-1} are found to be 622.23, 561.75,961.5 and 801mAhg^{-1}, While charge capacities are 494.08, 485.01,814.04 and 801 mAhg^{-1}, the first coulombic efficiencies are 79.40,86.3,84.6 and 82.4%, respectively. All MoO_3 anodes lead to low coulombic efficiencies in first cycle, because of large irreversible capacities[67]. The large irreversible capacity arises owing to following reasons: Firstly,

90

the solid electrolyte interface (SEI) formation on the surface of nanoparticles. Secondly, decomposition of electrolyte owing to unsaturated carbon atoms. In addition, Li ions may be trapped in the cavities of nanocomposites due to slow release of Li kinetics, formation of lithium compounds or may be due to bonding between less coordinated atoms at defect sites[67, 162]. From the second discharge onwards, the discharge/charge curves are well coincided. All uncoated samples almost show similar behavior showing variations only in the extent to which these materials can store capacity and further how much capacity is retained upon cycling. The first discharge profile shows a rapid potential drop from 3V until it reaches a narrow plateau around 2.3V which is due to intercalation of Lithium ions in to crystal structure of active material followed by a wide plateau at a potential of 0.8V which corresponds to conversion reaction between lithium ions and molybdenum oxide. Moreover, a steep profile follows this narrow plateau which tappers off gradually until potential reaches to 0.01V and shows the formation of SEI. The following 2nd discharge curve undergo changes due to Li^+ driven structural changes and therefore does not show any narrow plateau at potential lower than 2.3V followed by reduction in the wide plateau and steep profile. Information regarding with other compositions of α- MoO_3 are shown in Fig 3.28.

3.6.3 Rate capability

Figure 3.29 Investigate specific capacity, rate performance and cyclic stability of MoO_3 pure, MoO_3-$(CNT)_{x\%}$ and MoO_3-$(CNT)_{x\%}$-PANI electrode at various rates, such as $50mAg^{-1}$, $100mAg^{-1}$, $200mAg^{-1}$ and $400mAg^{-1}$ for 35 cycles. The charge/discharge capacities of Mo-$(CNT)_{12\%}$ is 814.5/961.5, 433.8/484.93, 293.93/330.04 and Mo-CNT)$_{12\%}$-PANI nanocomposites are 660/801, 347/390.75, 247.5/286.9mAg^{-1} at the current density of 100,200 and 400mAg-^{1}, While pure MoO_3 possess charge discharge capacities of 494.08/622.23, 160.2/181.4 and 104.1/119.7 at the same current rate.
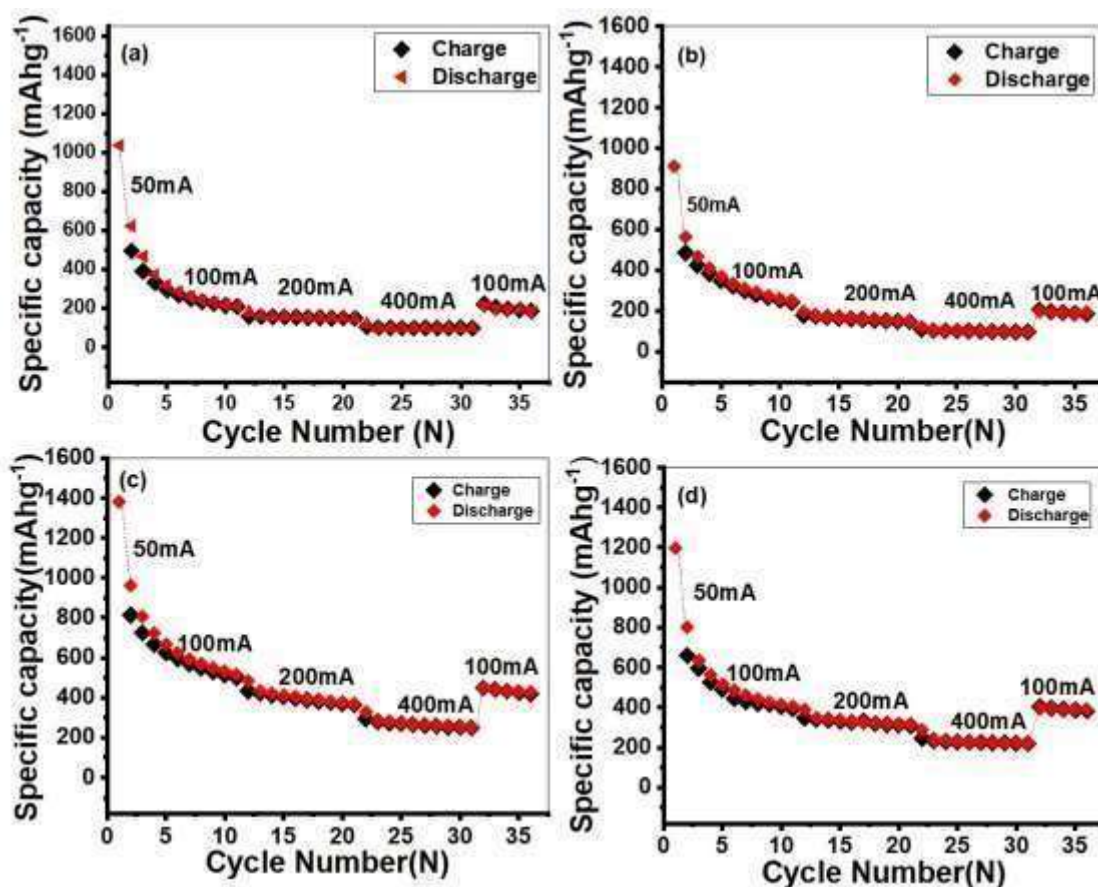
Figure 3.29 The cyclic performance of a) MoO_3 b) MoO_3-PANI c) MoO_3–$(CNT_S)_{12\%}$ d) MoO_3-$(CNTs)_{12\%}$-PANI nanocomposite nanocomposites at various current rates.

The graph showing decrease in capacity with increase of current density, however when current density reduces back to $100mAg^{-1}$, a charge /discharge capacity of 449.93/450.96 and 211/221 in case of MoO_3-$(CNT)_{12\%}$ and pure MoO_3 was obtained and remain stable in the subsequent cycles. PANI occupied some spaces in nanoparticles which increase reversibility and cyclic stability owing to the increasing extraction /insertion of Li^+ ion. Carbon nanotubes also improve performance of composites because of its conductivity, it also prevent electrode from disintegration during charge and discharge.
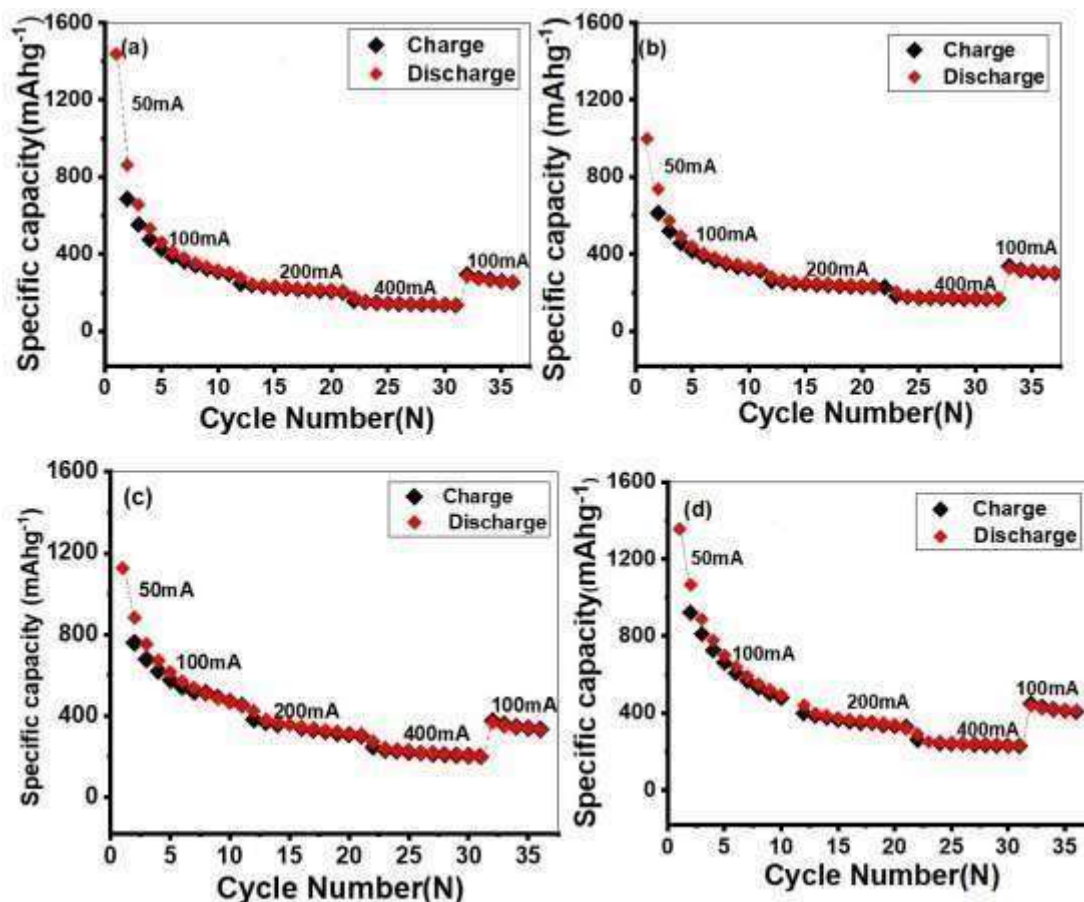
Figure 3.30 The cyclic performance of (a) MoO_3-pure, b) MoO_3-PANI. (c) MoO_3-$(CNT)_{12\%}$. (d) MoO_3-$(CNT)_{12\%}$-PANI nanocomposite nanocomposites at various current rates.

Apart from these carbon nanotubes are active itself electrochemically, prevent electrode disintegration by providing a mechanical framework during charge and discharge. On the other hand, carbon nanotubes provide physical barrier to prevent MoO_3 nanoparticles from aggregation and improve structure integrity[163]. Moreover, during cycling it act as a buffer that accommodate volume changes and thereby maintain structural stability. Specific capacity decreases drastically by increasing cycle number owing to volumetric changes that result in decrease in crystallinity. The stability results of MoO_3-CNT) $_{12\%}$ are better as compared to MoO_3-$(CNT)_{12\%}$-PANI.

Table 3.2 Specific capacities and cycle performance of MoO$_3$-based anodes in LIBs as reported in the literature

Samples	Dicharge capacity	Reversible capacity	Current density	References
MoO$_3$-(CNT)$_{12\%}$-PANI	801	406	100mAg^{-1}	This Work
MoO$_3$-(CNT)$_{12\%}$	961	516.99	100mAg^{-1}	This work
α-MoO$_3$	301	180	30 mAg^{-1}	[69]
α-MoO$_3$	211	133	300 mAg^{-1}	[69]
MoO$_3$	668	157	200 mAg^{-1}	[68]
MoO$_3$	974	286	100 mAg^{-1}	[164]
MoO$_3$-NiMoO$_4$	1031	324	100 mAg^{-1}	[164]
α-MoO$_3$-CNT	583	194	500mAg^{-1}	[123]

MoO$_3$ –(RGO)$_{12\%}$-PANI showed discharged capacity of 1027.6 mAhg^{-1} at 100 mAg^{-1} and 656.8 mAhg^{-1} at 400 mAg^{-1} after 30 cycles as shown in Fig 3.31.
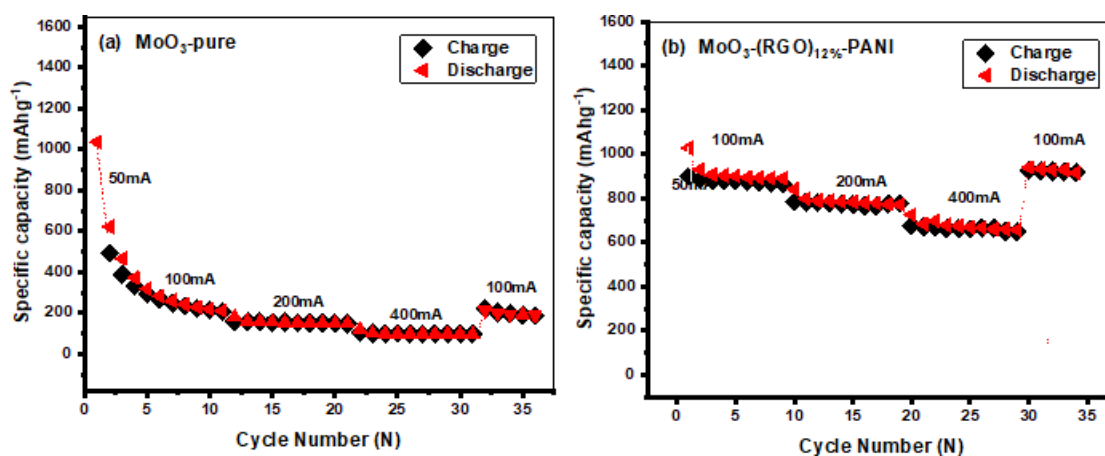
Figure 3.31 The cyclic performance of (a) MoO$_3$-pure, b) MoO$_3$-(RGO)$_{12\%}$-PANI

3.6.4 Electrochemical impedance spectroscopy (EIS)

The Nyquist plots of the EIS spectra Z" (ohm) and Z' (ohm) represent imaginary and real impedance components in the Nyquist plots. To evaluate the kinetics of anode and

cathode electrodes and to provide information about the bulk resistance of the electrode, surface film and charge transfer, we measured the electrochemical impedance spectroscopy (EIS) of the MoO_3-pure, MoO_3-PANI, MoO_3-$(CNT)_{12\%}$ and MoO_3-$(CNT)_{12\%}$-PANI nanocomposite electrodes. An equivalent circuit was employed to model the circuit parameters corresponding to the EIS of the cell. The electrochemical impedance spectra (EIS) of nanocomposites were recorded at an open circuit potential (OCP) as shown in Fig 3.32. Here R_1 connected in series represents the solution resistance, and the two parallel circuits consisting of constant phase elements (CPEs) and resistance (R) represent the capacitive and resistive load in the cell. R_2 and CPE_2 denote the resistance and constant phase element of the semicircle obtained at the high frequency region, while R_3 and CPE_3 are for the semicircle obtained at the low frequency region.
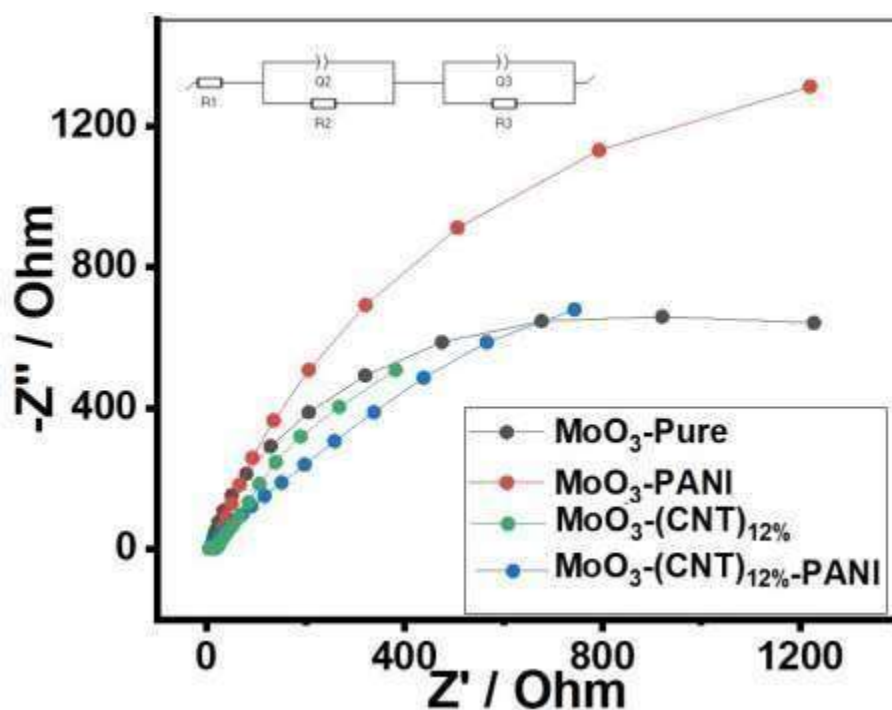
Figure 3.32 Electrochemical impedance spectra of MoO_3 electrodes.

According to the literature, the small semicircle in the high frequency region signifies interfacial layers, where Li^+ ions migrate through surface films on the electrode encounter resistance. The larger semicircle represents charge transfer resistance and double layer capacitance at the low frequency range. The semicircles, however, are generally depressed and a true capacitor cannot fit well with the experimental data. The CPEs are generally used in place of a capacitor to obtain a better mathematical fit, but

their physical justification is not obvious. Heterogeneities in the electrodes, such as surface roughness and porosity, were generally attributed with this observation[165, 166]. Physical interpretation of Q and α values in CPE is not straightforward and has no clear physical correspondence. Only alpha (α) can provide a measure of how similar the CPE is to an ideal capacitor. In addition, alpha being close to 0.5 was attributed to the behavior of a porous electrode, whereas for an ideal flat electrode, it is unity. Beyond these, Q and α hardly provide any physical insight and were not analyzed in detail [167].The experimental data (symbols) and the simulated (solid line) data according to the electrical equivalent circuit in the inset of figure are collected in Table 3.3. At the electrode–electrolyte boundary, there was kinetic resistance offered owing to the charge transfer. MoO_3-$(CNT)_{12\%}$ showed small resistance due to the electric conductivity offered by CNTs and the small contact resistance of the active material and current collector [66].
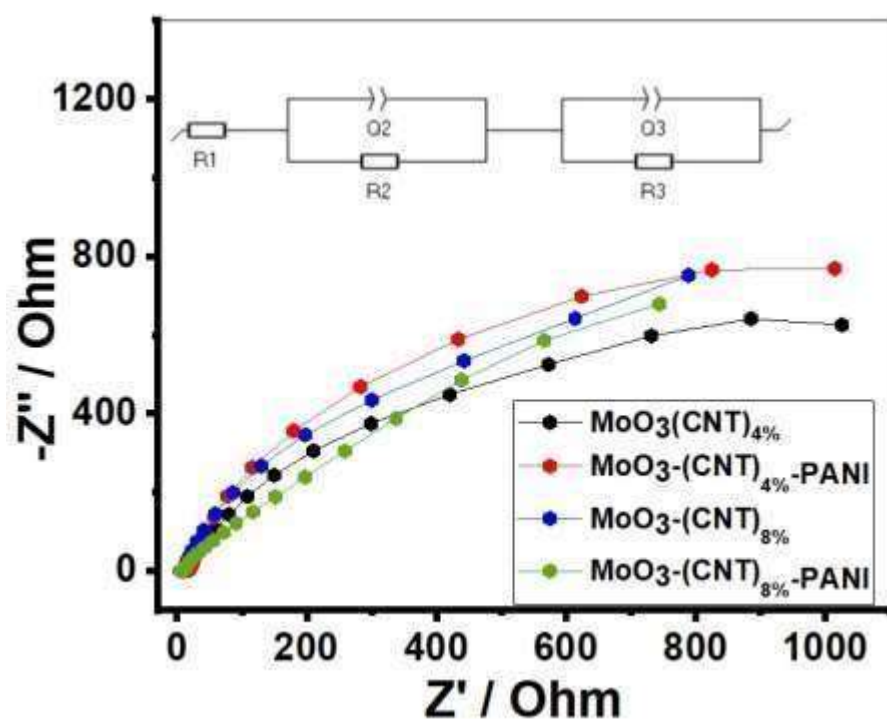
Figure 3.33 Electrochemical impedance spectra of MoO_3 electrodes

Table 3.3 EIS fitting results of samples.

Samples	$R_1(\Omega)$	$R_2(\Omega)$	$R_3(\Omega)$
MoO_3	7.11	9.923	1208
MoO_3-PANI	2.665	20.1	1201

MoO₃-(CNT)₄%	3.726	15.68	1007
MoO₃-(CNT)₄%-PANI	3.674	14.77	871
MoO₃-(CNT)₈%	4.072	9.923	739
MoO₃-(CNT)₈%-PANI	5.279	13.92	783
MoO₃-(CNT)₁₂%	3.072	22.2	339
MoO₃-(CNT)₁₂%-PANI	5.169	45.4	696.7

3.7 WO$_3$ as Anode Materials for LIBs

Tungsten trioxide (WO$_3$) compounds are ideal for LIB anodes due to their high theoretical capacity (693 mAhg^{-1}), low cost, efficient volumetric capacity (5274 mAhcm^{-3}), natural abundance, and diverse oxidation state numbers, resulting in more active electrochemical sites. Among polymorphous WO$_3$, the monoclinic form is attractive for LIB anodes due to its superior crystal structure and tungsten oxidation state. Despite its poor electrical conductivity, slow lithium intercalation/de-intercalation kinetics, and fast volume expansion/contraction over repeating cycles, mWO$_3$ has low-rate performance and high-capacity degradation. That's why, improvements were made.

3.8 Physicochemical Measurements

The crystals structure of WO$_3$ nanocomposites were determined by the Powder X-ray diffraction (PXRD) using Cu Kα radiation (λ = 1.5417 Å) as represented in Fig 3.34. All the XRD peaks of the nanocomposites are well matched to the monoclinic phase of WO$_3$ (JCPDS 83-0950) with the lattice constants of a = 7.300, b = 7.538, and c = 7.689 Å, which confirms preparation of WO$_3$. No other diffraction peaks of impurities are found, which indicates the formation of pure WO$_3$ of the final product. The high intensities of the diffraction peaks is an indication of good crystallinity of the samples. The MWCNT$_S$ peaks were not observed during the compositing of WO$_3$ with MWCNTs, because the peaks in the nanocomposites are overlapped with peaks of the WO$_3$ nanoparticles.
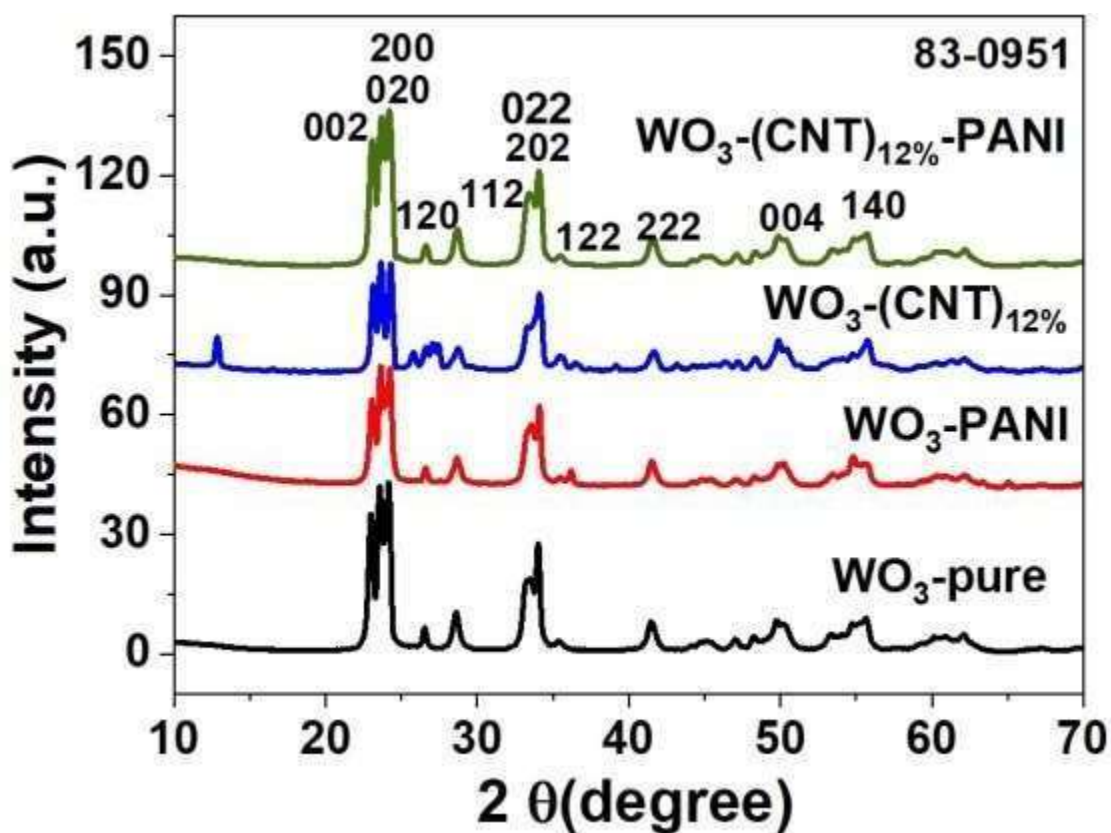
Figure 3.34 XRD spectra of WO_3, WO_3-PANI, WO_3-(CNTs)$_{12\%}$ and WO_3-(CNT)$_{12\%}$-PANI

The crystals structure of WO_3 nanocomposites were determined by the Powder X-ray diffraction (PXRD) using Cu Kα radiation ($\lambda = 1.5417$ Å) as represented in Fig 3.35. All the XRD peaks of the nanocomposites are well matched to the monoclinic phase of WO_3 (JCPDS 83-0950) with the lattice constants of a = 7.300, b = 7.538, and c = 7.689 Å, which confirms preparation of WO_3. No other diffraction peaks of impurities are found, which indicates the formation of pure WO_3 of the final product. The high intensities of the diffraction peaks is an indication of good crystallinity of the samples. The RGO peaks were not clearly observed during the compositing of WO_3 with RGO, because the peaks in the nanocomposites are overlapped with peaks of the WO_3 nanoparticles[168].
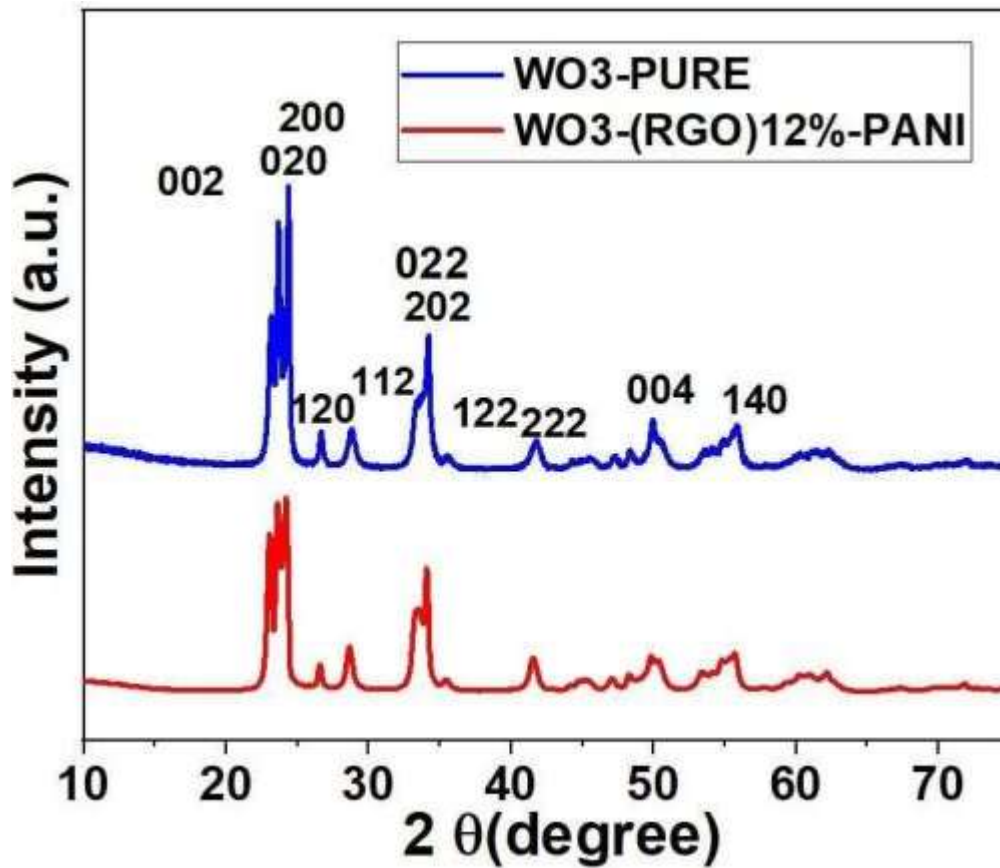
Figure 3.35 XRD of nanocomposites

3.8.1 Morphological analysis

The surface morphologies of the WO$_3$ nanocomposites were investigated by SEM. Fig

3.36 exhibit typical FESEM of all nanocomposite, which consist of uniform nanoflakes

like morphology.
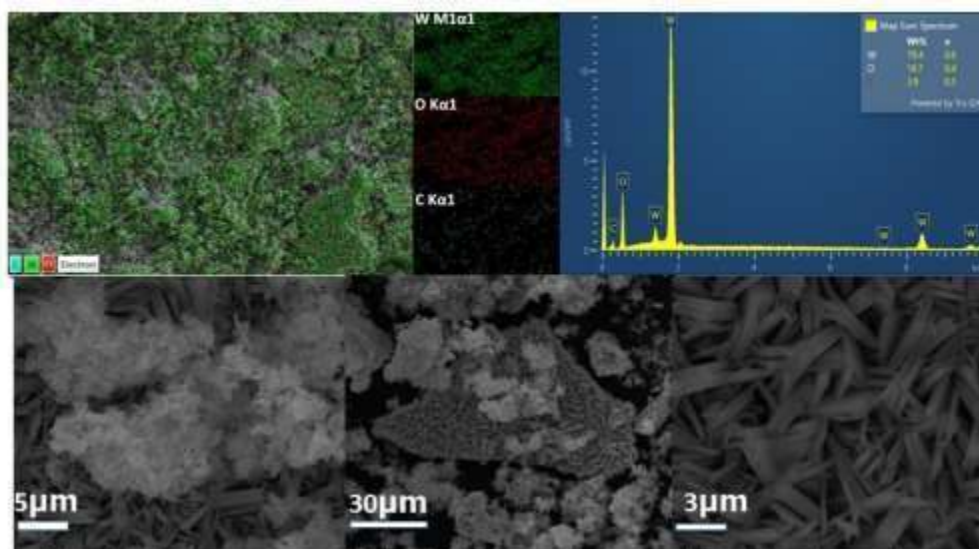
Figure 3.36 FESEM images and EDX mapping WO$_3$ pure

However, WO$_3$ nanoflakes are interconnected by each other and organized into a 3D porous network, confirming structure stability, high surface area as well as shortened lithium ion diffusion pathway[169]
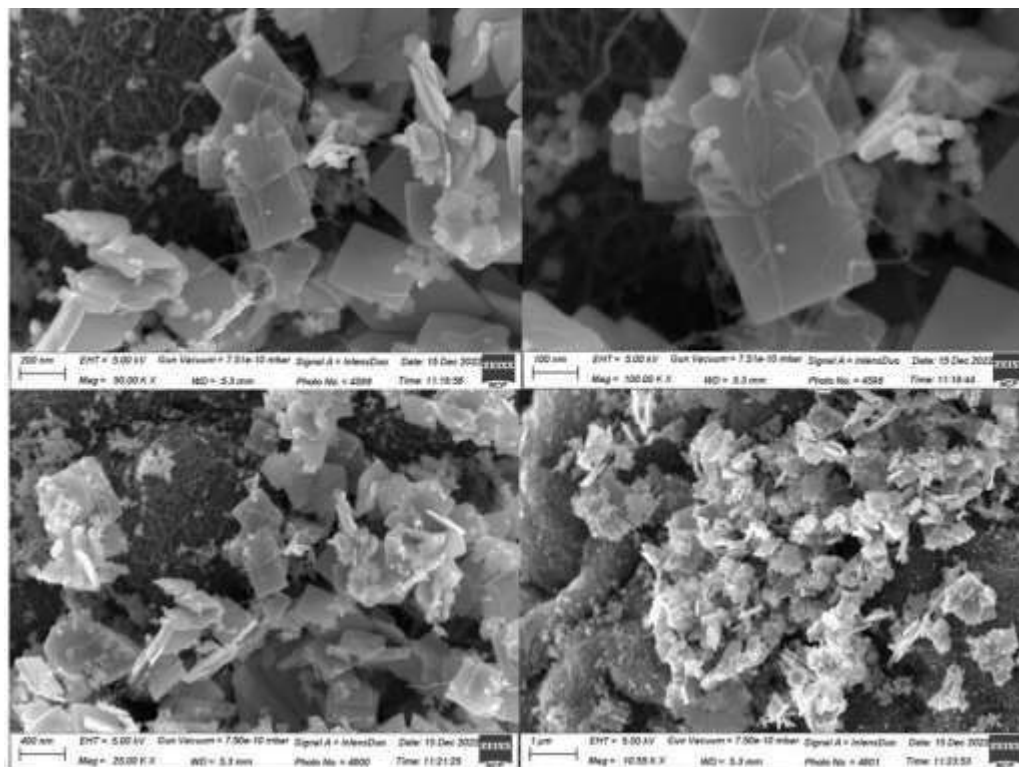
Figure 3.37 FESEM images of WO$_3$-CNTs (12%)

Fig 3.37 demonstrates that the WO$_3$ surface is covered with MWCNTs, which exhibits a uniform size and thin petals. After the addition of MWCNTs rough surface was observed suggesting high dispersion of MWCNTs. The EDS mapping exhibits existence of W, O and are homogeneously distributed.

The surface morphologies of the WO$_3$ nanocomposites were investigated by SEM. Fig 3.38 exhibit typical FESEM of all nanocomposite, which are composed of uniform nanoflakes like morphology. However, WO$_3$ nanoflakes are interconnected by each other an organized into a 3D porous network, confirming structure stability, high surface area as well as shortened lithium-ion diffusion pathway.
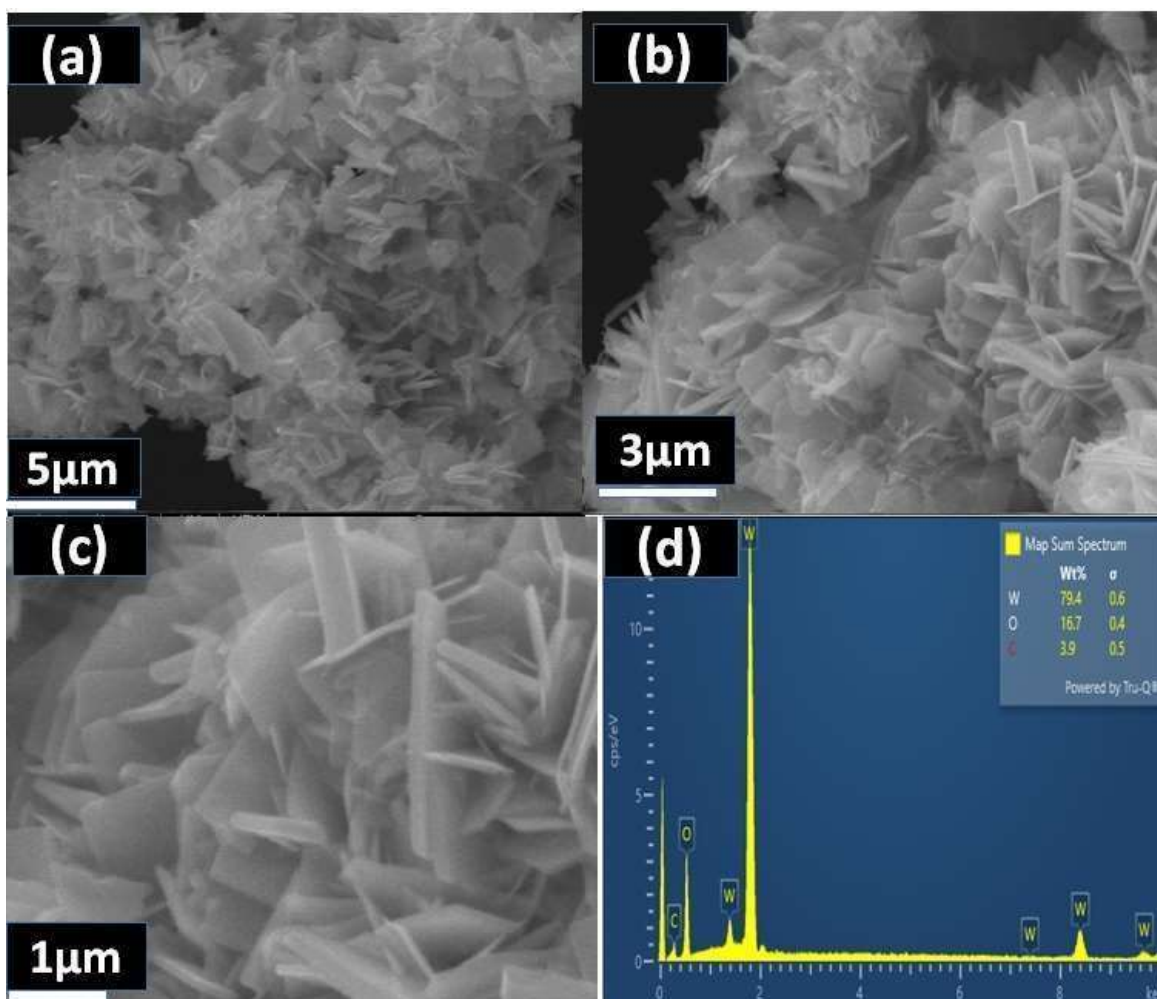
Figure 3.38 FESEM images and EDX mapping WO₃ pure

3.8.2 XPS analysis

XPS analysis was performed to determine the oxidation state and chemical composition of WO_3-$(CNT)_{12\%}$-PANI nanocomposite.

The results revealed the presence of W, O, C and N elements. Fig 3.39 depicts the presence of carbon spectra, which is due to presence of CNTs. The peaks at 284.3 and 285.0 are due to C-O and C=O respectively, while the peaks at 35.2eV and 37.3eV have been ascribed to binding energies of $W4f^{7//2}$ and $W4f^{5/2}$ and peak at 40.9 is attributed to W5p. These peaks confirmed W^{+6} oxidation state of tungsten in synthesized sample[170, 171]. It was observed that peaks with binding energies between 35.5-35.8 eV and 37.6-37.9eV mainly signify spin -orbit splitting peaks of $W4f^{7/2}$ and $W4f^{5/2}$ respectively[172] The O1s spectra showed lattice oxygen (O_L) and oxygen vacancies (Ov) with their corresponding binding energies[172].
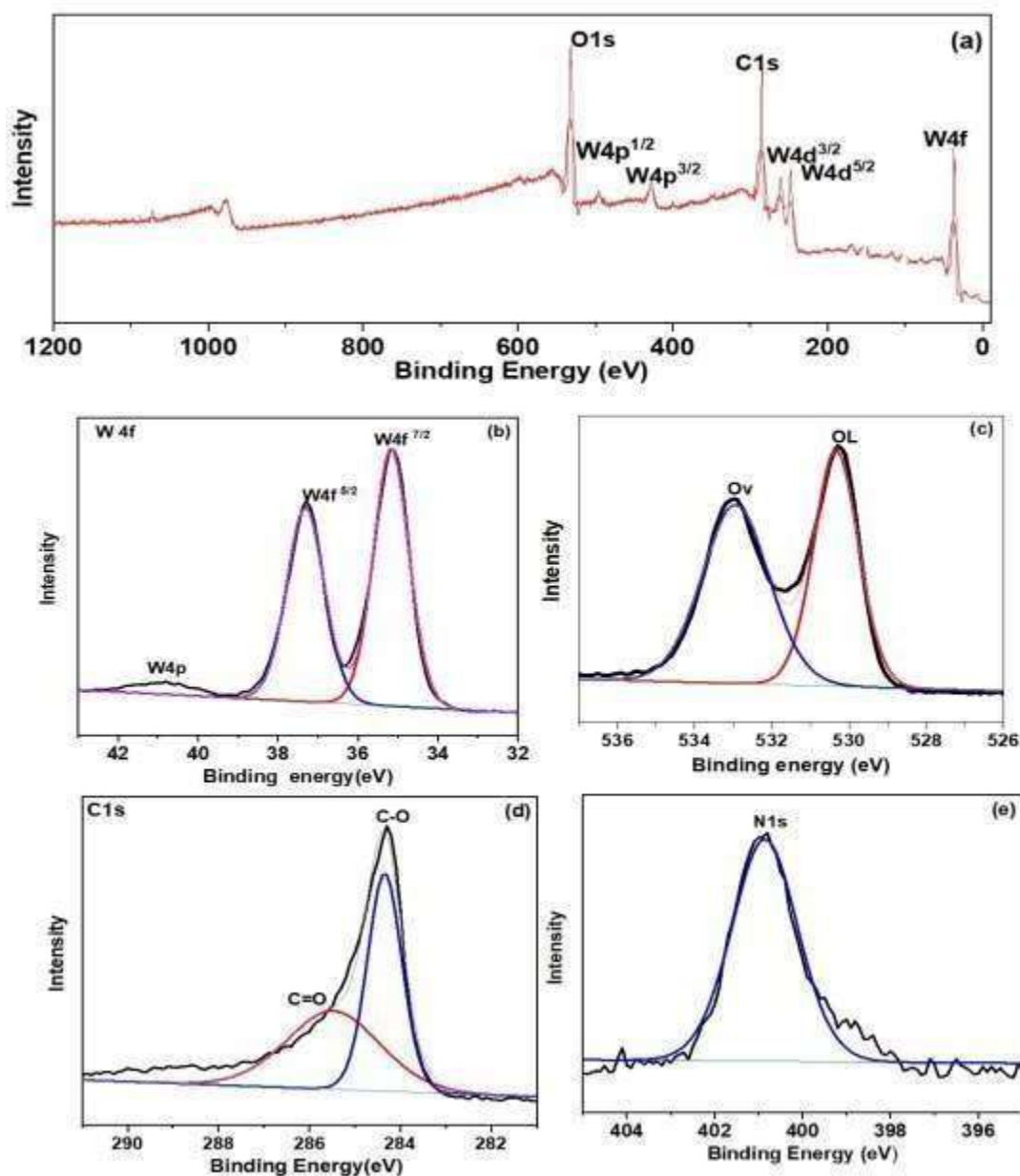
Figure 3.39 (a) XPS full survey scan of WO_3-CNTs $_{(12\%)}$-PANI, (b) W4f, (c) O 1s (d) C1s (e) N1s

3.8.3 Functional group analysis

The FT-IR analysis was performed to further ascertain and confirm the composition of as-synthesized sample pure WO_3 as represented in Fig 3.40. The apparent absorption bands at low-frequency region (500 to $1000 cm^{-1}$) indicate vibration of the W-O-W in oxide[173].
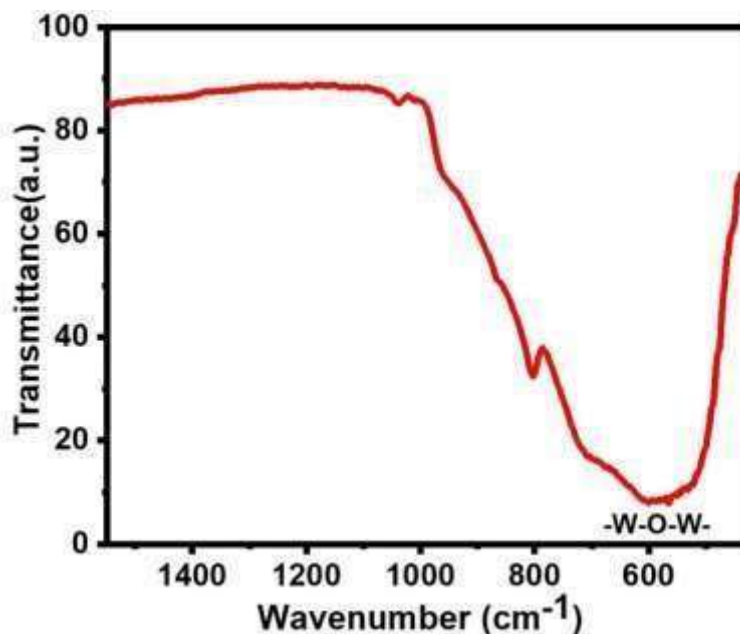
Figure 3.40 (a) FTIR analysis of WO_3-Pure.

3.9 Electrochemical Measurements

The cyclic voltammetry was conducted to study the detailed electrochemical behavior and reversibility of electrodes for the initial three cycles at scan rate of 0.5mV/s over the potential range of 0.01 to 3.0V (vs. Li/Li^+) as shown in Fig. 3.41(a-d). For the first cycle of electrodes, strong cathodic peak was observed near 0.6 V, which disappeared in the following 2nd and 3rd cycles.

3.9.1 Cyclic voltammetry (CV)

The strong peak near 0.6V is attributed to formation of Li_2O and solid electrolyte interphase (SEI) layer formation ($WO_3 + xLi^+ \leftrightarrow Li_xWO_3$; $LixWO_3 + (6 − x) Li^+ + (6 − x) e^- \leftrightarrow W + 3Li_2O$).
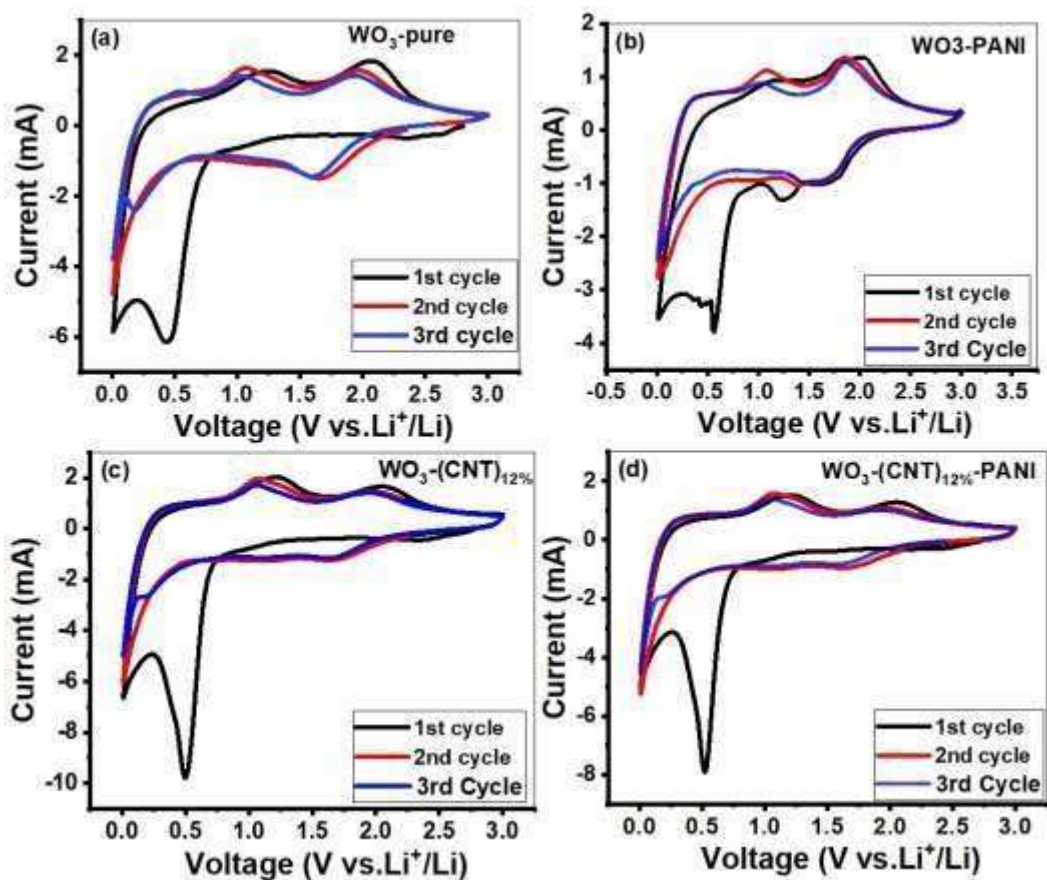
Figure 3.41 shows CVs of WO$_3$ bulk, WO$_3$ PANI, WO$_3$-(CNT)$_{12\%}$ and WO$_3$-(CNT)$_{12\%}$-PANI at a scan rate of 0.5 mV s^{-1} in the range between 0 and 3.0 V vs Li/Li$^+$.

According to literature, the thermodynamic potential of reaction in case of WO$_3$ is 1.6V, which indicates that the observed overpotential between 0.6 and 1.6 corresponds to decomposition of WO$_3$ to produce non crystalline Li$_2$O phase and W metal[174, 175]. In the anodic polarization, two oxidation peaks were observed at 1.2 V and 2.1 V, indicating W metal oxidizes to W^{+6} in WO$_3$. (W + 3Li$_2$O → WO$_3$ + 6Li$^+$ + 6e$^-$). CV profiles almost remain steady for second and third cycle, indicating good stability and high reversibility in the charging/discharging process. However, the peaks current intensity decreased in the next cycles, indicating capacity loss during first cycle, which may be due to formation of SEI film and decomposition of electrolyte.
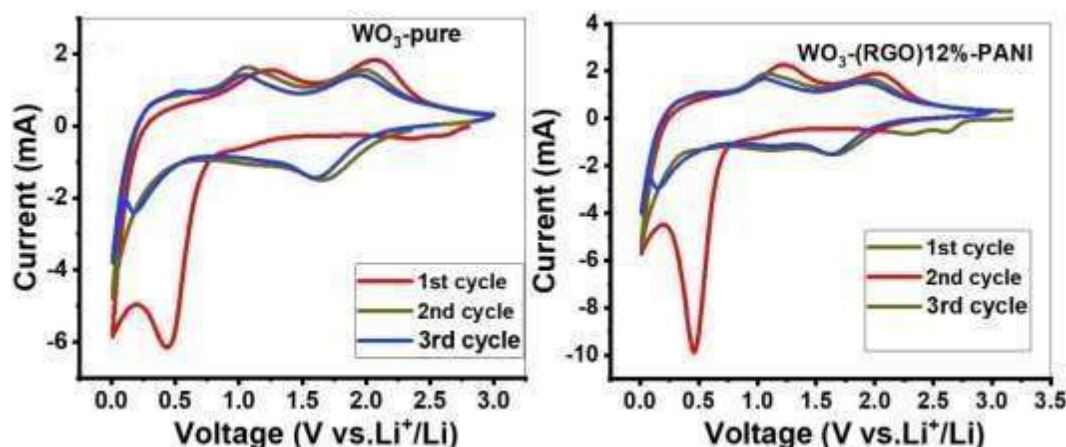
Figure 3.42 CVs of WO$_3$ bulk and WO$_3$-(RGO)$_{12\%}$-PANI at a scan rate of 0.5 mV s^{-1} in the range between 0 and 3.0 V vs Li/Li$^+$.

Electrochemical tests were performed in the voltage range of 0.01–3.0 V vs Li/Li$^+$ to investigate the cyclic performance and rate capability of WO$_3$ and WO$_3$-(RGO)$_{12\%}$-PANI anodes. The cyclic voltammetry (CV) results of two anodes for first 3 cycles are shown in Fig 3.42. During the initial charge process of WO$_3$ electrode, fist cathodic peak was observed at 0.6eV. The peak located at this potential was absent in the 2nd and 3rd cycles, which could be related to to solid electrolyte interphase (SEI) formation and reduction of Li$_2$WO$_x$ [175-177] (Li$_2$WO$_x$+(2x − 2)Li$^+$ +(2x − 2)e− →W+xLi$_2$O)[122, 175, 178]. It was observed in previous studies that the SEI film initially formed during first cycle on the surface of WO$_3$ appears as the intense peak as shown in the figure[179]. However, in the next cycle, WO$_3$ exhibit a weak reduction peak at this potential, indicating that the mesoporous structure of nanoparticles can inhibit the formation of SEI film or control severe structural change in the crystal. The sharp peak at 0.01 V arises from the reduction of W^{6+} or W^{5+} to W^0 according to the conversion reaction (W + 2xLi$^+$ 2xe$^-$ → W + xLi$_2$O). In the following process, broad anodic peaks were observed at 1.2 V and 2.1 V, indicating W metal oxidizes to W^{+6} in WO$_3$. (W + xLi$_2$O → WO$_x$ + 2xLi$^+$ + 2xe$^-$). For the next 2nd and 3rd cycles, the cathodic reduction peak of 0.01 V and two oxidation peak are repetitively appeared demonstrating the reversible conversion reaction of Li$^+$ intercalation/ de-intercalation to the WOx crystal structure[180].

3.9.2 Galvanostatic charge-discharge profiles

Fig 3.43 exhibited the galvanostatic charge-discharge profiles for Ist, 2nd and 10th cycle at current density of 100mAg^{-1} with a voltage range of 0.01-3.0 V.
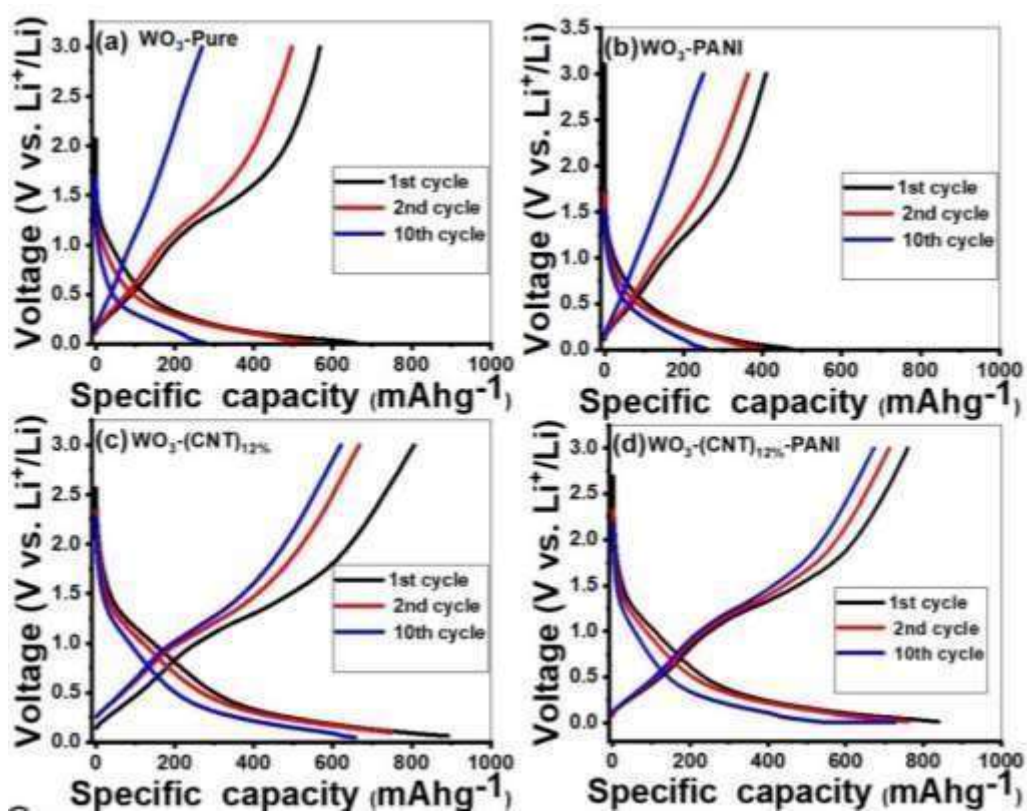
Figure 3.43 Charge/discharge profiles for (a) WO_3 b) WO_3-PANI c) WO3–
(CNTS)$_{12\%}$ d) WO_3-(CNTS)$_{12\%}$-PANI nanocomposites

Two voltage plateaus at about 1.6V and 0.6V were observed in the discharge curve as noticed in cathodic region of cyclic voltammogram (CV).

It can be seen that the WO_3-pure, WO_3-PANI, WO_3-(CNT)$_{12\%}$ and WO_3-(CNT)$_{12\%}$-PANI delivers a charge/discharge capacity of 567.357/661.24 mAhg^{-1},408.13/472.39 mAhg^{-1}, 805.52/891.01 mAhg^{-1} and 760.31/840.98 mAhg^{-1}, exhibiting coulombic efficiency of 85.80% ,86.39%, 90.63% and 90.40%, respectively. In the first cycle, high initial discharge capacity was observed, which could be attributed to the formation of SEI and decomposition of electrolyte[121]. The voltage plateau at 1.6V for discharging curves was well matches with the CV curves and is associated with the Li$^+$ ion insertion. It was observed that the WO_3-(CNT)$_{12\%}$ and WO_3-(CNT)$_{12\%}$-PANI showed much improved discharge capacity with respect to WO_3 pure and WO_3 PANI. The results show that the WO_3-(CNT)$_{12\%}$-PANI electrode exhibits enhanced discharge capacity of 728.48 mAh g^{-1} at the end of 10 th cycle and remains 537 mAh g^{-1} after 30 cycles, which are higher than pure WO_3 electrode 258.3 mAh g^{-1} after 10 cycles and 77.4 mAh g^{-1} after 30 cycles, respectively. The increased specific capacity may be due to MWCNTs and PANI coating. MWCNTs forms entangled structure with particles, facilitate motion of electrons between particles and provide short path for electron

transport hence provide conductivity around $(1-4) \times 102$ and 5–25 S cm^{-1} along transverse and longitudinal axes, respectively[181]. Moreover, PANI coating provide high surface area, good rate performance, and good cycle stability. Polyaniline percolate easily in to carbon nanotubes and allow electrolyte to diffuse in to the electrode material and help to prevent volume variations occur during the discharging/charging[182].

Fig 3.44 shows the exhibited the galvanostatic charge-discharge profiles for Ist, 2nd and 10th cycle at current density of 100mAg^{-1} with a voltage range of 0.01-3.0 V. The plateau near 1.6 V was observed, indicating 1st discharge process where, Li$^+$ intercalate into the crystal structure of WOx. After first discharge potential drops slowly, which indicate of SEI layer formation. Finally, the WO$_3$ and WO$_3$-(RGO)$_{12\%}$-PANI electrodes exhibited the first charge and discharge capacities of 567.357/661.24 mAhg^{-1} and 1035/1188 mAh g^{-1} exhibiting coulombic efficiency of 85.80% and 87.12, respectively. The phenomenon that the capacity first increases and then decreases could be related to the formation of SEI layer and the improvement of Li$^+$ ion diffusion kinetics[183-185].
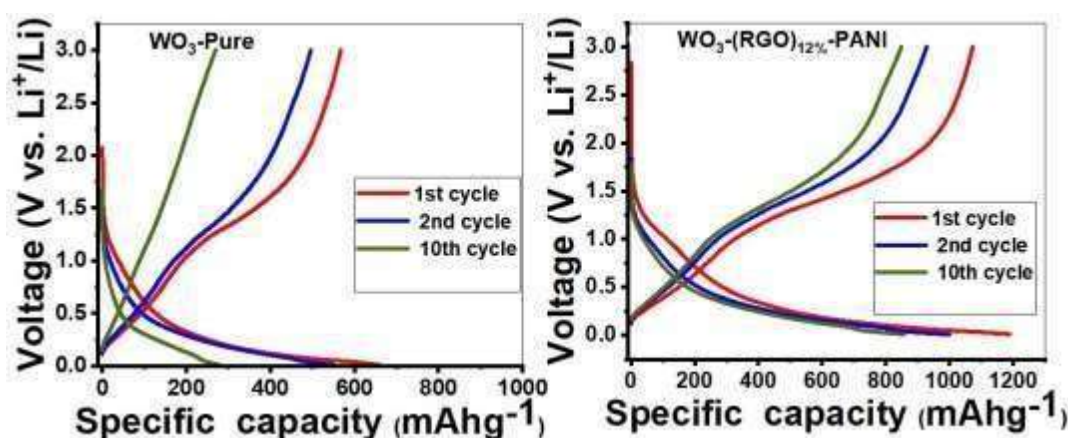
Figure 3.44 Charge/discharge profiles for WO$_3$ nanocomposites.

3.9.3 Rate capability

Fig 3.45 exhibited the rate capability of WO$_3$-pure, WO$_3$-PANI, WO$_3$-(CNT) $_{12\%}$ and WO$_3$-(CNT) $_{12\%}$-PANI measured at various charge/discharge current densities ranging from 100, 200 and 400 mAg^{-1} for each of ten cycles. It can be observed that the specific capacity decreases gradually as the current density increased. The discharge capacities of WO$_3$-(CNT) $_{12\%}$ were 891.81, 600.46 and 500.65 mAhg^{-1} and for WO$_3$-(CNT) $_{12\%}$-PANI were 840.98, 688.57 and 593.81 mAhg^{-1} at current densities of 100, 200 and 400mAg^{-1}, respectively; while WO$_3$ pure and WO$_3$-PANI possessed discharge capacities of 661.24, 218.36, and 112.55 and 472.39, 226.60 and 96.40. WO$_3$-(CNT)

12%-PANI exhibited superior rate performance, which were much higher than those of the pure WO$_3$ anode at the same current densities because of MWCNTs and PANI coating. MWCNTs maintains electrical conductive network, buffer the volume changes, improve the electronic conductivity and lithium-ion transport. Moreover, the MWCNTs improves the structural decency and robustness of the electrode Consequently, the electrical conductivity of WO$_3$-(MWCNTS)$_{12\%}$ nanocomposites was improved significantly through conductive networks that accomplished as current collectors to physically isolated and electrically inter-connected WO$_3$ nano- particles with conductive MWCNTs. PANI coating function as a protective layer to decrease the volume changes and facilitate formation of stable SEI layer. Furthermore, it shows coulombic efficiency of 91%, suggesting efficient ion and electron transport and facile lithium-ion extraction and insertion in the WO$_3$ nanocomposites. Moreover, compared with WO$_3$ pure, the WO$_3$-(MWCNT)$_{12\%}$-PANI composite showed good cyclic stability.
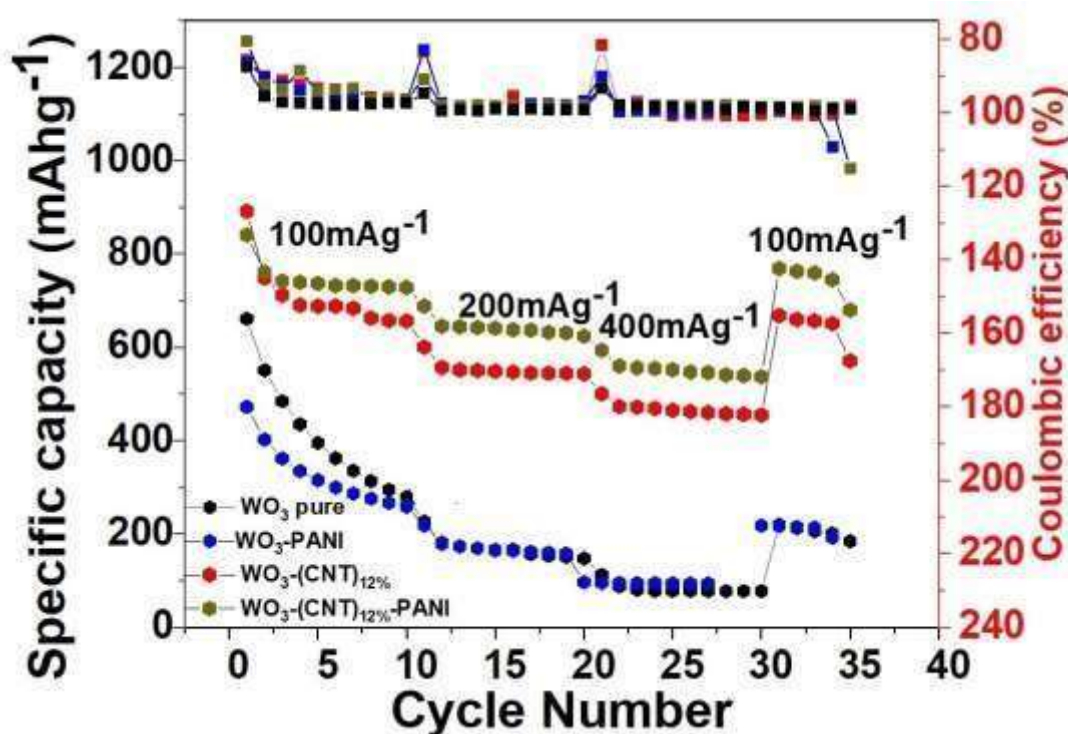
Figure 3.45 Rate capability for (a) WO$_3$ b) WO$_3$-PANI c) WO$_3$–(CNTS)$_{12\%}$ d) WO$_3$-(CNTS)$_{12\%}$-PANI nanocomposites.

Fig 3.46 exhibit the rate capability of WO$_3$-pure and WO$_3$-(RGO)$_{12\%}$-PANI measured at various charge/discharge current densities ranging from 100, 200 and 400 mAg^{-1} for each of ten cycles. The WO$_3$-(RGO)$_{12\%}$-PANI electrodes exhibited discharge capacities of 1188, 861.00, 770.23 mAhg^{-1} at the current densities of 100, 200 and 400mAg^{-1},

respectively. These results confirmed that the WO_3-$(RGO)_{12\%}$-PANI electrodes showed improved stability and capacity reversibility at different current densities than that of the pristineWO_3 electrode. The specific capacity of the WO_3-$(RGO)_{12\%}$-PANI electrode was measured as 770.23 mAhg^{-1} after 30 cycles, which is greater than greater than WO_3 electrode. Hence, it can be concluded that the interconnected 3D network of reduced graphene oxide maintains structural integrity, buffer the volume changes and stress for long cycles. In contrast, the specific capacity of pure WO_3 decreased owing to the pulverization arising from the sudden volume change during charge/discharge cycling or owing to a large amount of Li-ions insertion into the WO_3 crystal, which can block the Li$^+$ transfer from electrode to electrolyte. Thus, the WO_3-$(RGO)_{12\%}$-PANI exhibited higher and more stable lithium storage capability than pure WO_3 owing to the compositional and structural effect[122].
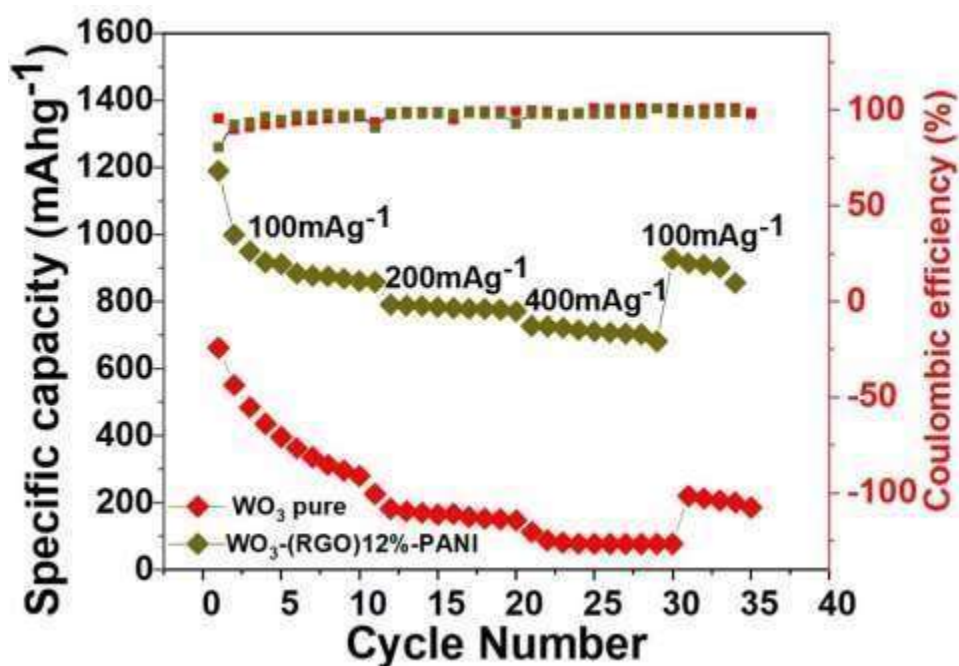
Figure 3.46 Rate capability of WO_3 nanocomposites.

3.9.4 Electrochemical impedance spectroscopy (EIS)

Electrochemical impedance spectroscopy (EIS) measurements of WO_3-pure, WO_3-PANI, WO_3-(CNT)$_{12\%}$ and WO_3-(CNT)$_{12\%}$-PANI nanocomposites were performed to better understand the charge transport mechanisms as shown in Fig 3.47. All the curves show similarity in appearance at low, high and medium frequency. At high to medium frequency a small semicircle is observed, while a straight line appears at the low frequency region. For LIBs, the charge transfer kinetics is evaluated from charge

transfer resistance. The diameter of semicircle represents charge transfer resistance. As it can be seen from the figure, the diameter of semicircle for WO_3-(CNT) $_{12\%}$-PANI nanocomposites is much smaller than WO_3-pure and WO_3-PANI. The EIS results are in accordance with charge/discharge, rate capability and cyclic voltammetry, demonstrating a favorable conducting network owing to WO_3 nanoparticles and the MWCNT$_S$.
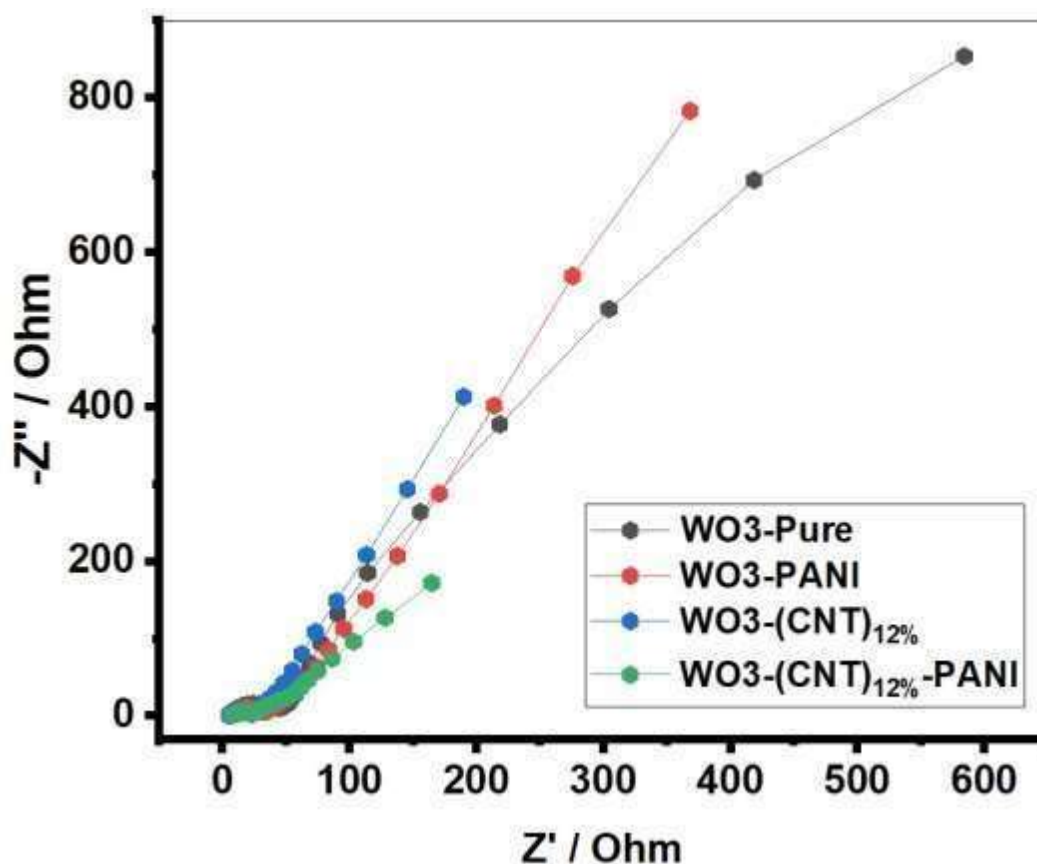
Figure 3.47 Nyquist plots of WO_3 nanocomposite electrodes**.**

Electrochemical impedance spectroscopy (EIS) measurements of WO_3-pureand WO_3-(RGO) $_{12\%}$-PANI nanocomposites were performed to better understand the charge transport mechanisms as shown in Fig 3.48. All the curves show similarity in appearance at low, high and medium frequency. At high to medium frequency a small semicircle is observed, while a straight line appears at the low frequency region. For LIBs, the charge transfer kinetics is evaluated from charge transfer resistance. The diameter of semicircle represents charge transfer resistance. As it can be seen from the figure, the diameter of semicircle for WO_3-(RGO)$_{12\%}$-PANI nanocomposites is much smaller than WO_3 pure. The EIS results are in accordance with charge/discharge, rate

capability and cyclic voltammetry, demonstrating a favorable conducting network owing to WO₃ nanoparticles and RGO.
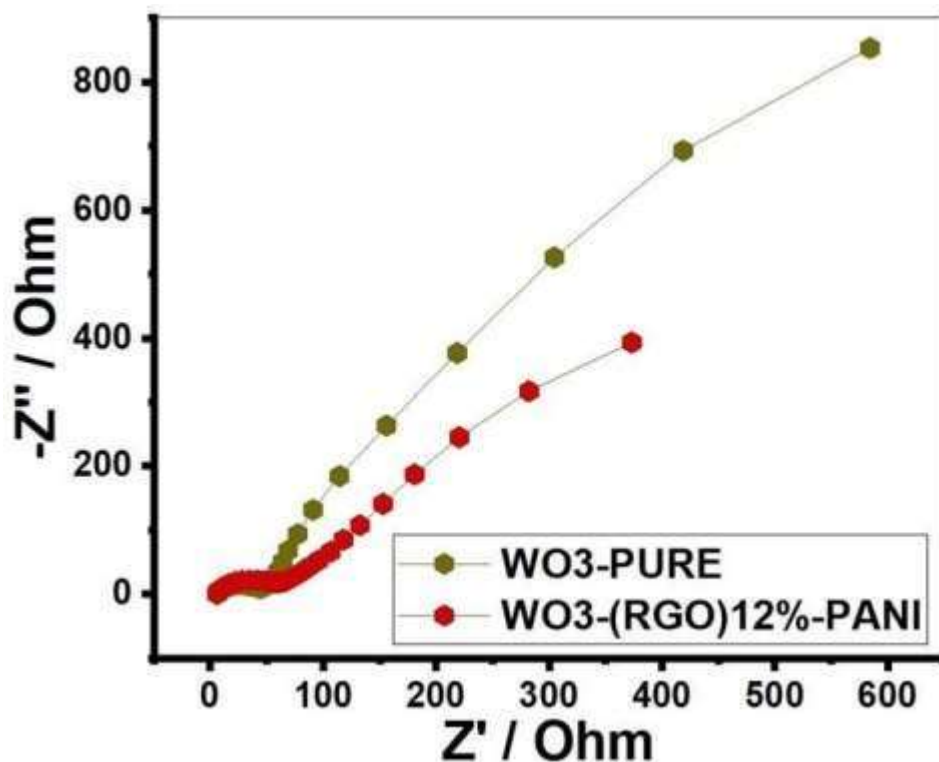
Figure 3.48 Nyquist plots of WO$_3$ nanocomposite electrodes

3.10 Comparative Analysis

Table 3.4 Comparative analysis of all samples

Electrode material	Initial cycle discharge (mAhg^{-1})	Reversible capacity(mAhg-1)	Current density(mAg⁻¹)	Capacity retention
Cr$_2$O$_3$ -(CNT)$_{12\%}$-PANI	1037	756	100	72%
MoO$_3$-(CNT)$_{12\%}$-PANI	801	406	100	50%
WO$_3$-(CNT)$_{12\%}$ -PANI	840	728	100	86%
WO$_3$-(RGO)$_{12\%}$-PANI	999	857	100	85%
Cr$_2$O$_3$-(RGO)$_{12\%}$-PANI	1027	789	100	77%

MoO$_3$-(RGO)$_{12\%}$-PANI	889	637	100	71%

Tungsten-based anode materials demonstrated the most promising outcomes in terms of capacity retention among these four types of materials..

3.11 Summary and Future Perspectives

Increasing global energy crisis and environmental concerns have stimulated development of energy-storage devices which are efficient and clean for society. Currently, Li-ion batteries exhibited their potential in the energy-storage devices, consequence of excellent charge–discharge capabilities, their great energy density and long cycling stabilities. TMOs electrodes got fast growth and explained its various potential in advancement of effective energy-storage systems owing to the excellent electrochemical performances and good physicochemical properties. However, their low electrical conductivity has retarded their good energy storage application. As a result, to solve this problem, many nanostructured TMOs and their composites with CNTs/RGO and PANI coating proved excellent electrochemical performances in rechargeable Li-ion batteries. We reported the development of hybrid nanostructured composites of $Cr_2O_3/MoO_3/WO_3$ with MWCNTs and RGO by co-precipitation method, Furthermore, PANI coating was done to increase their conductivity. The PANI coating layer alleviate volume changes, improve conductivity and cyclic stability.

The morphology and structure of nanocomposites were investigated by scanning electron microscopy (SEM) and X-ray diffraction (XRD), while the specific surface area and porosity were determined using Brunauer –Emmett-Teller (BET) and Barrett –Joyner-Halenda (BJH) methods. Fourier transform-infrared (FTIR) spectrometer analysis was performed in transmittance mode in the range of 500 to 4000 cm^{-1} to investigate different functional groups. The electrochemical performance was evaluated by galvanostatic charge/discharge, cyclic voltammetry (CV) and electrochemical impedance spectroscopy (EIS).

In case of Cr_2O_3 samples, Cr_2O_3-$(MWCNTs)_{12\%}$ and Cr_2O_3-$(MWCNTs)_{12\%}$-PANI show 770 and 815 $mAhg^{-1}$ capacity with coulombic efficiency of 97.54 and 97.01%.

The result showed an increase in specific capacities, particularly in case of CNT_S based composites where the capacity is recorded as 1382$mAhg^{-1}$ at 50$mAhg^{-1}$ and 961 at 100$mAhg^{-1}$ in case of MoO_3-$(CNT)_{12\%}$. In short, this study suggests strategies of CNTs incorporation and polymer coating to address the problems of low electronic and ionic

conductivity and swelling of active material during cycling were successful and in future it can be applied to other active materials as well, along with changing the morphology from micro to nanoscale.

The WO_3-$(CNT)_{12\%}$-PANI nanocomposite exhibited remarkable good results with better rate capability, high reversible capacity and cycling ability, over 30 cycles. The observed specific capacity was 840 mAhg^{-1} at 100mAg^{-1}. The high electrochemical performance of nanocomposites is also credited to the PANI coating over the surface of WO_3 nanoparticles, which alleviate volume changes and improve cyclic stability and conductivity.

The WO_3-$(RGO)_{12\%}$-PANI nanocomposite exhibited remarkable good results with better rate capability, high reversible capacity and cycling ability, over 30 cycles. The observed specific capacity was 1188 mAhg^{-1} at 100mAg^{-1}. The high electrochemical performance of nanocomposites is also credited to the PANI coating over the surface of WO_3 nanoparticles, which alleviate volume changes and improve cyclic stability and conductivity. Hence, WO_3-$(RGO)_{12\%}$-PANI nanocomposite can be considered as a possible candidate for high-capacity anode materials for LIBs. Cr_2O_3-$(RGO)_{12\%}$-PANI exhibited discharge capacity of 891.81mAhg^{-1} at 100mAg^{-1} and 535.8mAhg^{-1} at 400mAg^{-1} after 30 cycles, while MoO_3-$(RGO)_{12\%}$-PANI showed discharged capacity of 1027.6 mAhg^{-1} at 100 mAg^{-1} and 656.8 mAhg^{-1} at 400 mAg^{-1} after 30 cycle.

This research indicates that there are methods that can be utilized to enhance the performance of anode materials. carbon nanotubes and reduced graphene oxides were included into the material. Moreover, PANI coating was applied in order to further find solutions to the issues. It is possible that in the future it will also be applicable to other active materials.

We are anticipating major breakthroughs in the field of lithium-ion batteries as a result of our expansion of our exploration beyond transition metal oxides to encompass ferrites, phosphides, and sulfides. These new compositions have the potential to significantly improve the overall performance of battery electrodes, as well as their capacity to store energy, cycling stability, rate capability, and overall performance. In this regard, continued research and development activities will contribute to the realization of next-generation energy storage systems, which will enable the broad development of lithium-ion batteries that are both environmentally friendly and high-performing.

References

(1) Cao, Z.; Qin, M.; Jia, B.; Zhang, L.; Wan, Q.; Wang, M.; Volinsky, A. A.; Qu, X. Facile route for synthesis of mesoporous Cr_2O_3 sheet as anode materials for Li-ion batteries. *Electrochim. Acta.,* **2014**, *139*, 76-81.

(2) Naqvi, S. R.; Jamshaid, S.; Naqvi, M.; Farooq, W.; Niazi, M. B. K.; Aman, Z.; Zubair, M.; Ali, M.; Shahbaz, M.; Inayat, A.; et al. Potential of biomass for bioenergy in Pakistan based on present case and future perspectives. *Renew. Sustain. Energy Rev.* **2018**, *81*, 1247-1258.

(3) Tawalbeh, M.; Khan, H. A.; Al-Othman, A.; Almomani, F.; Ajith, S. A comprehensive review on the recent advances in materials for thermal energy storage applications. *Int. J. Thermofluids.* **2023**, *18*, 100326.

(4) Azad, A. K.; Adhikari, J.; Halder, P.; Rasul, M. G.; Hassan, N. M. S.; Khan, M. M. K.; Naqvi, S. R.; Viswanathan, K. Performance, Emission and Combustion Characteristics of a Diesel Engine Powered by Macadamia and Grapeseed Biodiesels. *Energies.* **2020**, *13,* 2748.

(5) Almaita, E.; Alshkoor, S.; Abdelsalam, E.; Almomani, F. State of charge estimation for a group of lithium-ion batteries using long short-term memory neural network. *J. Energy Storage.* **2022**, *52*, 104761.

(6) Michael E. Mann*, R. S. B. M. K. H. Global-scale temperature patterns and climate forcing over the past six centuries. *Nature.* **1998**. *392*, 779-787.

(7) Asen, P.; Shahrokhian, S.; zad, A. I. Ternary nanostructures of Cr_2O_3/graphene oxide/conducting polymers for supercapacitor application. *J. Electroanal. Chem.* **2018**, *823*, 505-516.

(8) Raza, M. A.; Yousif, M.; Hassan, M.; Numan, M.; Abbas Kazmi, S. A. Site suitability for solar and wind energy in developing countries using combination of GIS-AHP; a case study of Pakistan. *Renew. Energy.***2023**, *206*, 180-191.

(9) Xu, J.; Akhtar, M.; Haris, M.; Muhammad, S.; Abban, O. J.; Taghizadeh-Hesary, F. Energy crisis, firm profitability, and productivity: An emerging economy perspective. *Energy Strat. Rev.* **2022**, *41*,100849.

(10) Shah, M. U.; Khanum, S.; Waqas, A.; Janjua, A. K.; Shakir, S. A techno-economic and socio-environmental planning of wind farms for sustainable development and transition to a decarbonized scenario: Pakistan as a case study. *SUSTAIN ENERGY TECHN.* **2023**, *55*, 102969.

(11) Kadiyala, A.; Kommalapati, R.; Huque, Z. Characterization of the life cycle greenhouse gas emissions from wind electricity generation systems. *International J. Energy Environ. Eng.* **2016**, *8* , 55-64.

(12) Bompard, E.; Grosso, D.; Huang, T.; Profumo, F.; Lei, X.; Li, D. World Decarbonization through Global Electricity Interconnections. *Energies.* **2018**, *11,1746.*

(13) Armaroli, N.; Balzani, V. Solar Electricity and Solar Fuels: Status and Perspectives in the Context of the Energy Transition. *Chemistry.* **2016**, *22*, 32-57.

(14) Hittinger, E.; Whitacre, J. F.; Apt, J. What properties of grid energy storage are most valuable? *J. Power Sources.* **2012**, *206*, 436-449.

(15) Rydh, C. J.; Sandén, B. A. Energy analysis of batteries in photovoltaic systems. Part II: Energy return factors and overall battery efficiencies. *Energy Convers. Manag.* **2005**, *46*, 1980-2000.

(16) Malik, A.; Lan, J.; Lenzen, M. Trends in Global Greenhouse Gas Emissions from 1990 to 2010. *Environ Sci Technol* **2016**, *50* , 4722-4730.

(17) Zhu, W.; Kamali, A. R. Green preparation of nanostructured β-MoO$_3$/hexagonal-shaped MoS2/graphene with enhanced lithium-ion storage performance. *J. Alloys Compd.* **2023**, *932*. 167724.

(18) Ding, J.; Sheng, R.; Zhang, Y.; Huang, Y.; Cheng, W.; Liu, Z.; Wang, X.; Guo, Y.; Wang, J.; Jia, D.; et al. Fe$_2$O$_3$/MoO$_3$/NG Heterostructure Enables High Pseudocapacitance and Fast Electrochemical Reaction Kinetics for Lithium-Ion Batteries. *ACS Appl Mater Interfaces.* **2022**, *14*, 37747-37758.

(19) Faizan, M.; Hussain, S.; Islam, M.; Kim, J. Y.; Han, D.; Bae, J. H.; Vikraman, D.; Ali, B.; Abbas, S.; Kim, H. S.; et al. MoO$_3$-MoS$_2$ Core-Shell Structured Hybrid Anode Materials for Lithium-Ion Batteries. *Nanomaterials.* **2022**, *12,* 2008.

(20) Chen, F.; Wang, J.; Huang, L.; Bao, H.; Shi, Y. Ordered Mesoporous Crystalline Mo-Doped WO2 Materials with High Tap Density as Anode Material for Lithium Ion Batteries. *Chem. Mater.* **2016**, *28*, 608-617.

(21) Abbas, S. M.; Ahmad, N.; Ata ur, R.; Rana, U. A.; Khan, S. U.-D.; Hussain, S.; Nam, K.-W. High rate capability and long cycle stability of Cr$_2$O$_3$ anode with CNTs for lithium ion batteries. *Electrochim Acta.* **2016**, *212*, 260-269.

(22) Guo, C.; Liu, Z.; Han, K.; Zhang, L.; Ding, X.; Wang, X.; Mai, L. Nano-Sized Niobium Tungsten Oxide Anode for Advanced Fast-Charge Lithium-Ion Batteries. *Small.* **2022**, *18* , 2107365.

(23) Zhou, S.; Zhou, H.; Zhang, Y.; Zhu, K.; Zhai, Y.; Wei, D.; Zeng, S. SnO_2 Anchored in S and N Co-Doped Carbon as the Anode for Long-Life Lithium-Ion Batteries. *Nanomater.* **2022**, *12,* 700.

(24) Zhu, J.; Ding, Y.; Ma, Z.; Tang, W.; Chen, X.; Lu, Y. Recent Progress on Nanostructured Transition Metal Oxides As Anode Materials for Lithium-Ion Batteries. *J. Electron. Mater.* **2022**, *51*, 3391-3417.

(25) Sharma, S.; Chand, P. Supercapacitor and electrochemical techniques: A brief review. *Results in Chemistry.* **2023**, *5*, 100885.

(26) Liao, Z.; Zhang, S.; Li, K.; Zhang, G.; Habetler, T. G. A survey of methods for monitoring and detecting thermal runaway of lithium-ion batteries. *J. Power Sources.* **2019**, *436*, 226879.

(27) Nzereogu, P. U.; Omah, A. D.; Ezema, F. I.; Iwuoha, E. I.; Nwanya, A. C. Anode materials for lithium-ion batteries: A review. *Appl. Surf. Sci.* **2022**, *9*, 100233.

(28) Kong, D.; Lv, H.; Ping, P.; Wang, G. A review of early warning methods of thermal runaway of lithium ion batteries. *J. Energy Storage.* **2023**, *15,* 10707*364*.

(29) Qi, Z.; Wu, Y.; Li, X.; Qu, Y.; Yang, Y.; Mei, D. Microwave-assisted synthesis of CuC2O4·xH2O for anode materials in lithium-ion batteries with a high capacity. *Ionics.* **2019**, *26* , 33-42.

(30) Xu, G.-L.; Gong, Y.-D.; Miao, C.; Wang, Q.; Nie, S.-Q.; Xin, Y.; Wen, M.-Y.; Liu, J.; Xiao, W. Sn nanoparticles embedded into porous hydrogel-derived pyrolytic carbon as composite anode materials for lithium-ion batteries. *Rare Metals.* **2022**, *41*, 3421-3431.

(31) Glibo, A.; Eshraghi, N.; Mautner, A.; Jahn, M.; Flandorfer, H.; Cupid, D. M. Synthesis and comparative performance study of crystalline and partially amorphous nano-sized SnS_2 as anode materials for lithium-ion batteries. *Electrochim Acta.* **2022**, *428*,140869.

(32) Ma, Q.; Zhang, Z.; Kou, P.; Wang, D.; Wang, Z.; Sun, H.; Zheng, R.; Liu, Y. In-situ synthesis of niobium-doped TiO_2 nanosheet arrays on double transition metal MXene (TiNbCT(x)) as stable anode material for lithium-ion batteries. *J Colloid Interface Sci.* **2022**, *617*, 147-155.

(33) Zhu, L.; Han, T.; Ding, Y.; Long, J.; Lin, X.; Liu, J. A metal–organic-framework derived $NiFe_2O_4$-NiCo-LDH nanocube as high-performance lithium-ion battery anode under different temperatures. *Appl. Surf. Sci.* **2022**, *599*.

(34) Xiao, Y.; Jiang, M.; Cao, M. Developing WO_3 as high-performance anode material for lithium-ion batteries. *Mater. Lett.* **2021**, *285*, 129129.

(35) Chu, Y.; Xiong, S. Mixed transition-metal oxides carbon core-shell nanostructures derived from heterometallic clusters for enhanced lithium storage. *Chin. Chem. Lett.* **2022**, *33*, 486-490.

(36) Wang, Q.; Kang, L.; Xing, Z.; Nie, C.; Hong, H.; Zhou, X.; Yun, Q.; Ju, Z.; Chen, B. Prussian Blue Analogue-Derived $ZnO/ZnFe_2O_4$ Core-Shell Nanospheres as High-Performance Anodes for Lithium-Ion and Potassium-Ion Batteries. *Batter. Supercaps.* **2022**, *6*. 202200411.

(37) Khan, S. A.; Ali, S.; Saeed, K.; Usman, M.; Khan, I. Advanced cathode materials and efficient electrolytes for rechargeable batteries: practical challenges and future perspectives. *J. Mater. Chem.* **2019**, *7,* 10159-10173.

(38) Peiris, M. D. H. C.; Brennan, S.; Liepinya, D.; Liu, H.; Smeu, M. Computational determination of the solvation structure of $LiBF_4$ and $LiPF_6$ salts in battery electrolytes. *Colloids Surf. A: Physicochem. Eng. Asp.* **2023**, *674*, 131831.

(39) Zhao, C.; Yang, Z.; Zhou, X.; Hao, Z.; Chen, J.; Wang, Z.; Chen, X.; Wu, X.; Li, L.; Li, L.; et al. Recent Progress on Electrolyte Boosting Initial Coulombic Efficiency in Lithium-Ion Batteries. *Adv. Funct. Mater.* **2023**,34, 2303457.

(40) Liu, Y. K.; Zhao, C. Z.; Du, J.; Zhang, X. Q.; Chen, A. B.; Zhang, Q. Research Progresses of Liquid Electrolytes in Lithium-Ion Batteries. *Small.* **2023**, *19,* 2205315.

(41) Golubkov, A. W.; Fuchs, D.; Wagner, J.; Wiltsche, H.; Stangl, C.; Fauler, G.; Voitic, G.; Thaler, A.; Hacker, V. Thermal-runaway experiments on consumer Li-ion batteries with metal-oxide and olivin-type cathodes. *RSC Adv.* **2014**, *4*, 3633-3642.

(42) Sashmitha, K.; Rani, M. U. A comprehensive review of polymer electrolyte for lithium-ion battery. *Polym. Bull.* **2022**, *80*, 89-135.

(43) Shu-Lei Chou, a., * Yuede Pan, a Jia-Zhao Wang, a Hua-Kun Liu, a Shi-Xue Dou. Small things make big difference: Binder effects on the performance of Li and Na batteries. *Phys. Chem. Chem. Phys..***2014**, *16,* 20347-20359.

(44) Jing Lia, L. C., M.N. Obrovacb, K.C. Hewittc and J.R. Dahnc, a. Effect of heat treatment on Si electrodes using polyvinylidene fluoride binder. *JES.* **2008**, *155*, A234.

(45) G. Liu, a., *,z H. Zheng,a,c A. S. Simens,b,d A. M. Minor,b X. Song,a and; Battaglia, V. S. Optimization of Acetylene Black Conductive Additive and PVDF Composition for High-Power Rechargeable Lithium-Ion Cells. *JES*. **2007**,*154*, A1129.

(46) Chen, Y.; Kang, Y.; Zhao, Y.; Wang, L.; Liu, J.; Li, Y.; Liang, Z.; He, X.; Li, X.; Tavajohi, N.; et al. A review of lithium-ion battery safety concerns: The issues, strategies, and testing standards. *J. Energy Chem.***2021**, *59*, 83-99.

(47) Raijmakers, L. H. J.; Danilov, D. L.; Eichel, R. A.; Notten, P. H. L. A review on various temperature-indication methods for Li-ion batteries. *Appl. Energy.* **2019**, *240*, 918-945.

(48) Zhang, X.; Li, Z.; Luo, L.; Fan, Y.; Du, Z. A review on thermal management of lithium-ion batteries for electric vehicles. *Energy.* **2022**, *238*, 121652.

(49) Qiu, Y.; Jiang, F. A review on passive and active strategies of enhancing the safety of lithium-ion batteries. *Int. J. Heat Mass Transf.* **2022**, *184*, 122288.

(50) A. J. Smith, J. C. B., and J. R. Dahn. A High Precision Study of the Coulombic Efficiency of Li-Ion Batteries. *ESL*, **2010**, *12*, A177.

(51) Holtstiege, F.; Wilken, A.; Winter, M.; Placke, T. Running out of lithium? A route to differentiate between capacity losses and active lithium losses in lithium-ion batteries. *Phys Chem Chem Phys.* **2017**. *19,* 25905-25918.

(52) Sakamoto, J. S.; Dunn, B. Vanadium Oxide-Carbon Nanotube Composite Electrodes for Use in Secondary Lithium Batteries. *JES.* **2002**, *149*, A26.

(53) L. Y. Beaulieu, a., * K. W. Eberman,b,** R. L. Turner,b,** L. J. Krause,b,** and J. R. Dahna. Colossal Reversible Volume Changes in Lithium Alloys. *ECS.* **2001***, 4 A137.*

(54) Liu, H. K.; Guo, Z. P.; Wang, J. Z.; Konstantinov, K. Si-based anode materials for lithium rechargeable batteries. *J. Mater. Chem.* **2010**. *20*, 10055-10057.

(55) Park, C. M.; Kim, J. H.; Kim, H.; Sohn, H. J. Li-alloy based anode materials for Li secondary batteries. *Chem Soc Rev.* **2010**. *39,* 3115-3141.

(56) Pan, Q.; Qin, L.; Liu, J.; Wang, H. Flower-like ZnO–NiO–C films with high reversible capacity and rate capability for lithium-ion batteries. *Electrochim Acta.* **2010**. *55*, 5780-5785.

(57) NuLi, Y.; Zeng, R.; Zhang, P.; Guo, Z.; Liu, H. Controlled synthesis of α-Fe_2O_3 nanostructures and their size-dependent electrochemical properties for lithium-ion batteries. *J. Power Sources.* **2008**. *184*, 456-461.

(58) Xiang, J. Y.; Tu, J. P.; Zhang, J.; Zhong, J.; Zhang, D.; Cheng, J. P. Incorporation of MWCNTs into leaf-like CuO nanoplates for superior reversible Li-ion storage. *Electrochem. commun.* **2010**. *8*, 1103-1107.

(59) Li, W. Y.; Xu, L. N.; Chen, J. Co_3O_4 Nanomaterials in Lithium-Ion Batteries and Gas Sensors. *Adv. Funct. Mater.* **2005**. *15*, 851-857.

(60) Reddy, M. V.; Yu, T.; Sow, C. H.; Shen, Z. X.; Lim, C. T.; Subba Rao, G. V.; Chowdari, B. V. R. α-Fe_2O_3 Nanoflakes as an Anode Material for Li-Ion Batteries. *Adv. Funct. Mater.* **2007**. *17,* 2792-2799.

(61) Cui, Z.-M.; Jiang, L.-Y.; Song, W.-G.; Guo, Y.-G. High-Yield Gas−Liquid Interfacial Synthesis of Highly Dispersed Fe_3O_4 Nanocrystals and Their Application in Lithium-Ion Batteries. *Chem. Mater.* **2009**, *21*, 1162-1166.

(62) Anh Tran, T.; Krishnamoorthy, K.; Song, Y. W.; Cho, S. K.; Kim, S. J. Toxicity of nano molybdenum trioxide toward invasive breast cancer cells. *ACS Appl Mater Interfaces.* **2014**, *6*, 2980-2986.

(63) Chithambararaj, A.; Rajeswari Yogamalar, N.; Bose, A. C. Hydrothermally Synthesized h-MoO_3 and α-MoO_3 Nanocrystals: New Findings on Crystal-Structure-Dependent Charge Transport. *Cryst. Growth Des.* **2016**, *16*, 1984-1995.

(64) Chernova, N. A.; Roppolo, M.; Dillon, A. C.; Whittingham, M. S. Layered vanadium and molybdenum oxides: batteries and electrochromics. *J. Mater. Chem.* **2009**, *19,* 2526-2552.

(65) Sreedhara, M. B.; Santhosha, A. L.; Bhattacharyya, A. J.; Rao, C. N. R. Composite of few-layer MoO_3 nanosheets with graphene as a high-performance anode for sodium-ion batteries. *J. Mater. Chem A.* **2016**, *4*, 9466-9471.

(66) Mohan, V. M.; Chen, W.; Murakami, K. Synthesis, structure and electrochemical properties of polyaniline/MoO_3 nanobelt composite for lithium battery. *Mater. Res. Bull.* **2013**, *48*, 603-608.

(67) Liu, C.-L.; Wang, Y.; Zhang, C.; Li, X.-S.; Dong, W.-S. In situ synthesis of α-MoO_3/graphene composites as anode materials for lithium-ion battery. *Mater. Chem. Phys.* **2014**, *143*, 1111-1118.

(68) Shahsank, M.; Bhojya Naik, H. S.; Sumedha, H. N.; Nagaraju, G. Implementing an in-situ carbon formation of MoO_3 nanoparticles for high performance lithium-ion battery. *Ceram. Int.* **2021**, *47*, 10261-10267.

(69) Nadimicherla, R.; Zha, R.; Wei, L.; Guo, X. Single crystalline flowerlike α-MoO_3 nanorods and their application as anode material for lithium-ion batteries. *J. Alloys Compd.* **2016**, *687*, 79-86.

(70) Klinbumrung, A.; Thongtem, T.; Thongtem, S. Characterization of Orthorhombicα-MoO_3 Microplates Produced by a Microwave Plasma Process. *J. Nanomater.* **2012**, *5*, 930763.

(71) Bai, S.; Chen, C.; Luo, R.; Chen, A.; Li, D. Synthesis of MoO_3/reduced graphene oxide hybrids and mechanism of enhancing H_2S sensing performances. *Sens. Actuator A-Phys.* **2015**, *216*, 113-120.

(72) Lee, S.-H.; Kim, Y.-H.; Deshpande, R.; Parilla, P. A.; Whitney, E.; Gillaspie, D. T.; Jones, K. M.; Mahan, A. H.; Zhang, S.; Dillon, A. C. Reversible Lithium-Ion Insertion in Molybdenum Oxide Nanoparticles. *Adv. Mater.* **2008**, *20*, 3627-3632.

(73) Ma, G.; Chen, Z.; Chen, Z.; Jin, M.; Meng, Q.; Yuan, M.; Wang, X.; Liu, J.-M.; Zhou, G. Constructing novel WO_3/Fe(III) nanofibers photocatalysts with enhanced visible-light-driven photocatalytic activity via interfacial charge transfer effect. *Mater. Today Energy.* **2017**, *3*, 45-52.

(74) Cai, Z.-X.; Li, H.-Y.; Ding, J.-C.; Guo, X. Hierarchical flowerlike WO_3 nanostructures assembled by porous nanoflakes for enhanced NO gas sensing. *Sens. Actuators B: Chem.***2017**, *246*, 225-234.

(75) Zhu, T.; Chong, M. N.; Chan, E. S. Nanostructured tungsten trioxide thin films synthesized for photoelectrocatalytic water oxidation: a review. *ChemSusChem.* **2014**, *7*, 2974-2997.

(76) Yang, B.; Miao, P.; Cui, J. Characteristics of amorphous WO_3 thin films as anode materials for lithium-ion batteries. *Journal of Materials Science: Electron. Mater.* **2020**, *31*, 11071-11076.

(77) Huang, Y.; Lu, R.; Wang, M.; Sakamoto, J.; Poudeu, P. F. P. Hexagonal-WO_3 nanorods encapsulated in nitrogen and sulfur co-doped reduced graphene oxide as a high-performance anode material for lithium ion batteries. *J. Solid State Chem.* **2020**, *282*,121068.

(78) Mubasher; Mumtaz, M.; Lashari, N. U. R.; Hassan, M.; Tangsee, S.; Khan, M. T. Multi-walled carbon nanotubes and chromium ferrites nanoparticles nanohybrids as anode materials for lithium-ion batteries. *J. Alloys Compd.* **2021**, *872*,159654.

(79) Guo, B.; Chi, M.; Sun, X.-G.; Dai, S. Mesoporous carbon–Cr_2O_3 composite as an anode material for lithium ion batteries. *J. Power Sources.* **2012**, *205*, 495-499.

(80) Dupont, L.; Laruelle, S.; Grugeon, S.; Dickinson, C.; Zhou, W.; Tarascon, J. M. Mesoporous Cr_2O_3 as negative electrode in lithium batteries: TEM study of the texture effect on the polymeric layer formation. *J. Power Sources* **2008**, *175*, 502- 509.

(81) Ramasamy, R. P.; Ramadass, P.; Haran, B. S.; Popov, B. N. Synthesis, characterization and cycling performance of novel chromium oxide cathode materials for lithium batteries. *J. Power Sources.* **2003**, *124*, 155-162.

(82) Langli Luo, § Jinsong Wu,*,†,§ Junming Xu,†,‡ and Vinayak P. Dravid*,†. Atomic Resolution Study of Reversible Conversion Reaction in Metal Oxide Electrodes for Lithium-Ion Battery. *ACS Nano*. **2014**, *8*, 11560-11566.

(83) Kim, J.-J.; Ahn, C.; Bak, W.; Yoo, W. C.; Sung, Y.-E. Improved electrochemical performance of a three-dimensional ordered mesoporous carbon based lithium ion battery using vinylene carbonate. *Mater. Today Commun.* **2016**, *6*, 69-73.

(84) Zhong, X.-B.; Yang, Z.-Z.; Wang, H.-Y.; Lu, L.; Jin, B.; Zha, M.; Jiang, Q.-C. A novel approach to facilely synthesize mesoporous $ZnFe_2O_4$ nanorods for lithium ion batteries. *J. Power Sources.* **2016**, *306*, 718-723.

(85) Hill, A. H.; Harrison, A.; Dickinson, C.; Zhou, W.; Kockelmann, W. Crystallographic and magnetic studies of mesoporous eskolaite. *Microporous Mesoporous Mater.* **2010**, *130*, 280-286.

(86) Yamashita, H.; Horiuchi, Y.; Imaoka, S.; Nishio, S.; Nishiyama, N.; Mori, K. Surface hydrophilic–hydrophobic property on transparent mesoporous silica thin films containing chromium oxide single-site photocatalyst. *Catal. Today.* **2008**, *132*, 146-152.

(87) Ullah, S.; Khan, I. A.; Choucair, M.; Badshah, A.; Khan, I.; Nadeem, M. A. A novel Cr_2O_3 -carbon composite as a high performance pseudo-capacitor electrode material. *Electrochim Acta.* **2015**, *171*, 142-149.

(88) Wang, W.; Xiong, F.; Zhu, S.; Chen, J.; Xie, J.; An, Q. Defect engineering in molybdenum-based electrode materials for energy storage. *eScience* **2022**, *2*, 278-294.

(89) Cai, L.; Rao, P. M.; Zheng, X. Morphology-controlled flame synthesis of single, branched, and flower-like alpha-MoO$_3$ nanobelt arrays. *Nano Lett.* **2011**, *11*, 872-877.

(90) Li, J.; Liu, X. Preparation and characterization of α-MoO$_3$ nanobelt and its application in supercapacitor. *Mater. Lett.* **2013**, *112*, 39-42.

(91) Yan, D.; Luo, X.; Zhang, H.; Zhu, G.; Chen, L.; Chen, G.; Xu, H.; Yu, A. Single-crystalline α-MoO3 microbelts derived from a bio-templating method for superior lithium storage application. *J. Alloys Compd.* **2016**, *688*, 481-486.

(92) Yuan, L.; Wang, J.; Chew, S. Y.; Chen, J.; Guo, Z. P.; Zhao, L.; Konstantinov, K.; Liu, H. K. Synthesis and characterization of SnO2–polypyrrole composite for lithium-ion battery. *J. Power Sources.* **2007**, *174*, 1183-1187.

(93) Cai, J.-J.; Zuo, P.-J.; Cheng, X.-Q.; Xu, Y.-H.; Yin, G.-P. Nano-silicon/polyaniline composite for lithium storage. *Electrochem. commun* **2010**, *12*, 1572-1575.

(94) Li, B.; Li, X.; Li, W.; Wang, Y.; Uchaker, E.; Pei, Y.; Cao, X.; Li, S.; Huang, B.; Cao, G. Mesoporous Tungsten Trioxide Polyaniline Nanocomposite as an Anode Material for High-Performance Lithium-Ion Batteries. *Chem Nano Mat.* **2016**, *2* , 281-289.

(95) Yang, S.; Huo, J.; Song, H.; Chen, X. A comparative study of electrochemical properties of two kinds of carbon nanotubes as anode materials for lithium-ion batteries. *Electrochim Acta* **2008**, *53*, 2238-2244.

(96) Belin, T.; Epron, F. Characterization methods of carbon nanotubes: a review. *Mater. sci. eng: B.* **2005**, *119*, 105-118.

(97) Sinnott, S. B.; Andrews, R. Carbon Nanotubes: Synthesis, Properties, and ApplicationsCrit. Rev. Solid State Mater. Sci. **2001**, *26*, 145- 249.

(98) Ali Eatemadi1, H. D., Hamzeh Karimkhanloo1, Mohammad Kouhi4*, Nosratollah Zarghami1, Abolfazl Akbarzadeh2,5*, Mozhgan Abasi1, Younes Hanifehpour3 and Sang Woo Joo. Carbon nanotubes: properties, synthesis, purification, and medical applications. *Nanoscale Res. Lett*, **2014,** *9*, 1-13

(99) Lee, S.; Kim, Y.-J.; Kim, D.-H.; Ku, B.-C.; Joh, H.-I. Synthesis and properties of thermally reduced graphene oxide/polyacrylonitrile composites. *J. Phys. Chem. Solids.* **2012**, *73*, 741-743.

(100) Papageorgiou, D. G.; Kinloch, I. A.; Young, R. J. Mechanical properties of graphene and graphene-based nanocomposites. *Prog. Mater. Sci.* **2017**, *90*, 75-127.

(101) Sohni, S.; Hassan, T.; Khan, S. B.; Akhtar, K.; Bakhsh, E. M.; Hashim, R.; Nidaullah, H.; Khan, M.; Khan, S. A. Lignin nanoparticles-reduced graphene oxide based hydrogel: A novel strategy for environmental applications. *Int J Biol Macromol* **2023**, *225*, 1426-1436.

(102) Pham, V. H.; Pham, H. D.; Dang, T. T.; Hur, S. H.; Kim, E. J.; Kong, B. S.; Kim, S.; Chung, J. S. Chemical reduction of an aqueous suspension of graphene oxide by nascent hydrogen. . *J. Mater. Chem.* **2012**, *22*, 10530-10536.

(103) Huang, X.; Yin, Z.; Wu, S.; Qi, X.; He, Q.; Zhang, Q.; Yan, Q.; Boey, F.; Zhang, H. Graphene-based materials: synthesis, characterization, properties, and applications. *Small* **2011**, *7*, 1876-1902.

(104) Zeng, Z.; Chen, Y.; Zhu, X.; Yu, L. Polyaniline-supported nano metal-catalyzed coupling reactions: Opportunities and challenges. *Chin. Chem. Lett.* **2023**, *34*. 107728.

(105) Khan, N. A.; Hassan, M.; Lee, H. J.; Jhung, S. H. Highly porous polyaniline- or polypyrrole-derived carbons: Preparation, characterization, and applications in adsorption. *J. Chem. Eng.* **2023**, *474*, 145472.

(106) Babel, V.; Hiran, B. L. A review on polyaniline composites: Synthesis, characterization, and applications. *Polym. Compos.* **2021**, *42*, 3142-3157.

(107) Feng, M.; Tian, J.; Xie, H.; Kang, Y.; Shan, Z. Nano-silicon/polyaniline composites with an enhanced reversible capacity as anode materials for lithium-ion batteries. *J. Solid State Electrochem.* **2015**, *19*, 1773-1782.

(108) Wang, S.; Hu, L.; Hu, Y.; Jiao, S. Conductive polyaniline capped Fe_2O_3 composite anode for high rate lithium ion batteries. *Mater. Chem. Phys.* **2014**, *146* , 289-294.

(109) Laresgoiti, I.; Käbitz, S.; Ecker, M.; Sauer, D. U. Modeling mechanical degradation in lithium ion batteries during cycling: Solid electrolyte interphase fracture. *J. Power Sources.* **2015**, *300*, 112-122.

(110) Menkin, S.; Golodnitsky, D.; Peled, E. Artificial solid-electrolyte interphase (SEI) for improved cycleability and safety of lithium–ion cells for EV applications. *Electrochem Commun.* **2009**, *11*, 1789-1791.

(111) Nojabaee, M.; Kopljar, D.; Wagner, N.; Friedrich, K. A. Understanding the Nature of Solid-Electrolyte Interphase on Lithium Metal in Liquid Electrolytes: A Review on Growth, Properties, and Application-Related Challenges. *Batter. Supercaps* **2021**, *4*, 909-922.

(112) Wang, A.; Kadam, S.; Li, H.; Shi, S.; Qi, Y. Review on modeling of the anode solid electrolyte interphase (SEI) for lithium-ion batteries. *npj Comput Mater.* **2018**, *4* ,15.

(113) Verma, P.; Maire, P.; Novák, P. A review of the features and analyses of the solid electrolyte interphase in Li-ion batteries. *Electrochimic Acta.* **2010**, *55* (22), 6332-6341.

(114) Wu, H.; Jia, H.; Wang, C.; Zhang, J. G.; Xu, W. Recent Progress in Understanding Solid Electrolyte Interphase on Lithium Metal Anodes. *Adv. Energy Mater.* **2020**, *11, 2003092.*

(115) Zhang, X.; Fu, C.; Li, J.; Yao, C.; Lu, T.; Pan, L. MoO_3/reduced graphene oxide composites as anode material for sodium ion batteries. *Ceram. Int.* **2017**, *43*, 3769-3773.

(116) Srivastava*b, P. R. a. a. S. K. Nanostructured Anode Materials for Lithium-Ion Batteries. J. Mater. Chem A **. 2014**, 3, 2454-2484.

(117) Ma, F.; Yuan, A.; Xu, J.; Hu, P. Porous alpha-MoO_3/MWCNT nanocomposite synthesized via a surfactant-assisted solvothermal route as a lithium-ion-battery high-capacity anode material with excellent rate capability and cyclability. *ACS Appl Mater Interfaces.* **2015**, *7* , 15531-15541.

(118) Sun1, H.; 2, G.; , D. H., Alberto Ansaldo1; , D. A. D., 3 , Vittorio Pellegrini1; , J. B. B., An. Carbon nanotubes-bridged molybdenum trioxide nanosheets as high performance anode for lithium ion batteries. **2017**, *2D Materials*, *5*, 015024.

(119) Fu, Y.; Gu, H.; Yan, X.; Liu, J.; Wang, Y.; Huang, J.; Li, X.; Lv, H.; Wang, X.; Guo, J.; et al. Chromium(III) oxide carbon nanocomposites lithium-ion battery anodes with enhanced energy conversion performance. *J. Chem. Eng.* **2015**, *277*, 186-193.

(120) Bai, Y.; Qu, S.; Jia, Z.; Zhang, L.; Zhu, G.; Feng, A.; Wu, G.; Wu, H. Cr2O3 nanocrystal anode materials with improved cyclic stability for lithium ion batteries. *J. Mater. Sci.: Mater. Electron.* **2018**, *29*, 11795-11800.

(121) Kim, J.; Jo, Y.; Ahmed, A. T. A.; Inamdar, A. I.; Cho, S.; Kim, H.; Im, H. Density-modulated multilayered homo-junction tungsten oxide anode materials for high-

capacity Li-ion batteries with long-term stability. *Int. J. Energy Res.* **2021**, *46*, 1387-1397.

(122) Park, S. K.; Lee, H. J.; Lee, M. H.; Park, H. S. Hierarchically structured reduced graphene oxide/WO3 frameworks for an application into lithium ion battery anodes. *J. Chem. Eng.* **2015**, *281*, 724-729.

(123) Sheng, D.; Zhang, M.; Wang, X.; Zhou, S.; Fu, S.; Liu, X.; Zhang, Q. Carbon nanotubes embedded in α-MoO_3 nanoribbons for enhanced lithium-ion storage. *J. Mater. Sci.: Mater. Electron.* **2022**, *33*, 11743-11752.

(124) Cheng, X.; Li, Y.; Sang, L.; Ma, J.; Shi, H.; Liu, X.; Lu, J.; Zhang, Y. Boosting the electrochemical performance of MoO_3 anode for long-life lithium ion batteries: Dominated by an ultrathin TiO_2 passivation layer. *Electrochimic Acta.* **2018**, *269*, 241-249.

(125) Ren, H.; Sun, S.; Cui, J.; Li, X. Synthesis, Functional Modifications, and Diversified Applications of Molybdenum Oxides Micro-/Nanocrystals: Cryst.Growth Des. **2018**, *18*, 6326-6369.

(126) Li, T.; Beidaghi, M.; Xiao, X.; Huang, L.; Hu, Z.; Sun, W.; Chen, X.; Gogotsi, Y.; Zhou, J. Ethanol reduced molybdenum trioxide for Li-ion capacitors. *Nano Energy.* **2016**, *26*, 100-107.

(127) Li, Y.; Sun, H.; Cheng, X.; Zhang, Y.; Zhao, K. In-situ TEM experiments and first-principles studies on the electrochemical and mechanical behaviors of α-MoO_3 in Li-ion batteries. *Nano Energy.* **2016**, *27*, 95-102.

(128) Yen, J.-Z.; Yang, Y.-C.; Tuan, H.-Y. Interface engineering of high entropy Oxide Polyaniline heterojunction enables highly stable and excellent lithium ion storage performance. *J. Chem. Eng.* **2022**, *450*, 137924.

(129) Onat, Burcu, Gonca Yasar, Coskun Ayvaz, Indoor environmental quality in university Laboratories. *Pamukkale U J Eng SC.* **2023**,*6,642-649.*

(130) Khan, H.; Yerramilli, A. S.; D'Oliveira, A.; Alford, T. L.; Boffito, D. C.; Patience, G. S. Experimental methods in chemical engineering: X-ray diffraction spectroscopy—XRD. *CJCE,* **2020**, *98,* 1255-1266.

(131) Mishra, S. T. R. T. A. K. Z. R. K. Spectroscopic Methods for Nanomaterials Characterization. **2017**.

(132) By Stephen Brunauer, P. H. E. a. E. T. Adsorption of Gases in Multimolecular Layers. **1938**.

(133) SING, K. S. W. REPORTING PHYSISORPTION DATA FOR GAS/SOLID SYSTEMS with Special Reference to the Determination of Surface Area and Porosity. Pure Appl. Chem. **1985**, 157, 603-619.

(134) Sing, K. The use of nitrogen adsorption for the characterisation of porous materials. Colloids Surf. A: Physicochem. Eng. Asp. **2001**, 187, 3-9.

(135) Stevie, F. A.; Donley, C. L. Introduction to x-ray photoelectron spectroscopy. *J. Vac. Sci. Technol. A: Vacuum, Surfaces, and Films* **2020**, 6, *38* .

(136) Greczynski, G.; Hultman, L. A step-by-step guide to perform x-ray photoelectron spectroscopy. *J. Phys. D Appl. Phys.* **2022**,8, *132*.

(137) Fadley, C. S. X-ray photoelectron spectroscopy: Progress and perspectives. *J. Electron Spectros. Relat. Phenomena.* **2010**, *17*, 2-32.

(138) Sherwood, A. P. a. P. A. Data Analysis Techniques in X-ray Photoelectron Spectros. *Analyt Chem.* **1982**,5, 13-19.

(139) Alhendal, A.; Rashad, M.; Husain, A.; Mouffuok, F.; Bumajdad, A. A chromia-based sorbent for the enrichment of phosphotyrosine. *J Chromatogr A.* **2022**, *1671*, 462991.

(140) Benítez, A.; Marangon, V.; Hernández-Rentero, C.; Caballero, Á.; Morales, J.; Hassoun, J. Porous Cr_2O_3-C composite derived from metal organic framework in efficient semi-liquid lithium-sulfur battery. *Mater. Chem. Phys.* **2020**, *255*,123484.

(141) Singh, J.; Verma, V.; Kumar, R.; Sharma, S.; Kumar, R. Effect of structural and thermal disorder on the optical band gap energy of Cr_2O_3nanoparticles. *Mater. Res. Express.* **2019**, *6*. 085039.

(142) Abdullah, M. M.; Rajab, F. M.; Al-Abbas, S. M. Structural and optical characterization of Cr_2O_3 nanostructures: Evaluation of its dielectric properties. *AIP Advances* **2014**, *4* .4867012.

(143) Azzam, E. M. S.; Fathy, N. A.; El-Khouly, S. M.; Sami, R. M. Enhancement the photocatalytic degradation of methylene blue dye using fabricated $CNTs/TiO_2$/AgNPs/Surfactant nanocomposites. *JWPE.* **2019**, *28*, 311-321.

(144) Wang, S.; Zhou, S. Photodegradation of methyl orange by photocatalyst of CNTs/P-TiO(2) under UV and visible-light irradiation. *J Hazard Mater* **2011**, *185*, 77-85.

(145) Liao, G.; Chen, S.; Quan, X.; Zhang, Y.; Zhao, H. Remarkable improvement of visible light photocatalysis with PANI modified core–shell mesoporous TiO_2 microspheres. *Appl. Catal. Environ.* **2011**, *102*, 126-131.

(146) Zekaik, A.; Benhebal, H.; Benrabah, B. Synthesis and characterization of Cu doped chromium oxide (Cr_2O_3) thin films. *HTMP.* **2019**, *38*, 806-812.

(147) Zamani, N.; Modarresi-Alam, A. R.; Noroozifar, M.; Javanbakht, M. The improved performance of lithium-ion batteries via the novel electron transport catalytic role of polyaniline (PANI) in PANI/Co_3O_4–CuO raspberry as new anode material. *J. Appl. Electrochem .* **2019**, *49*, 327-340.

(148) Sadeghi, N.; Khorshidi, A.; Ganjali, M. Cr_2O_3 nanoparticles composited with MWCNTs as an efficient electrocatalyst for the oxygen reduction reaction. *Inorg. Chem. Commun.* **2021**, *126*, 108489.

(149) Abbas, S. M.; Hussain, S. T.; Ali, S.; Abbas, F.; Ahmad, N.; Ali, N.; Khan, Y. One-pot synthesis of a composite of monodispersed CuO nanospheres on carbon nanotubes as anode material for lithium-ion batteries. *J. Alloys Compd.* **2013**, *574*, 221-226.

(150) Li, X.; Huang, X.; Liu, D.; Wang, X.; Song, S.; Zhou, L.; Zhang, H. Synthesis of 3D Hierarchical Fe_3O_4/Graphene Composites with High Lithium Storage Capacity and for Controlled Drug Delivery. *J. Phys. Chem. C.* **2011**, *115*, 21567-21573.

(151) Abbas, S. M.; Ali, S.; Niaz, N. A.; Ali, N.; Ahmed, R.; Ahmad, N. Superior electrochemical performance of mesoporous Fe_3O_4/CNT nanocomposites as anode material for lithium ion batteries. *J. Alloys Compd.* **2014**, *611*, 260- 266.

(152) Abbas, S. M.; Zia ur, R.; Rana, U. A.; Khan, S. U.-D.; Iqbal, Z.; Ahmad, N. MoN-decorated nitrogen doped carbon nanotubes anode with high lithium storage performance. *Electrochimic Acta .***2016**, *190*, 988-996.

(153) Xia, Q.; Zhao, H.; Du, Z.; Zeng, Z.; Gao, C.; Zhang, Z.; Du, X.; Kulka, A.; Świerczek, K. Facile synthesis of MoO_3/carbon nanobelts as high-performance anode material for lithium ion batteries. *Electrochimic Acta.* **2015**, *180*, 947-956.

(154) Saraf, M.; Shuck, C. E.; Norouzi, N.; Matthews, K.; Inman, A.; Zhang, T.; Pomerantseva, E.; Gogotsi, Y. Free-Standing α-MoO_3/Ti_3C_2 MXene Hybrid Electrode in Water-in-Salt Electrolytes. *EEM. 6*, e12516

(155) Sharma, R.; Sarkar, A.; Jha, R.; Sharma, A. K.; Bhushan, M.; Bhardwaj, R. Synthesis & material properties of α-MoO$_3$ nanoparticles. *Mater. Today Energy.* **2022**, *48*, 683-686.

(156) Chiang, T. H.; Yeh, H. C. A novel synthesis of α-MoO$_3$ nanobelts and the characterization. *J. Alloys Compd.* **2014**, *585*, 535-541.

(157) Navas, I.; Vinodkumar, R.; Lethy, K. J.; Detty, A. P.; Ganesan, V.; Sathe, V.; Mahadevan Pillai, V. P. Growth and characterization of molybdenum oxide nanorods by RF magnetron sputtering and subsequent annealing. *J. Phys. D: Appl. Phys.* **2009**, *42* (17), 175305.

(158) Wu, Z.; Wang, D.; Liang, X.; Sun, A. Ultrasonic-assisted preparation of metastable hexagonal MoO$_3$ nanorods and their transformation to microbelts. *Ultrason Sonochem* **2011**, *18* , 288-292.

(159) Sen, S. K.; Dutta, S.; Khan, M. R.; Manir, M. S.; Dutta, S.; Al Mortuza, A.; Razia, S.; Hakim, M. A. Characterization and Antibacterial Activity Study of Hydrothermally Synthesized h-MoO$_3$ Nanorods and α-MoO$_3$ Nanoplates. *J. Bionanosci.* **2019**, *9* , 873-882.

(160) Cao, L.; Li, Y.; Wu, J.; Li, W.; Huang, J.; Feng, Y.; Yao, C.; Li, J.; Wang, R.; Kang, Q.; et al. Facile synthesis of carbon coated MoO3 nanorods decorated with WO2 nanoparticles as stable anodes for lithium-ion batteries. *J. Alloys Compd.* **2018**, *744*, 672-678.

(161) Oh, S. H.; Park, S. M.; Kang, D.-W.; Kang, Y. C.; Cho, J. S. Fibrous network of highly integrated carbon nanotubes/MoO3 composite bundles anchored with MoO$_3$ nanoplates for superior lithium ion battery anodes J. Ind. Eng. Chem. **2020**, *83*, 438-448.

(162) Li, M.-Y.; Wang, Y.; Liu, C.-L.; Gao, H.; Dong, W.-S. Iron oxide/carbon microsphere lithium-ion battery electrode with high capacity and good cycling stability. *Electrochimic Acta.* **2012**, *67*, 187-193.

(163) Liu, Z.; Sun, L.; Yang, W.; Yang, J.; Han, S.; Chen, D.; Liu, Y.; Liu, X. The synergic effects of Na and K co-doping on the crystal structure and electrochemical properties of Li$_4$Ti$_5$O$_{12}$ as anode material for lithium ion battery. *Solid State Sci.* **2015**, *44*, 39-44.

(164) Francis, M. K.; Bhargav, P. B.; Ramesh, A.; Ahmed, N.; Balaji, C. Electrochemical performance analysis of NiMoO$_4$/α-MoO$_3$ composite as anode material for high capacity lithium-ion batteries. *APPL PHYS A-MATER.* **2022**,*128, 132.*

(165) Deng, Z.; Zhang, Z.; Lai, Y.; Liu, J.; Li, J.; Liu, Y. Electrochemical Impedance Spectroscopy Study of a Lithium/Sulfur Battery: Modeling and Analysis of Capacity Fading. *Journal of The Electrochemical Society* **2013**, *160* , A553-A558.

(166) Kim, J. H.; Kwak, E.; Oh, K. Y. Degradation pathways dependency of a lithium iron phosphate battery on temperature and compressive force. *International Journal of Energy Research* **2020**, *45*, 6888-6906.

(167) Mishra, P.; Yavas, D.; Bastawros, A. F.; Hebert, K. R. Electrochemical impedance spectroscopy analysis of corrosion product layer formation on pipeline steel. *Electrochimica Acta* **2020**, *346*, 136232.

(168) Hou, J.-B.; Zhang, K.; Xiao, J.-H.; Xu, Z.-Q.; Gao, W.-J.; Gao, X.-Y.; Zhou, S.-K.; Jiao, Z.-Z.; Yi, M.-R.; Yin, Y.-H.; et al. Modified tungsten oxide as a binder-free anode in lithium-ion battery for improving electrochemical stability. *Tungsten* **2022**, *4* , 356-369.

(169) Sekar, S.; Aqueel Ahmed, A. T.; Pawar, S. M.; Lee, Y.; Im, H.; Kim, D. Y.; Lee, S. Enhanced water splitting performance of biomass activated carbon-anchored WO_3 nanoflakes. *Appl. Surf. Sci.* **2020**, *508*, 145127.

(170) Bharagav, U.; Ramesh Reddy, N.; Nava Koteswara Rao, V.; Ravi, P.; Sathish, M.; Rangappa, D.; Prathap, K.; Shilpa Chakra, C.; Shankar, M. V.; Appels, L.; et al. Bifunctional g-C(3)N(4)/carbon nanotubes/WO_3 ternary nanohybrids for photocatalytic energy and environmental applications. *Chemosphere* **2022**, *311*, 137030.

(171) Bittencourt, C.; Felten, A.; Espinosa, E. H.; Ionescu, R.; Moreau, N.; Heszler, P.; Granqvist, C. G.; Pireaux, J. J.; Llobet, E. Evaporation of WO_3on carbon nanotube films: a new hybrid film. *SMS.* **2006**, *15*, 1555-1560.

(172) Mpanza, T.; Ogundipe, S. A.; Ndlangamandla, C. L.; Swart, H. C.; Nkosi, S. S. The effect of acids precipitants on the synthesis of WO_3 hierarchical nanostructures for highly selective and sensitive H_2S detection. *FS..* **2023**, *4*, 1143080.

(173) Dang, W.; Wang, W.; Yang, Y.; Wang, Y.; Huang, J.; Fang, X.; Wu, L.; Rong, Z.; Chen, X.; Li, X.; et al. One-step hydrothermal synthesis of 2D WO_3 nanoplates@ graphene nanocomposite with superior anode performance for lithium ion battery. *Electrochim Acta* **2019**, *313*, 99-108.

(174) Yoon, S.; Jo, C.; Noh, S. Y.; Lee, C. W.; Song, J. H.; Lee, J. Development of a high-performance anode for lithium ion batteries using novel ordered mesoporous

tungsten oxide materials with high electrical conductivity. *Phys Chem Chem Phys.* **2011**, *13* , 11060-11066.

(175) Kim, D.-M.; Kim, S.-J.; Lee, Y.-W.; Kwak, D.-H.; Park, H.-C.; Kim, M.-C.; Hwang, B.-M.; Lee, S.; Choi, J.-H.; Hong, S.; et al. Two-dimensional nanocomposites based on tungsten oxide nanoplates and graphene nanosheets for high-performance lithium ion batteries. *Electrochim Acta* **2015**, *163*, 132-139.

(176) Shi, J.; Tian, X.; Wang, H.; Ge, L.; Li, J.; Lv, B. Oxygen deficient sea urchin-like Cu-WO3 with high capacity and long life for anode of lithium-ion battery.*Appl. Surf. Sci* .**2023**, *618*, 156627.

(177) Pan, Y.; Xu, M.; Yang, L.; Yu, M.; Liu, H.; Zeng, F. Porous architectures assembled with ultrathin Cu_2O–Mn_3O_4 hetero-nanosheets vertically anchoring on graphene for high-rate lithium-ion batteries. *J. Alloys Compd.* **2020**, *819*, 152969.

(178) Qiu, Y.; Xu, G.-L.; Kuang, Q.; Sun, S.-G.; Yang, S. Hierarchical WO3 flowers comprising porous single-crystalline nanoplates show enhanced lithium storage and photocatalysis. *Nano Res.* **2012**, *5* , 826-832.

(179) Sun, Y.; Wang, W.; Qin, J.; Zhao, D.; Mao, B.; Xiao, Y.; Cao, M. Oxygen vacancy-rich mesoporous $W_{18}O_{49}$ nanobelts with ultrahigh initial Coulombic efficiency toward high-performance lithium storage. *Electrochim Acta.* **2016**, *187*, 329-339.

(180) Rastgoo-Deylami, M.; Javanbakht, M.; Omidvar, H.; Hooshyari, K.; Salarizadeh, P.; Askari, M. B. Nickel-doped monoclinic WO_3 as high performance anode material for rechargeable lithium ion battery. *JEAC.* **2021**, *894*, 115383.

(181) Al-Samet, M. A. M. M.; Burgaz, E. Improving the lithium-ion diffusion and electrical conductivity of $LiFePO_4$ cathode material by doping magnesium and multi-walled carbon nanotubes. *J. Alloys Compd.* **2023**, *947*, 169680.

(182) Heme, H. N.; Alif, M. S. N.; Rahat, S. M. S. M.; Shuchi, S. B. Recent progress in polyaniline composites for high capacity energy storage: A review. *J. Energy Storage.* **2021**, *42*, 103018.

(183) Wang, H.; Qian, X.; Wu, H.; Zhang, R.; Wu, R. MOF-derived rod-like composites consisting of iron sulfides embedded in nitrogen-rich carbon as high-performance lithium-ion battery anodes. *Appl. Surf. Sci.* **2019**, *481*, 33-39.

(184) Liu, Y.; Chen, Z.; Jia, H.; Xu, H.; Liu, M.; Wu, R. Iron-Doping-Induced Phase Transformation in Dual-Carbon-Confined Cobalt Diselenide Enabling Superior Lithium Storage. *ACS Nano.* **2019**, *13*, 6113-6124.

(185) Wei, Y.; Huang, L.; He, J.; Guo, Y.; Qin, R.; Li, H.; Zhai, T. Healable Structure Triggered by Thermal/Electrochemical Force in Layered GeSe$_2$ for High Performance Li-Ion Batteries. *Advanced Energy Materials.* **2018**, *8*, 1703635.

List of Publications from thesis

1) Kiran, Laraib, Mehmet Kadri Aydınol, Syed Sakhawat Shah, Aneela Anwar, Syed Mustansar Abbas, Doruk Bahtiyar, Muhammad Siddiq, Abdul Rehman, Mohamed Ouladsmane, and Muhammad Imran Shahzad. "Mesoporous Cr_2O_3/MWCNTs/PANI nanocomposite as a high-performance anode material for rechargeable lithium-ion batteries." *Fuel* 352 (2023): 128961.

2) Kiran, Laraib, Mehmet Kadri Aydınol, Awais Ahmad, Syed Sakhawat Shah, Doruk Bahtiyar, Muhammad Imran Shahzad, Sayed M. Eldin, and Aboud Ahmed Awadh Bahajjaj. "Flowers Like α-MoO3/CNTs/PANI Nanocomposites as Anode Materials for High-Performance Lithium Storage." *Molecules* 28, no. 8 (2023): 3319